Constraints on Anomalous Quartic Gauge Boson Couplings at OPAL and the System Test of the ATLAS barrel SCT

Paul James Bell

Thesis submitted for the degree of
Doctor of Philosophy

Particle Physics Group
School of Physics and Astronomy
University of Birmingham

October 2003

Synopsis

Reported in this thesis is an analysis of OPAL data collected during the last four years of LEP operation at CERN, a review of the principal results of the ATLAS SCT barrel system test and a preliminary ATLAS Monte Carlo study.

Anomalous quartic couplings between the electroweak gauge bosons may contribute to the $e^+e^- \to \nu\overline{\nu}\gamma\gamma$ process. The main analysis uses 652 pb^{-1} of OPAL data recorded at 183-209 GeV centre-of-mass energies. A sample of 20 acoplanar photon pair events is selected and a binned maximum likelihood method used to constrain the possible WW$\gamma\gamma$ and ZZ$\gamma\gamma$ couplings. The 95% confidence level limits on the anomalous coupling parameters a_0^W, a_c^W, a_0^Z and a_c^Z are found to be

$$\begin{aligned}
-0.040\ \text{GeV}^{-2} < \quad a_0^W/\Lambda^2 \quad &< 0.037\ \text{GeV}^{-2}, \\
-0.114\ \text{GeV}^{-2} < \quad a_c^W/\Lambda^2 \quad &< 0.103\ \text{GeV}^{-2}, \\
-0.009\ \text{GeV}^{-2} < \quad a_0^Z/\Lambda^2 \quad &< 0.026\ \text{GeV}^{-2}, \\
-0.034\ \text{GeV}^{-2} < \quad a_c^Z/\Lambda^2 \quad &< 0.039\ \text{GeV}^{-2},
\end{aligned}$$

where Λ is the energy scale of the new physics. Limits obtained when allowing two or four parameters to vary are also presented. The results are combined with those from the $W^+W^-\gamma$ and $q\overline{q}\gamma\gamma$ processes also studied at OPAL.

Additionally, results are reported of the system test of 12 silicon micro-strip detector modules, operated on a prototype partial section of the inner-most ATLAS SCT barrel. The performance of the modules was found to be within the specified limits of the design. Methods have also been developed to measure the common-mode noise present in binary read-out systems, and their functionality is demonstrated by application to the ATLAS detector modules operated at the system test.

Finally, a Monte Carlo study of the W$\gamma\gamma$ final state produced in pp collisions is presented, using ATLFAST to model the events in the ATLAS detector. This tri-boson process may be sensitive to a possible anomalous WW$\gamma\gamma$ vertex.

Author's Contribution

Whilst all the words of this thesis are my own, the analysis reported herein is a result of the direct and indirect input of many collaborators; not least, those who operated the LEP accelerator and the OPAL detector before my Ph.D had even begun. I therefore make explicit here that work for which I have been responsible.

The OPAL analysis described in the first four chapters is based on an acoplanar event selection routine which I updated and optimised for the anomalous quartic gauge coupling scenario I was considering. I then wrote the necessary code to perform the binned maximum likelihood analysis of the data. I also undertook the evaluation of the systematic error sources, except where otherwise referenced. My results from the $\nu\overline{\nu}\gamma\gamma$ channel were published as an OPAL physics note [1] for the ICHEP conference in 2002. The method was subsequently re-optimised and the new results have been combined with those from the $W^+W^-\gamma$ and $q\overline{q}\gamma\gamma$ channels studied by Mark Thomson. At the time of writing, our paper reporting these combined results is undergoing the peer review procedure.

During my attachment to CERN, I worked as part of the ATLAS SCT barrel system test team. I was involved in the daily operation of the system test and contributed to many of what became the standard data taking and analysis tools in use there. I therefore give a summary of the principal results in chapter 5 of this thesis. In conjunction with Joern Grosse-Knetter I developed two methods of measuring common-mode noise in binary read-out systems and this work, forming the latter part of chapter 5, is currently in the publication process with Nuclear Instruments and Methods (A).

In the last few months of my Ph.D, I have been using the ATLFAST detector simulation program within the ATHENA framework to conduct a study of the $W\gamma\gamma$ process at ATLAS. This open ended work comprises the final chapter of this thesis.

Acknowledgements

I am indebted to Dave Charlton for his imparting of knowledge coupled with the first class supervision he has supplied throughout the last three years. I hope I shall continue to apply his thoroughness and attention to detail to all areas of my subsequent career. Further thanks are of course due to all members of the Birmingham University Particle Physics Group who made it a truly friendly, supportive and memorable place in which to have worked.

The OPAL analysis has benefited from the support of the wider OPAL community and in particular the assistance of Peter Krieger on all matters pertaining to the event selection is very gratefully acknowledged. I also thank Jo Pater for her supervision during the period I was based at CERN and the friendly, daily assistance of Joern Grosse-Knetter in getting to grips with the operation of the system test.

Finally, thanks are due to my friends in Birmingham and elsewhere who have made all the difference to my time as a student and, not least, those people closest to me, for their invaluable love and support.

Paul, October 2003

Contents

List of Figures

List of Tables

Chapter 1

Introduction and Theoretical Framework

The ancient Greeks' belief that the complexity of the everyday world was built from just four elements, earth, fire, air and water, was perhaps mankind's first attempt to understand the very nature of matter itself. Nearly three millennia later, modern day high energy physics research represents the continued pursuit of this same understanding. Within this field, the developments in theory and experiment of the last few decades have culminated in what is currently the most successful mathematical description of nature at its most fundamental level: the Standard Model of particle physics.

An overview of the Standard Model, in which all known elementary constituents of the sub-atomic world and the interactions between them are embedded, is presented in this chapter. The concept of self-couplings between the electroweak gauge bosons is introduced, indicating how their study represents an important test of the Standard Model. Finally, the formalism for possible anomalous quartic gauge couplings is presented and it is shown how these may be probed using the $e^+e^- \to \nu\overline{\nu}\gamma\gamma$ process.

1.1 Overview of the Standard Model

1.1.1 Introducing the Particles and Forces

The point-like elementary particles from which all matter in the Universe is thought to be composed are listed in table 1.1. The matter constituents themselves are the spin-$\frac{1}{2}$ *fermions*, named after the Fermi-Dirac statistics which they obey. These can interact with each other through some or all of the four *fundamental forces*; the strong, weak, electromagnetic and gravitational interactions, mediated by the exchange of further elementary particles, the *gauge bosons*.

GAUGE BOSONS	**FERMIONS**		
	Generation 1	**Generation 2**	**Generation 3**
	Leptons		
γ (0)	ν_e (<3 eV)	ν_μ (<0.19 MeV)	ν_τ (<18.2 MeV)
	e^- (511 keV)	μ^- (106 MeV)	τ^- (1.78 GeV)
$W^\pm$ (80.4 GeV)			
Z (91.2 GeV)	**Quarks**		
	u (1.5-4.5 MeV)	c (1.0-1.4 GeV)	t (∼180 GeV)
$g(\times 8)$ (0)	d (5.0-8.5 MeV)	s (80-155 MeV)	b (4.0-4.5 GeV)

Table 1.1: The elementary fermions and gauge bosons within the Standard Model. Their masses are given in parentheses [2].

The fermions exist as three generations of lepton and quark doublets. The first generation of leptons is formed by the electron (e^-) and its neutrino (ν_e), whilst the first generation of quarks consists of the up (u) and the down (d). The masses of these particles are indicated in table 1.1. The particles contained in the second and third generations are more massive duplicates of those in the first, but which are increasingly short-lived. These higher generation particles are therefore only produced in interactions of sufficient energy and are not seen in stable matter. Although the phenomenon of neutrino oscillations, first observed by the Super-Kamiokande

experiment in 1998 [3], demands that there be a mass difference between the different neutrino types, the small absolute values for the neutrino masses are neglected throughout this work.

The e^-, μ^- and τ^- leptons all possess an electric charge of $Q = -1$ (in units of the electron charge, e) while the quarks u, c, t and d, s, b have fractional electric charges $+\frac{2}{3}$ or $-\frac{1}{3}$, respectively. The quarks in addition carry a quantum number "colour", usually labelled as *red*, *green* or *blue*. For every fermion there is a corresponding anti-fermion, identical except for its internal quantum numbers such as electric charge and colour, which are reversed.

All fermions except the electrically neutral neutrinos can interact via the familiar electromagnetic force. This is mediated by virtual photon (γ) exchange and is well described by Quantum Electrodynamics (QED). With the exchange particle here being massless, the force is granted an infinite range by the Heisenberg Uncertainty Principle [4]. In contrast, the weak force, felt by all fermions, is carried by the massive charged $W^{\pm}$ bosons and the neutral Z boson and acts over a limited range. The formalism of the gauge group theory [5] describing QED and its unification with the weak interaction is outlined in the following sections of this chapter.

A detailed understanding of the quark model and the theory of Quantum Chromo Dynamics (QCD) describing the strong force, through which only these fermions can interact, is not required for the work presented in this thesis. The strong force is mediated between quarks by the exchange of eight coloured bosons called gluons (g). Although massless, strong self-interactions of these gluons limit the range of the interaction. The strong force binds the quarks together as colour neutral combinations, either in triplets as baryons, such as the proton (uud) and neutron (dud), or in quark-anti-quark pairs as mesons. Due to the phenomenon of confinement free quarks are never observed.

Although the dominating force on a cosmological scale, the gravitational interaction, transmitted between all particles with mass by the hypothetical massless graviton, is negligibly weak on the scale of sub-atomic particles and is not usually considered in particle physics.

1.1.2 Introducing Gauge Field Theory: Quantum Electrodynamics (QED)

The theory of QED describes how charged spin-$\frac{1}{2}$ particles obeying the Dirac equation interact electromagnetically via the exchange of virtual photons. The formalism precipitates from, for example, the Lagrangian for a free electron of mass m,

$$\mathcal{L} = i\bar{\psi}\gamma_\mu\partial^\mu\psi - m\bar{\psi}\psi,$$

by imposing local phase invariance [6]. That is, $\mathcal{L}$ should be invariant under transformations of the form

$$\psi(x) \to e^{-ie\hat{Q}\alpha(x)}\psi(x),$$

where $\hat{Q}$ is the charge operator, having eigenvalue $Q = -1$ for an electron, and $\alpha(x)$ is some scalar function of space and time. The condition is satisfied only if an extra term is added:

$$\mathcal{L} = i\bar{\psi}\gamma_\mu\partial^\mu\psi - m\bar{\psi}\psi - e\bar{\psi}\gamma_\mu Q\psi A^\mu,$$

where the vector field A^μ that is introduced transforms as

$$A^\mu \to A^\mu - \frac{1}{eQ}\partial^\mu\alpha(x).$$

Since the operator $\hat{Q}$ is the generator of the unitary Abelian group of transformations $\hat{U}(\alpha(x)) = e^{-ie\hat{Q}\alpha(x)}$, the Lagrangian is now said to possess local $U(1)_{\text{em}}$ gauge invariance. The so called gauge field, A^μ, can be identified with the Maxwell field vector, prompting the inclusion of a kinetic term, $-\frac{1}{4}F^{\mu\nu}F_{\mu\nu}$, where

$$F^{\mu\nu} = \partial^\mu A^\nu - \partial^\nu A^\mu.$$

The QED Lagrangian for an electron is therefore

$$\mathcal{L} = i\bar{\psi}(\gamma_\mu\partial^\mu - m)\psi - \frac{1}{4}F^{\mu\nu}F_{\mu\nu} - e\bar{\psi}\gamma_\mu Q\psi A^\mu,$$

which describes the Dirac field of the electron (1st term), the gauge field of the photon (2nd term) and the coupling of these two fields (3rd term). Adding a mass

term for A^μ is prohibited by the gauge invariance, supporting the association of the gauge field with the massless photon.

In order for the gauge field theory to be useful, it must make predictions for the cross-sections of processes involving interacting fermion and photon fields. This is achieved by drawing the *Feynman diagram* corresponding to the physical process of interest. From such a diagram, the matrix element, $-i\mathcal{M}$, of the transition amplitude for the process can be written down as the product of several factors, following the Feynman rules [7]. Drawn in figure 1.1 is the Feynman diagram for the scattering of an electron by a static charge, giving a simple illustration of the QED interaction at lowest order. The four-momentum, q, of the photon is given by four-momentum conservation at the vertex where the fermion and photon fields are coupled: the photon is virtual since $q^2 \neq 0$. Associated with the vertex is the Feynman vertex factor, $ie\gamma_\mu$, which, according with the Feynman rules, is the coefficient of the interaction term in $i\mathcal{L}$. This is one factor that enters the expression for $-i\mathcal{M}$. As a result, the amplitude for the process is governed by e.

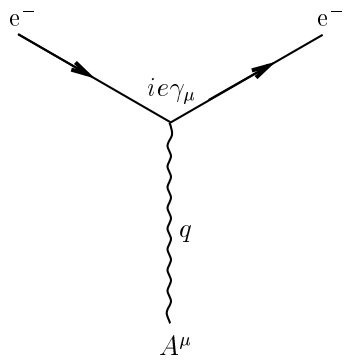

Figure 1.1: The lowest order (Born level) QED interaction. The Feynman diagram could correspond to the scattering of an electron from a static charge.

The Feynman diagram drawn in figure 1.1 depicts the so called Born level scattering process, involving the smallest number of couplings, e. Strictly, to calculate the full cross-section, the higher order processes shown in figure 1.2 need to be included, as these are identical in terms of the observable initial and final states. This is problematic since the unobserved particles in the loops have unconstrained

momenta which must be integrated over, yielding infinities in the calculations. The occurrence of such infinities is averted by the act of *renormalisation*, however, which essentially consists of absorbing them into the definition of the electron charge. The electron-photon coupling of diagram 1.1, which really corresponded to the bare charge, e_0, is redefined to include the effects of the higher order processes and set to its observed value, that is $\frac{e^2}{4\pi} = \frac{1}{137} = \alpha$. Thus, after renormalising, the process 1.1 is taken to represent its sum with all other possible higher order processes. The bare charge is now infinite and can be interpreted as a bare electron being surrounded by a cloud of virtual particles. When viewed from a distance the electron charge is measured as e, but when higher energy photons are used to probe closer to the bare electron its charge increases: this is described as the "running" of the electromagnetic coupling constant, α, with energy. That gauge field theories have proven to be the most successful way to describe and explain interactions on a sub-atomic scale is because they possess this property of being renormalisable [8].

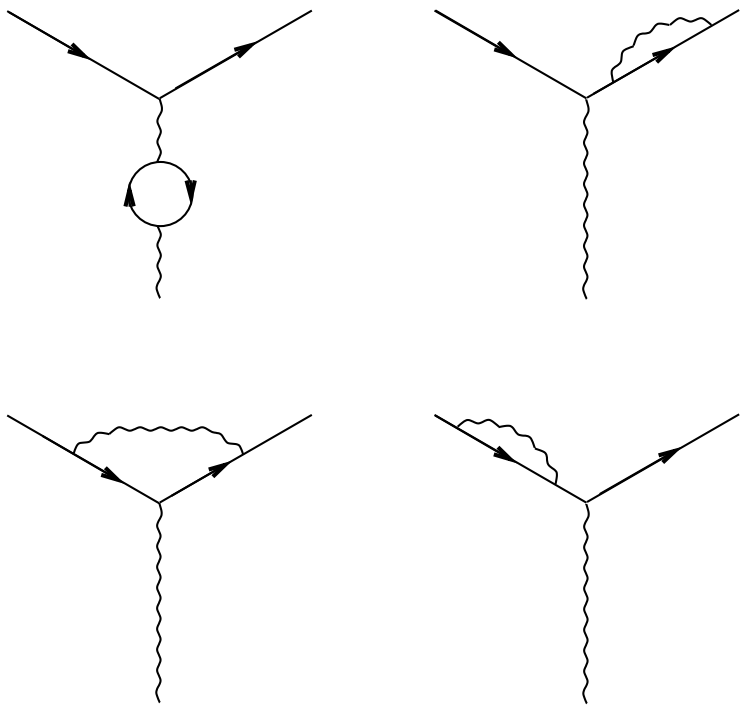

Figure 1.2: Higher order QED interactions.

By the theorem of Noether [9] the $U(1)_{\rm em}$ gauge invariance of the QED Lagrangian must be associated with some conserved quantity. In this case it is the current density $J^{\rm em}_\mu = \bar{\psi}\gamma_\mu Q\psi$, the conservation of which implies the conservation of charge at the QED vertex. The electromagnetic interaction of QED, $i\mathcal{L}_{\rm int}$, can be embodied in

$$-ieJ^{\rm em}_\mu A^\mu, \tag{1.1}$$

which is interpreted as the coupling of the gauge field to the fermion current with strength e.

1.1.3 The Weak Interactions

The weak force manifests itself in two forms: charged current interactions through the exchange of the $\rm W^+$ and $\rm W^-$ bosons and neutral current interactions via Z exchange [10]. For the first generation of leptons, the two vertices involving the exchange of W bosons are drawn in figure 1.3. In analogy to the photon field

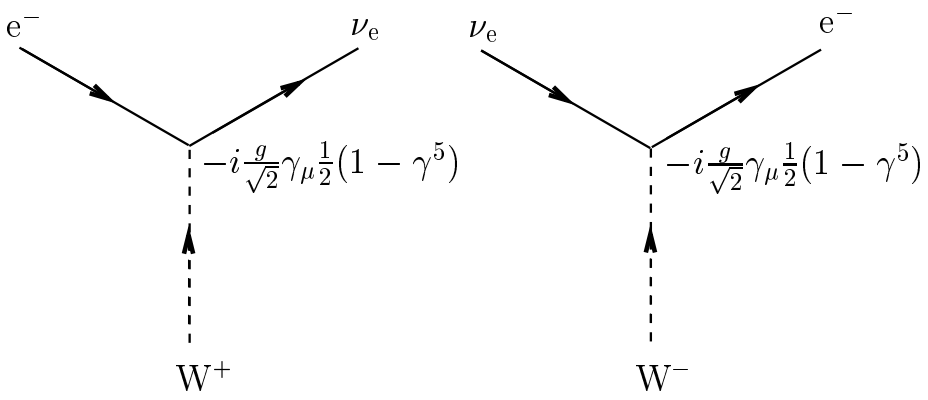

Figure 1.3: The charged current weak vertices. The vertex factors are the coefficients of $i\mathcal{L}^{\pm}_{\rm int}$.

coupling to the electromagnetic current $J^{\rm em}_\mu$ with strength e in QED, these weak interactions can be expressed as the field of the appropriate W boson, $W^{\mu+}$ or $W^{\mu-}$, coupling to either a charge raising or charge lowering current, J^+_μ or J^-_μ, with

strength $g/\sqrt{2}$:

$$i\mathcal{L}^{+}_{\rm int} = -i\frac{g}{\sqrt{2}}J^{+}_{\mu}W^{\mu+},$$
$$i\mathcal{L}^{-}_{\rm int} = -i\frac{g}{\sqrt{2}}J^{-}_{\mu}W^{\mu-}.$$

The observation of maximal parity violation, through the absence of left-handed anti-neutrinos and right-handed neutrinos in β decay experiments, revealed that the weak charged currents are necessarily of the vector minus axial-vector form. That is,

$$J^{+}_{\mu} = \bar{\nu}\gamma_{\mu}\frac{1}{2}(1-\gamma_5)e = \bar{\nu}_L\gamma_{\mu}e_L,$$
$$J^{-}_{\mu} = \bar{e}\gamma_{\mu}\frac{1}{2}(1-\gamma_5)\nu = \bar{e}_L\gamma_{\mu}\nu_L,$$

where the lepton names now denote the Dirac fields and the L subscripts record the left handed nature of the particles involved: at high energies, $\frac{1}{2}(1\pm\gamma_5)$ project out the positive and negative helicity eigenstates, or the right and left handed components of ψ. In the limit of massless particles, therefore, only left handed particles and right handed anti-particles participate in the charged current weak interactions.

Charged current weak interactions among the quarks are more complicated than within the leptonic sector due to the observed mixing between the quark doublets. The universality of the weak coupling g is preserved, but the charged currents couple to left handed quark states u, d$'$, c, s$'$, t and b$'$ which are orthogonal combinations of the physical (mass) eigenstates, u, d, c, s, t and b. This mixing is parametrised by the Cabibbo-Kobayashi-Maskawa matrix [11]:

$$\begin{pmatrix} d' \\ s' \\ b' \end{pmatrix} = V_{CKM} \begin{pmatrix} d \\ s \\ b \end{pmatrix}.$$

The mixing matrix V_{CKM} has small but non-zero off diagonal terms, allowing the possibility for decays to occur across the generations. For the leptons, taking the neutrino to be massless, analogous mixing is unobservable since any orthogonal combination of weak neutrino eigenstates gives a (zero) mass eigenstate. In weak

interactions therefore, ν_e is taken by definition to be the partner of the electron, and similarly for the muon and tau generations.

A possible Z-fermion vertex is shown in figure 1.4. Here there is no charge raising or lowering effect and the flavour of the scattered fermion remains unchanged. The interaction is characterised by a weak neutral current, J_μ^{NC}, coupling to the field of the Z boson, Z^μ. Unlike $J_\mu^\pm$ the form of J_μ^{NC} generally has some right-handed component, with the values of the factors c_A^f and c_V^f depending on the fermion type, f.

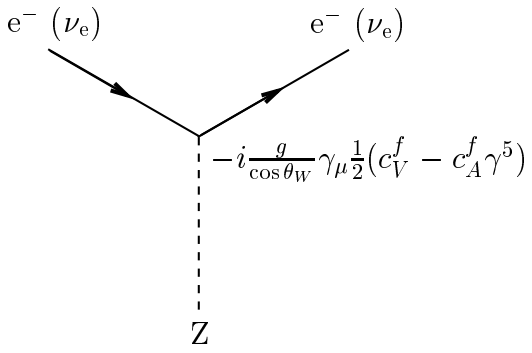

Figure 1.4: The neutral current weak vertex.

1.1.4 Electroweak Unification

The QED formalism followed from the requirement of local gauge invariance under $U(1)_{\mathrm{em}}$ transformations. Similar gauge symmetry principles allow the weak and electromagnetic interactions to be cast together as a unified electroweak theory, respecting the transformations of an encompassing gauge group [12]. The weak charged currents from the previous section can be written in 2-dimensional form as

$$J_\mu^+ = \bar{\chi_L}\gamma_\mu\tau_+\chi_L,$$
$$J_\mu^- = \bar{\chi_L}\gamma_\mu\tau_-\chi_L,$$

where

$$\tau_+ = \begin{pmatrix} 0 & 1 \\ 0 & 0 \end{pmatrix}, \quad \tau_- = \begin{pmatrix} 0 & 0 \\ 1 & 0 \end{pmatrix}.$$

and

$$\chi_L = \begin{pmatrix} \nu \\ e \end{pmatrix}_L.$$

The operators τ_+ and τ_- are related to the Pauli matrices τ_1 and τ_2 by $\tau_\pm = \frac{1}{2}(\tau_1 \pm i\tau_2)$. The three matrices $T_i = \frac{\tau_i}{2}$ are the three generators of $SU(2)_L$, the so called isospin symmetry group, where again the L subscript records the left-handed nature of the fermions involved. In this $SU(2)_L$ symmetry, the left handed electron and its neutrino form a doublet χ_L of weak isospin $T = \frac{1}{2}$ with third components $T_3 = +\frac{1}{2}$ (ν_L) and $T_3 = -\frac{1}{2}$ (e_L). The W^+ and W^- correspond to the ladder operators τ_+ and τ_- which shift between these weak isospin states by raising or lowering T_3. In the absence of a right handed neutrino, the right handed electron e_R forms an isosinglet state $\psi_R = \mathrm{e}_R$ of $T = 0$. When considering quarks the situation is analogous, with

$$\chi_L = \begin{pmatrix} \mathrm{u} \\ \mathrm{d}' \end{pmatrix}_L,$$

and $\psi_R = \mathrm{u}_R$ or d_R.

The charged currents use just two generators of the $SU(2)_L$ group, suggesting the existence of a third current of the form

$$J^3_\mu = \bar{\chi_L}\gamma_\mu \frac{1}{2}\tau_3 \chi_L$$

corresponding to T_3, completing an isospin triplet of currents J^i_μ. This can be identified with neither J^{em}_μ nor J^{NC}_μ of the previous sections, however, which both have right handed components. In order to accommodate QED and weak neutral currents, the $SU(2)_L$ group is enlarged to $SU(2)_L \times U(1)_Y$ with the inclusion of an additional $U(1)_Y$ symmetry, as proposed by Glashow [13]. This is generated by the

weak hypercharge operator Y, given by

$$Q = T_3 + \frac{Y}{2}$$

and has a corresponding conserved weak hypercharge current

$$J^Y_\mu = \bar{\psi}\gamma_\mu Y \psi.$$

Due to the relation between the generators above, $U(1)_{\rm em}$ exists as a subgroup of $SU(2)_L \times U(1)_Y$: it is in this way that the weak and electromagnetic interactions are said to be unified.

Having identified the appropriate gauge group, $SU(2)_L \times U(1)_Y$, the electroweak Lagrangian must be constructed such that it is invariant under local transformations of this type. The transformations are

$$\begin{aligned} \chi_L \to \chi'_L &= e^{i\alpha(\mathbf{x})\cdot\mathbf{T} + i\beta(x)Y}\chi_L, \\ \psi_R \to \psi'_R &= e^{i\beta(x)Y}\psi_R, \end{aligned} \tag{1.2}$$

illustrating explicitly how the chiral $SU(2)_L$ part acts only on the left handed fermion fields. For the overall Lagrangian to transform as a singlet, gauge fields (like the A^μ of QED) must be introduced: a triplet of vector fields $\mathbf{W}^\mu$ for the three generators of $SU(2)_L$ and a further vector field B^μ for the $U(1)_Y$ group. The resulting interaction terms then couple $\mathbf{W}^\mu$ to the triplet of currents $\mathbf{J}_\mu$ with strength g, and B^μ to the hypercharge current J^Y_μ with strength $g'/2$. The weak isospin and hypercharge interactions are therefore expressed as

$$-ig\mathbf{J}_\mu \cdot \mathbf{W}^\mu - i\frac{g'}{2}J^Y_\mu B^\mu. \tag{1.3}$$

The $\mathrm{W}^\pm$ bosons are described by the fields

$$W^{\mu\pm} = \sqrt{\frac{1}{2}}\left(W^{\mu 1} \mp iW^{\mu 2}\right)$$

and to uncover the physical Z and photon fields the neutral $W^{\mu 3}$ and B^μ fields have to mix as

$$\begin{aligned} A^\mu &= B^\mu \cos\theta_W + W^{\mu 3}\sin\theta_W, \\ Z^\mu &= -B^\mu \sin\theta_W + W^{\mu 3}\cos\theta_W, \end{aligned} \tag{1.4}$$

where θ_W is the weak mixing angle. Comparing equation (1.4) with the interactions of (1.3) and requiring that the electromagnetic interaction of (1.1) can be extracted reveals that $J_\mu^{\rm em}$ and $J_\mu^{\rm NC}$ are given by the orthogonal combinations

$$J_\mu^{\rm em} = J_\mu^3 + \frac{1}{2}J_\mu^Y,$$
$$J_\mu^{\rm NC} = J_\mu^3 - \sin^2\theta_W J_\mu^{\rm em},$$

with the relation

$$e = g\sin\theta_W = g'\cos\theta_W. \tag{1.5}$$

Writing the couplings between the fields and the currents (1.3) in terms of the fields and the generators of the $SU(2)_L \times U(1)_Y$ symmetry, the full electroweak Lagrangian for an electron-neutrino lepton pair is

$$\begin{aligned}\mathcal{L}_{\rm EW}^{\rm e,\nu_e} = \; & \bar{\chi_L}\gamma^\mu[i\partial_\mu - g\frac{1}{2}\boldsymbol{\tau}\cdot\mathbf{W}_\mu - g'\frac{Y}{2}B_\mu]\chi_L \\ & + \bar{e_R}\gamma^\mu[i\partial_\mu - g'\frac{Y}{2}B_\mu]e_R \\ & - \frac{1}{4}\mathbf{W}_{\mu\nu}\cdot\mathbf{W}^{\mu\nu} - \frac{1}{4}B_{\mu\nu}B^{\mu\nu}. \end{aligned} \tag{1.6}$$

The first two terms embody the kinetic energies of the electron and the neutrino and their interactions with the $\mathbf{W}^\nu$ and B^μ fields. The last two are the kinetic energy and self-coupling of the $\mathbf{W}^\mu$ fields,

$$\mathbf{W}^{\mu\nu} = \partial^\mu\mathbf{W}^\nu - \partial^\nu\mathbf{W}^\mu - g\mathbf{W}^\mu\times\mathbf{W}^\nu,$$

and the kinetic energy of the B^μ field,

$$B^{\mu\nu} = \partial^\mu B^\nu - \partial^\nu B^\mu.$$

The last term in the expression for $\mathbf{W}^{\mu\nu}$ arises since the generators of the group, T_i, do not commute: the group is non-Abelian. This is the origin of the self-couplings of the gauge bosons and is revisited in section 1.2.

1.1.5 Electroweak Symmetry Breaking

The electroweak Lagrangian presented in equation (1.6) describes only massless fermions and gauge fields. Fermion mass terms, of the form

$$-m\overline{\psi}\psi = -m(\overline{\psi}_L\psi_R + \overline{\psi}_R\psi_L)$$

mix the right and left handed components and so cannot be invariant under the chiral transformations of (1.2). A method of acquiring the necessary mass terms without violating the gauge invariance and thereby losing the property of renormalisability is therefore required. Moreover, the necessary mixing of the fields shown in (1.4) must be achieved, with the Z along with the Ws gaining mass whilst leaving the photon field massless. In the Standard Model this is achieved via the Higgs mechanism [14], outlined below.

An $SU(2)_L \times U(1)_Y$ gauge invariant term, $\mathcal{L}_{\text{Higgs}} = T(\phi) - V(\phi)$, is added to $\mathcal{L}_{\text{EW}}$. In the Weinberg-Salam "minimal" model of electroweak interactions, ϕ is an $SU(2)_L$ doublet of complex scalar fields with weak hypercharge $Y = 1$:

$$\phi = \sqrt{\frac{1}{2}} \begin{pmatrix} \phi_1 + i\phi_2 \\ \phi_3 + i\phi_4 \end{pmatrix}.$$

The potential term, given by

$$V(\phi^\dagger\phi) = \mu^2\phi^\dagger\phi + \lambda(\phi^\dagger\phi)^2,$$

with $\mu^2 < 0$ and $\lambda > 0$, makes the vacuum infinitely degenerate, and the $SU(2)_L \times U(1)_Y$ symmetry is said to be *spontaneously broken* upon making a choice of ground state about which to perform perturbative calculations. That is, once such a transformation has been made, the symmetry of the Lagrangian is no longer apparent: the vacuum of the theory no longer possesses the same $SU(2)_L \times U(1)_Y$ symmetry as the Lagrangian. The ground states are obtained by minimising the potential, V, and occur for $|\phi|^2 = -\frac{\mu^2}{2\lambda}$. Expanding about any one of these infinite number of minima generates the required mass-like terms for the gauge fields.

The particular minimum

$$\phi_1 = \phi_2 = \phi_4 = 0, \qquad \phi_3^2 = -\frac{\mu^2}{\lambda} = v^2$$

can be chosen to demonstrate that the vacuum expectation value of ϕ is

$$\phi_0 = \sqrt{\frac{1}{2}} \begin{pmatrix} 0 \\ v \end{pmatrix}.$$

Since $Q = T_3 + \frac{Y}{2}$, the vacuum is neutral ($\hat{Q}\phi_0 = 0$) and therefore invariant under the $U(1)_{\rm em}$ transformations for which Q is the generator. Thus, the symmetry group is broken as

$$SU(2)_L \times U(1)_Y \to U(1)_{\rm em}$$

which results in mass-like terms appearing for just three of the gauge bosons and the photon, associated with the $U(1)_{\rm em}$ subgroup, remaining massless. Three of the scalar degrees of freedom, the "would-be" Goldstone bosons associated with the three broken symmetries, are absorbed as the required longitudinal polarisations of the now massive $\rm W^{\pm}$ and Z. One massive scalar field remains: that of the Higgs boson.

After the symmetry is spontaneously broken, the Ws gain a mass equal to $\frac{1}{2}vg$. The mixing of the $\mathbf{W}^{\mu 3}$ and B^{μ} fields yields one combination A^{μ} which gains no mass, whilst the orthogonal combination Z^{μ} has a mass $\frac{1}{2}v\sqrt{(g^2 + g'^2)}$. From $e = g \sin\theta_W = g' \cos\theta_W$ the relation

$$\rho = \frac{M_{\rm W}}{M_{\rm Z} \cos\theta_W} = 1$$

at leading order (tree level) is predicted. The $\rm W^{\pm}$ and Z bosons were discovered at CERN in 1983 [15] and their masses are in excellent agreement with the observed value of θ_W. The experimental observation that the value of the ρ parameter is very close to unity [2],

$$\rho = 1.0012^{+0.0023}_{-0.0014},$$

is associated with the so-called $SU(2)_C$ custodial symmetry [16, 17] ensuring the necessary W and Z mass relations.

The same Higgs doublet that gives mass to the $\rm W^{\pm}$ and Z bosons is also responsible for the generation of the fermion masses, and the eagerly awaited discovery of the Higgs boson may confirm this final and least well understood ingredient of the electroweak sector.

1.1.6 The Standard Model and Beyond

The formalism for the strong interaction is based on a gauge principle generated by transformations of the type $SU(3)_c$, where c labels colour as the conserved charge. The $SU(3)_c$ symmetry is unbroken, so the gauge fields of the eight gluons remain massless. The inclusion of this gauge group enlarges the group that encapsulates the Standard Model to $SU(3)_c \times SU(2)_L \times SU(1)_Y$ [18].

Despite thus far proving to be experimentally robust, it should be noted that the Standard Model is not a complete theory. The Higgs sector, assuming it is confirmed, does not *predict* the fermion masses: they remain some of the eighteen free parameters which have to be measured experimentally and inserted by hand. There is no explanation of why there are three and only three fermion generations. Little is said about gravity. Theorists are therefore motivated to consider possible extensions to the Standard Model, which can be mathematically aesthetically appealing. In Grand Unified Theories (GUTs) [19], for example, the strong, weak and electromagnetic interactions are embedded in a single gauge group. Alternatively, supersymmetry [20] predicts the existence of bosonic "superpartners" for all fermions and fermionic superpartners for all bosons. However, there has been no signs of the predictions of GUTs (such as proton decay) or supersymmetric models, whilst a further alternative, string theory, is currently unable to make any experimental predictions testable at the energies currently attainable. Moreover, aside from the need to incorporate neutrino masses and mixings, which demands a relatively minor modification to the electroweak sector, the Standard Model has withstood all the tests that the experimentalists can currently perform: there have so far been no observations that require any significant extensions to the Model.

1.2 Gauge Boson Self-Couplings

1.2.1 Gauge Boson Self-Couplings in the Standard Model

Section 1.1.4 illustrated how it is the imposition of the $SU(2)_L \times U(1)_Y$ local gauge symmetry that generates the gauge fields $\mathbf{W}^\mu$ and B^μ of the electroweak Lagrangian. As a result of the $\mathbf{T}$ matrices that generate the $SU(2)_L$ group not commuting with each other, $\mathbf{W}^{\mu\nu}$ is given by

$$\mathbf{W}^{\mu\nu} = \partial^\mu \mathbf{W}^\nu - \partial^\nu \mathbf{W}^\mu - g\mathbf{W}^\mu \times \mathbf{W}^\nu$$

and the $-\frac{1}{4}\mathbf{W}^{\mu\nu} \cdot \mathbf{W}_{\mu\nu}$ term therefore records the self-interactions of the gauge fields. This term leads to both triple gauge couplings (TGCs) of the form WWγ and WWZ and the quartic gauge couplings (QGCs) WWWW, WWZZ, WW$\gamma\gamma$ and WWZγ, as shown in figures 1.5. We refer to "gauge" couplings because of the way in which they arise from the imposition of the Yang-Mills (non-Abelian) gauge invariance: the vertex factors are determined by the $SU(2)_L \times U(1)_Y$ symmetry as functions of g, the same universal coupling with which the gauge bosons couple to the fermions. Studying the form and structure of the gauge boson self-couplings is therefore an important test of whether the fundamental interactions of nature are indeed described by a non-Abelian $SU(2)_L \times U(1)_Y$ gauge structure.

1.2.2 Anomalous Triple Gauge Couplings

Although measurements made at LEP have tested most of the fermion-gauge boson couplings precisely, there have so far been no precision tests of the gauge boson self-couplings. The study of these usually proceeds via an effective Lagrangian formalism. Such Lagrangians incorporate the new physics that may give rise to deviations in the TGCs or QGCs from their Standard Model expectations, whilst including the electroweak theory as a low energy limit. In the case of the triple gauge couplings, the most general Lorentz invariant effective Lagrangian for WWV

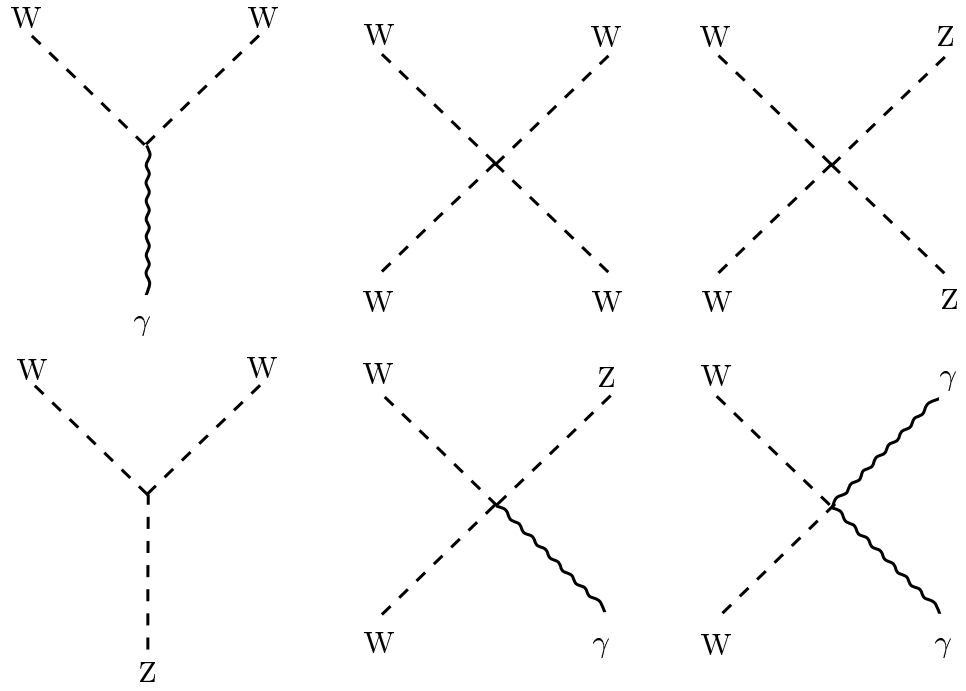

Figure 1.5: Three- and four-point gauge-boson self-couplings in the Standard Model. The coupling factors at the vertices are determined as functions of g by the gauge structure of the Standard Model.

where $\mathrm{V} = \gamma, \mathrm{Z}$ is

$$\begin{aligned}
i\frac{\mathcal{L}^{\mathrm{WWV}}_{eff}}{g_{\mathrm{WWV}}} = \; & g_1^{\mathrm{V}} V^\mu \left(W^-_{\mu\nu} W^{\nu+} - W^+_{\mu\nu} W^{\nu-}\right) \\
& + \kappa_{\mathrm{V}} W^+_\mu W^-_\nu V^{\mu\nu} \\
& + \frac{\lambda_{\mathrm{V}}}{M^2_{\mathrm{W}}} V^{\mu\nu} W^{\rho+}_\nu W^-_{\rho\mu} \\
& + i g_5^{\mathrm{V}} \epsilon_{\mu\nu\rho\sigma} \left((\partial_\rho W^{\mu-}) W^{\nu+} - W^{\mu-} (\partial^\rho W^{\nu+})\right) V^\sigma \\
& + i g_4^{\mathrm{V}} W^-_\mu W^+_\nu (\partial^\mu V^\nu + \partial^\nu V^\mu) \\
& - \frac{\tilde{\kappa}_{\mathrm{V}}}{2} W^-_\mu W^+_\nu \epsilon^{\mu\nu\rho\sigma} V_{\rho\sigma} \\
& - \frac{\tilde{\lambda}_{\mathrm{V}}}{2M^2_{\mathrm{W}}} W^-_{\rho\mu} W^{\mu+}_\nu \epsilon^{\nu\rho\alpha\beta} V_{\alpha\beta},
\end{aligned}$$

in which $V^{\mu\nu} = \partial^\mu V^\nu - \partial^\nu V^\mu$ and $W^{\mu\nu} = \partial^\mu W^\nu - \partial^\nu W^\mu$. There are seven coupling parameters for each vertex, g_1^{V}, κ_{V}, λ_{V}, g_5^{V}, g_4^{V}, $\tilde{\kappa}_{\mathrm{V}}$ and $\tilde{\lambda}_{\mathrm{V}}$, together with an overall coupling strength g_{WWV} where $g_{\mathrm{WW}\gamma} = -e$ and $g_{\mathrm{WWZ}} = -e\cot\theta_W$. However, by requiring electromagnetic gauge invariance (charge conservation), CP conservation

and $SU(2)_L \times U(1)_Y$ gauge invariance, the total number of independent couplings is reduced to four: g_1^Z, κ_γ, g_5^Z, and λ, where $\lambda = \lambda_\gamma = \lambda_Z$. The Standard Model predictions for these are $g_1^Z = 1$, $\kappa_\gamma = 1$, $g_1^Z = 0$ and $\lambda = 0$. Measurements of the $e^+e^- \to W^+W^-$ process [21] by OPAL have found their values to be

$$\begin{aligned} g_1^Z &= 0.987^{+0.034}_{-0.033}, \\ \kappa_\gamma &= 0.88^{+0.09}_{-0.08}, \\ g_5^Z &= -0.04^{+0.13}_{-0.12}, \\ \lambda &= -0.060^{+0.034}_{-0.033}. \end{aligned}$$

These are in good agreement with the Standard Model expectation and therefore constitute strong evidence for its gauge structure.

1.2.3 Anomalous Quartic Gauge Couplings

The study of quartic gauge boson self-couplings proceeds in a similar way to that of the tri-linear couplings, by writing down effective Lagrangian terms parametrising any possible anomalous contributions. Whereas probing the TGCs is regarded purely as a test of the non-Abelian structure of the Standard Model, however, the QGCs may provide a window on the mechanism responsible for the spontaneous breaking of the electroweak symmetry [22]. For example, to conserve unitarity in W^+W^- scattering events (figure 1.6), the Standard Model Higgs exchange diagram is required to conspire with the γ/Z exchange diagrams and the QGC process. Deviations in the expected scattering amplitudes of longitudinally polarised vector bosons, which originate from the three would-be Goldstone bosons, may therefore yield the first experimental signature of some symmetry breaking mechanism alternative to the Higgs.

No experiment has allowed the quartic vertices between four massive vector bosons to be studied, due to the lack of phase space for massive vector boson scattering and the inability to produce the alternative three massive vector boson final state. However, LEP-2 was able to produce final states with two massive vector

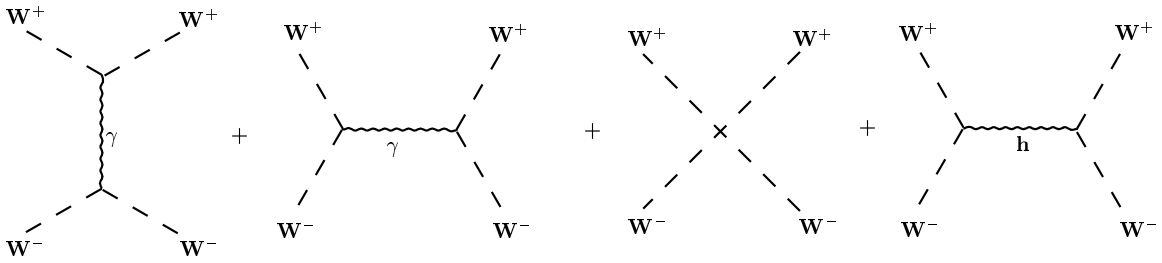

Figure 1.6: Contributions to the W^+W^-scattering process, $W^+W^- \to W^+W^-$. The addition of the QGC process to the first two diagrams is not sufficient to conserve unitarity: the Higgs particle (h) exchange diagram is also required.

bosons, permitting quartic vertices with at least one hard photon to be probed directly. Any deviations here are indicative of some discrepancy in the general sector of quartic couplings.

The formalism for extra possible quartic terms involving at least one photon has been discussed widely in the literature (see e.g. [22, 23, 24]). The term

$$\mathcal{L}_{\mathrm{WW}\gamma} = -ie\frac{\lambda_\gamma}{M_{\mathrm{W}}^2}F^{\mu\nu}W^\dagger_{\mu\alpha}W^\alpha_\nu$$

generates an anomalous $\mathrm{WW}\gamma\gamma$ coupling but since it is also associated with a $\mathrm{WW}\gamma$ vertex the parameter λ_γ is constrained by TGC analyses using the $e^+e^- \to W^+W^-$ process.

A purely quartic anomalous coupling of the form $\mathrm{WWZ}\gamma$, which violates C and CP, has been considered in [22] and [23] and is parametrised in [24] by the Lagrangian

$$\begin{aligned}\mathcal{L}_{\mathrm{n}} &= -i\frac{e^2}{16\cos\theta_W}\frac{a_{\mathrm{n}}}{\Lambda^2}\{F^\nu_\mu[Z^{\mu\alpha}(W^+_\alpha W^-_\nu - W^-_\alpha W^+_\nu)\\ &+ W^{+\mu\alpha}(W^-_\nu Z_\alpha - Z_\nu W^-_\alpha)\\ &- W^{-\mu\alpha}(W^+_\nu Z_\alpha - Z_\nu W^+_\alpha)]\}\end{aligned}$$

with anomalous coupling parameter a_{n}. Also reported in [24], the two lowest dimension terms that give rise to purely quartic couplings involving two photons are:

$$\begin{aligned}\mathcal{L}_0 &= -\frac{e^2}{8}\frac{a_0^{\mathrm{W}}}{\Lambda^2}F_{\mu\nu}F^{\mu\nu}W^{+\alpha}W^-_\alpha - \frac{e^2}{16\cos^2\theta_W}\frac{a_0^{\mathrm{Z}}}{\Lambda^2}F_{\mu\nu}F^{\mu\nu}Z^\alpha Z_\alpha,\\ \mathcal{L}_{\mathrm{c}} &= -\frac{e^2}{16}\frac{a_{\mathrm{c}}^{\mathrm{W}}}{\Lambda^2}F_{\mu\alpha}F^{\mu\beta}(W^{+\alpha}W^-_\beta + W^{-\alpha}W^+_\beta) - \frac{e^2}{16\cos^2\theta_W}\frac{a_{\mathrm{c}}^{\mathrm{Z}}}{\Lambda^2}F_{\mu\alpha}F^{\mu\beta}Z^\alpha Z_\beta.\end{aligned}$$

These are obtained by imposing local $U(1)_{\rm em}$ gauge symmetry and demanding both C and P conservation. They also respect the $SU(2)_C$ custodial symmetry. Both terms generate anomalous quartic gauge couplings (AQGCs) of the form WW$\gamma\gamma$ and ZZ$\gamma\gamma$, the latter of which does not occur in the Standard Model. In this formalism the couplings at the W and Z vertices are distinguished, unlike the earlier treatment in [22] in which $a_0^{\rm W} = a_0^{\rm Z} = a_0$ and $a_{\rm c}^{\rm W} = a_{\rm c}^{\rm Z} = a_{\rm c}$. These restrictions were formerly imposed on the grounds of assuring custodial symmetry, though the more recent work of [24] has shown that $a_0^{\rm W} = a_0^{\rm Z}$ and $a_{\rm c}^{\rm W} = a_{\rm c}^{\rm Z}$ are not essential for preserving $SU(2)_C$. In all cases the strengths of the quartic couplings are proportional to $\frac{1}{\Lambda^2}$ where Λ, the energy scale of the new physics, is by convention often set to $M_{\rm W}$.

Previous OPAL analyses have placed constraints on the possible anomalous couplings at the WWZγ, WW$\gamma\gamma$ and ZZ$\gamma\gamma$ quartic vertices. These were expressed as limits on the parameters $a_{\rm n}$, a_0 and $a_{\rm c}$ found from the $\rm W^+W^-\gamma$ final state [25, 26] and on a_0 and $a_{\rm c}$ from the $\nu\overline{\nu}\gamma\gamma$ [27] and $\rm q\bar{q}\gamma\gamma$ [28] final states. DELPHI has also constrained $a_{\rm n}$, a_0 and $a_{\rm c}$ from the $\rm W^+W^-\gamma$ process [29] and L3 from $\nu\overline{\nu}\gamma\gamma$, $\rm W^+W^-\gamma$ [30] and $\rm q\overline{q}\gamma\gamma$ [31]. The ALEPH experiment has reported constraints on the independent $a_0^{\rm Z}$, $a_{\rm c}^{\rm Z}$ and $a_0^{\rm W}$, $a_{\rm c}^{\rm W}$ parameters from the $\nu\overline{\nu}\gamma\gamma$ final state [32].

The work reported in the following three chapters of this thesis looks again at the $\nu\overline{\nu}\gamma\gamma$ final state at OPAL and seeks to constrain the anomalous coupling parameters $a_0^{\rm W}$, $a_{\rm c}^{\rm W}$, $a_0^{\rm Z}$ and $a_{\rm c}^{\rm Z}$ from the terms $\mathcal{L}_0$ and $\mathcal{L}_{\rm c}$ above. Compared to [27] a much larger data sample is used and unlike the previous OPAL study, which considered only a possible anomalous WW$\gamma\gamma$ vertex, the possible ZZ$\gamma\gamma$ contribution is now also taken into account.

The possibilities for measuring anomalous quartic gauge couplings at hadron colliders have also been investigated, see for example [33]. In the final chapter a preliminary study of the W$\gamma\gamma$ final state at ATLAS, sensitive to the WW$\gamma\gamma$ vertex, is presented.

1.2.4 AQGCs in the $e^+e^- \to \nu\overline{\nu}\gamma\gamma$ Process

The dominant Standard Model contribution leading to the $\nu\overline{\nu}\gamma\gamma$ final state at LEP is doubly-radiative return to the Z by the emission of two initial state photons (figure 1.7). There also exists a set of twelve so-called "WW fusion" diagrams which can be found explicitly in [34].

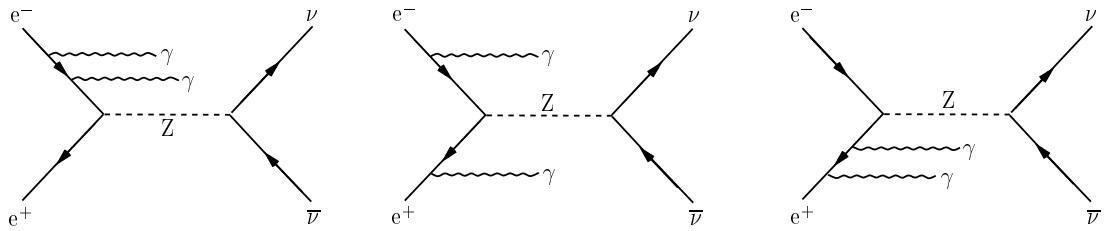

Figure 1.7: The Standard Model doubly-radiative return processes leading to $\nu\overline{\nu}\gamma\gamma$.

Figure 1.8 shows the contributions to $e^+e^- \to \nu\overline{\nu}\gamma\gamma$ arising from the AQGCs parametrised by $\mathcal{L}_0$ and $\mathcal{L}_c$. Since the Lagrangian terms are linear in the parameters a_0^W, a_0^Z and a_c^W, a_c^Z, so too are the vertex factors and consequently the matrix elements for the processes of figure 1.8. The WW$\gamma\gamma$ and ZZ$\gamma\gamma$ contributions to the amplitude for $e^+e^- \to \nu\overline{\nu}\gamma\gamma$ therefore vary linearly with the anomalous coupling parameters (a_0^W, a_c^W) and (a_0^Z, a_c^Z), respectively. Since the total amplitude is the sum of the contributions from the AQGC diagrams and the Standard Model processes, the total $\nu\overline{\nu}\gamma\gamma$ cross-section gains a quadratic dependence on each of the parameters. Due to the appearance of field strength tensor $F_{\mu\nu}$ in the Lagrangian terms, according to the Feynman rules the vertex couplings also vary linearly with the energy of the photons.

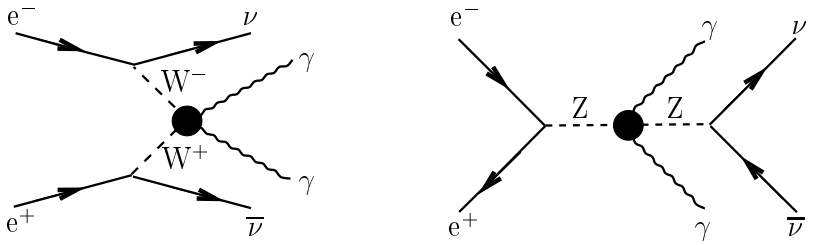

Figure 1.8: The anomalous WW$\gamma\gamma$ and ZZ$\gamma\gamma$ quartic gauge coupling contributions to $e^+e^- \to \nu\overline{\nu}\gamma\gamma$ arising from the Lagrangian terms $\mathcal{L}_0$ and $\mathcal{L}_c$. The coupling at the WW$\gamma\gamma$ vertex is given by (a_0^W, a_c^W) and at the ZZ$\gamma\gamma$ vertex by (a_0^Z, a_c^Z).

Chapter 2

Experimental Framework

The LEP accelerator and its four detectors typified the huge scale of apparatus, manpower and financial cost entailed in modern day high energy particle physics experiments. In this chapter, the operation of LEP and the OPAL detector are described, covering some of the physical principles involved and highlighting the components of the detector most relevant to this analysis. The role of Monte Carlo models in making experimentally observable predictions from theory is introduced. Finally, a description is given of the method of selection of the required $\nu\overline{\nu}\gamma\gamma$ events.

2.1 Particle Acceleration at LEP

The Large Electron-Positron Collider known as LEP [35, 36] was operated at CERN, on the Swiss-French border near Geneva, from 1989 to 2000. The synchrotron, housed in a 27 km circumference tunnel approximately 5 m in diameter and 100 m below the ground, accelerated two counter-rotating beams of electrons and positrons in a single beam pipe. A schematic diagram of LEP and its injector chain is given in figure 2.1. The electrons originated from thermionic emission from a heated cathode and were accelerated by the first LEP Injector LINAC (LIL) up to 200 MeV. Such a LINAC (LINear ACcelerator) is essentially a set of metal drift tubes alternatively attached to either side of an alternating radio frequency (RF) high voltage which

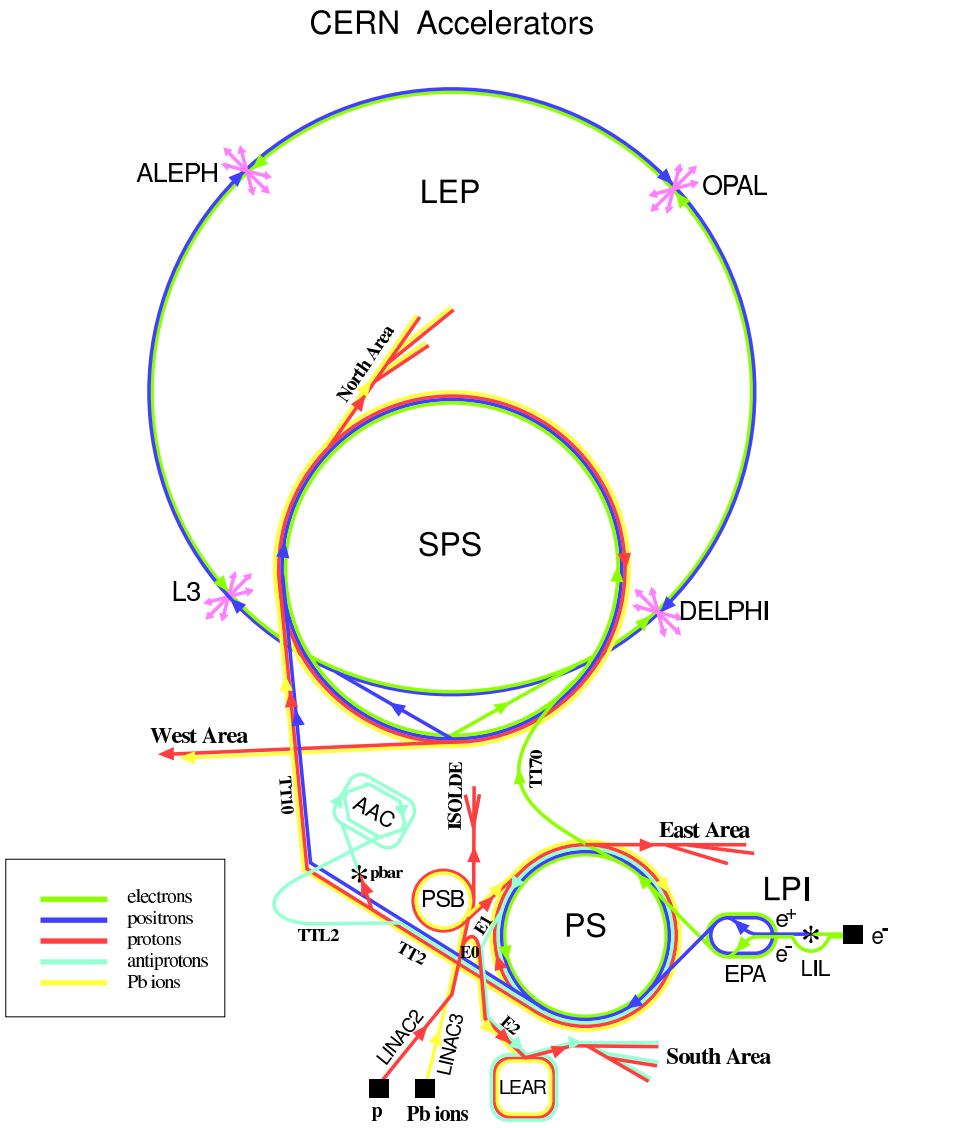

LEP: Large Electron Positron collider
SPS: Super Proton Synchrotron
AAC: Antiproton Accumulator Complex
ISOLDE: Isotope Separator OnLine DEvice
PSB: Proton Synchrotron Booster
PS: Proton Synchrotron
LPI: Lep Pre-Injector
EPA: Electron Positron Accumulator
LIL: Lep Injector Linac
LINAC: LINear ACcelerator
LEAR: Low Energy Antiproton Ring

Rudolf LEY, PS Division, CERN, 02.09.96

Figure 2.1: The LEP accelerator and injector system.

accelerates charged particles along an evacuated beam pipe. Accelerated electrons emerging from this LINAC were brought into collision with a tungsten target, producing photons via Bremsstrahlung and subsequently electron-positron pairs, which were separated by a magnetic field. These positrons and the electrons from the first LINAC were then further accelerated to 600 MeV by a second LINAC, before entering the Electron Positron Accumulator (EPA) storage ring. After sufficient accumulation in the EPA, the particle bunches passed to the Proton Synchrotron (PS) and finally to the Super Proton Synchrotron (SPS) to be accelerated up to 20 GeV, prior to injection into LEP. Once in LEP, the bunches, each containing approximately 10^{11} electrons or positrons, were stored and brought to their final collision energy. During its latest, highest centre-of-mass energy runs, this filling of LEP typically took one hour, for perhaps three hours of operation.

Within LEP, further acceleration was provided by RF cavities positioned along the straight sections. Electromagnetic dipoles were also required to produce the necessary magnetic fields to steer the particles around the curved sections. The name synchrotron refers to the need to increase these bending fields, and the RF frequencies, with the energy of the particles. The beam transport system that kept the beams in their orbits consisted of, in addition to more than 3 000 dipole bending magnets, over 800 quadrupole focusing magnets and around 1 200 further sextupole and correcting magnets. Quadrupole magnets focus the beam along one axis transverse to its motion, but at the same time defocus it along the other. A net focusing effect is achieved with a succession of such magnets arranged with their focusing directions alternately perpendicular to each other. The particle bunches were reduced in size such that at the crossing points of the electron and positron beams their cross-sections were just 10 μm by 250 μm in the vertical and horizontal directions, respectively. At four such points were located the detectors, OPAL [37], ALEPH [38], DELPHI [39] and L3 [40], which recorded the products of the resulting e^+e^- interactions.

Originally operated as a Z factory, LEP initially consisted of 128 copper RF cavities with a total accelerating voltage of 400 MV per lap. During the so called LEP-2 phase beginning in 1996, the attainable centre-of-mass energy was increased

by replacing these copper RF cavities with over 100 new super-conducting cavities. Before providing any additional acceleration of the beam particles, however, the RF cavities in a synchrotron must first compensate for the energy lost through synchrotron radiation. This radiation is emitted by any orbiting charged particle by virtue of its centripetal acceleration. For high energy electrons and positrons of energy E, the energy loss per particle per cycle, ΔE, increases as E^4/R, where R is the radius of the synchrotron [41]. The energy requirement to meet the synchrotron losses therefore rises rapidly with the centre-of-mass energy, which limits the highest energy attainable in a synchrotron of a certain radius.

In the final months of operation, some of the original copper cavities were reinstalled in LEP and a high of 209 GeV centre-of-mass energy was reached, before the machine and its detectors were decommissioned to make way for the construction of the Large Hadron Collider (LHC). When completed in 2007, the LHC will accelerate protons in two separate beam pipes, reaching a centre-of-mass energy of 14 TeV. For a relativistic proton, the synchrotron energy loss is 10^{13} times smaller than for an electron of the same momentum. This facilitates the much greater centre-of-mass energy of the new machine, using beam pipes located inside the existing LEP tunnel.

2.2 Particle Detection at OPAL

The task of OPAL (the Omni Purpose Apparatus for LEP) was to detect, identify and measure the energies and momenta of the particles produced in the e^+e^- collisions. A schematic diagram of the detector is shown in figure 2.2. The two paramount design features are: (1) as close as possible to 4π solid angle coverage allowing all collision products to be detected and thus any missing energy and momentum to be attributed to "invisibles", neutrinos in the Standard Model; (2) "onion-like" layered construction with different sub-detectors for detecting and identifying different types of particle and for measuring different particle properties.

The coordinate system used to map the events occurring within the detector is shown in the bottom corner of figure 2.2. The electron beam direction is taken as

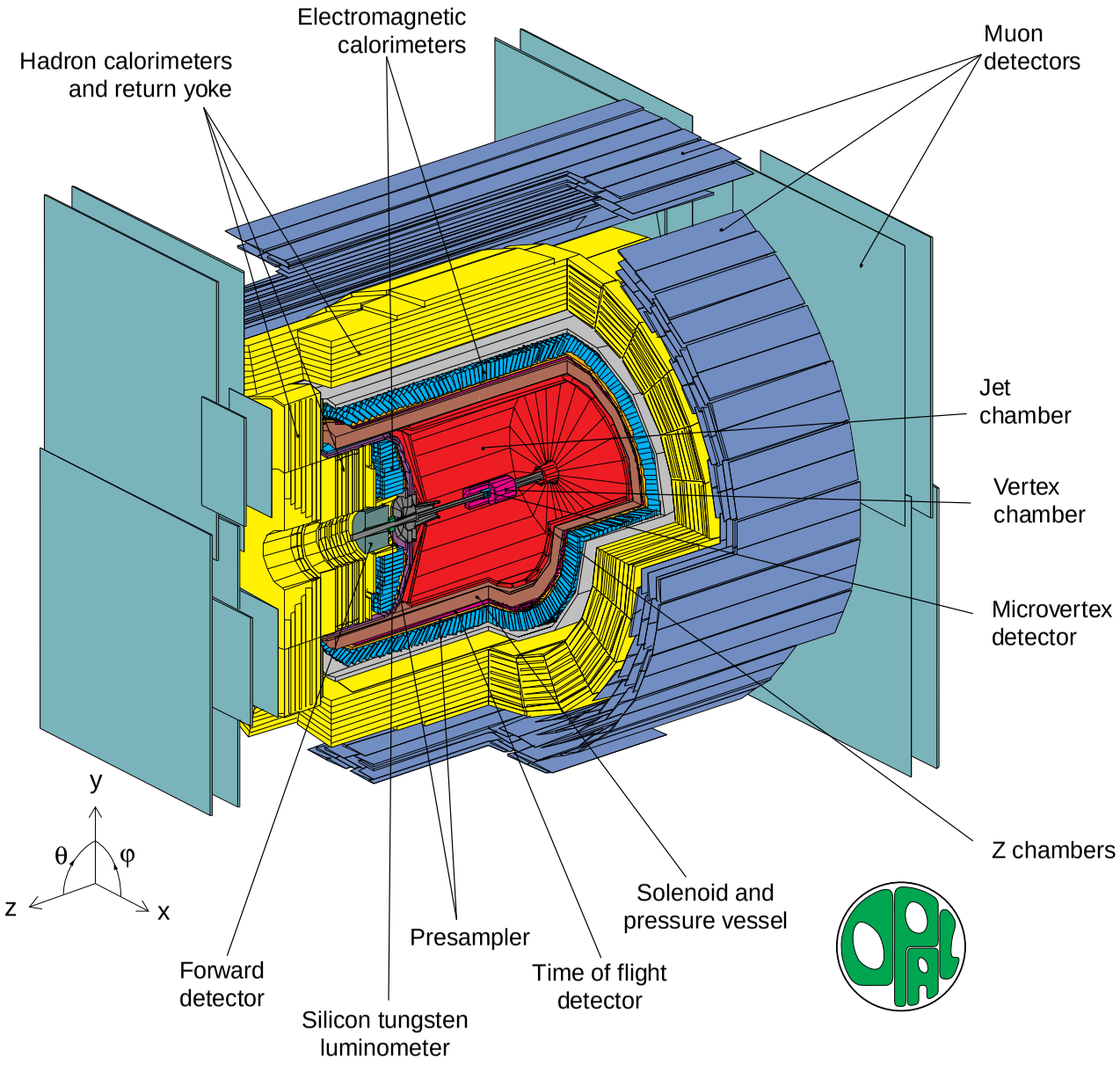

Figure 2.2: The OPAL detector and coordinate system.

the z-axis with the x- and y-axes then forming a right handed system, with an origin at the nominal interaction point. The polar angle θ is measured from the positive z-axis and the azimuthal angle ϕ from the x-axis in the x-y plane. To achieve as close as possible total hermicity, like any such modern detector employed in a collider environment, OPAL was constructed from concentric cylindrical layers of sub-detectors, sealed by two end-cap detectors. Particles moving outwards from the collision vertex would first be tracked by the detectors housed in the central pressure vessel. Outside this was the solenoid, a water cooled aluminium coil carrying 7000 A of current which developed an axial field of 0.435 T. Next came the electromagnetic and then the hadronic calorimetry, the iron of the latter acting as the return yoke for the magnetic field. Only muons and neutrinos would penetrate further than this, the former being seen in the outer-most muon chambers as they escaped the detector and the latter escaping unseen.

The sub-detector of prime importance to this analysis was the electromagnetic calorimeter, though information from the tracking chambers was also employed. The relevant components will now be described in further detail. For a full description of the remaining sub-detectors, the hadronic calorimetry (HCAL) and the muon chambers, refer to [37, 42, 43].

2.2.1 The Tracking System

The purpose of a tracking system is to measure precisely the trajectories of charged particles as they emerge from the interaction point, whilst expending a minimal material budget ahead of the calorimetry. In OPAL, tracking was provided in the form of three drift chambers located within the central pressure vessel, supplemented from 1991 by a silicon micro-vertex detector.

The location of the tracking system inside the solenoid allowed the momentum of charged particles to be deduced from their trajectories. A charged particle moving through a magnetic field experiences a Lorentz force perpendicular to its velocity and the direction of the field. The curved trajectory of a particle of charge $|Q| = 1e$

allows the component of its momentum perpendicular to the field, $p_\perp$, in GeV, to be found from

$$p_\perp = 0.3Br,$$

where r is the radius of curvature in m of the track and B is the magnetic field strength in Tesla. Position measurements along a particle's curved trajectory therefore allow its momentum to be determined, and the direction of the curvature also gives the sign of its charge.

The three drift chambers inside the pressure vessel all operated on the same principle: the detection of the ionisation produced in the gas of the pressure vessel by the passage of the charged particles. This ionisation was detected using planes of anode and cathode wires. The physical location of the anode wires on which signals were induced, combined with the time for the ionised particles to drift there under the influence of the electric field, allowed the trajectories to be determined. Additionally, the actual signal sizes assisted in the identification of the type of particle that caused the ionisation.

The tracking and other subsystems ahead of the calorimetry are described below.

- **The Silicon Micro-Vertex Detector (SI)**

  The silicon micro-vertex detector [44] provided high precision track measurements close to the interaction point and thereby allowed events with secondary decay vertices of short lived particles to be reconstructed. In its final form after two upgrades, the detector consisted of two concentric layers of silicon wafer modules 30 cm long, located at radial distances of 6.5 and 7 cm from the beam axis. By arranging the wafers both parallel and perpendicular to the z-axis the tracks could be reconstructed to a resolution of 10 μm in the r-ϕ plane and about 15 μm in the z-direction. The physics of silicon detectors is discussed further in chapter 5.

- **The Vertex Chamber (CV)**

  The vertex chamber [45] was the inner-most of the three drift chambers housed inside the pressure vessel. Approximately 1 m in length and covering a radius

from 8.0 to 25.5 cm, the CV allowed the tracks found in the SI to be matched to those seen in the middle and outer drift chambers. The cylindrical detector consisted of two concentric layers of chambers each divided into 36 sectors. There were 12 wires parallel to the z-direction in each inner sector and 6 in each outer sector. The latter had a 4° twist to the axial direction and this "stereo" information, combined with the time differences seen between signals measured at each end of the wires, gave a z measurement with a resolution of about 700 μm. Comparing the relative signal sizes in neighbouring wires allowed an r-ϕ resolution of about 50 μm to be achieved.

- **The Jet Chamber (CJ)**

  Occupying most of the space inside the pressure vessel and a large fraction of the total volume of OPAL, the jet chamber [46] was the principal tool used in track reconstruction. Again cylindrical in construction, this detector was 4 m in length, extended in radius from 0.5 to 3.7 m from the beam axis and covered 98% of the solid angle in the polar region $|\cos\theta| < 0.98$. Its volume was divided into 24 sectors each of 15° in azimuth and containing 159 axial sense wires with 10 mm radial separation. In addition to precise ϕ information, extracted from the measured drift times to the wire positions, coarse z information was obtained from the charge collected at each end of the wires. The spatial resolutions in the r-ϕ plane and z direction were then 135μm and 6 cm, respectively.

  The CJ also made use of the total charge collected at each point along the trajectory of a track to calculate the rate of ionisation energy loss by the particle with distance, $\frac{\mathrm{d}E}{\mathrm{d}x}$. This assisted in particle identification, since $\frac{\mathrm{d}E}{\mathrm{d}x}$ has a distinctive dependence on momentum for particles of different type [47].

- **Z Chambers (CZ)**

  The CZ was the outer-most component within the central tracker and was used to improve on the coarse z-coordinate measurement supplied by the jet chamber. The cylindrical layer of drift chambers consisted of 24 sectors in ϕ, each divided into 8 0.5 m lengths. The 6 wires in each cell were arranged radially, achieving a resolution in the z-direction of approximately 300 μm.

- **Barrel Time-of-Flight (TOF) and Tile End-Cap (TE) Detectors**

  Just outside the magnetic coil were located the scintillator arrays which formed the barrel time-of-flight (TOF) system. This was an important tool for the rejection of spurious events not associated with the e^+e^- collisions, such as cosmic rays and possible beam interactions with gas atoms in the pipe. The TOF system comprised 160 scintillators located at a radius of 2.36 m, from which the luminescence was recorded by photo-multiplier tubes. Further layers of scintillators made up the tile end-cap (TE) system which complemented the TOF system in the end-cap regions. These were read-out by optical fibres to photo-multiplier tubes situated outside the magnetic field.

- **The Minimum Ionising Particle Detector (MIP-PLUG)**

  The MIP-PLUG [48] was installed in the forward regions of OPAL in 1997. The four layers of scintillating tiles at ± 2.5 m from the interaction point were designed to detect minimum ionising particles, such as muons, in the angular regions from 40 to 200 mrad from the beam pipe.

2.2.2 Electromagnetic Calorimetry

The role of the electromagnetic (EM) calorimeter [49] was to measure the positions and energies of the electrons, positrons and photons emerging from the central tracker. This was of particular importance for photons, which left no signature in the tracking system. In general, EM calorimeters consist of some dense absorbing medium in which Bremsstrahlung and pair-production combine to cause "showering": incoming electrons and positrons are decelerated and thus radiate photons, which subsequently create further electron-positron pairs, yielding more photons, such that the number of particles increases exponentially with depth into the medium. The showering is curtailed as the energy from the initial particle is expended, with all the energy being dissipated in the material. For a more detailed discussion of this process refer to [50].

The main electromagnetic calorimeter (ECAL) of OPAL was made of lead glass

blocks, within which the electrons and positrons of the shower emitted Čerenkov radiation. This was transmitted through the glass and collected by photo-tubes, with the amount of light corresponding to the amount of activity in the cascade and therefore the energy of the incident particle. Since there were over two radiation lengths of material between the beam pipe and the ECAL, presampler devices were included to estimate the amount of showering and thus the energy loss ahead of the lead glass blocks. These principal components are described below.

- **Lead Glass Electromagnetic Calorimeter**

  The ECAL was made up of some 9 440 lead glass blocks in the barrel section with a further 1 132 being used in each of the end-caps, together allowing electromagnetic objects with energies above 100 MeV to be measured over a polar angular range of $|\cos\theta| < 0.98$. Within the barrel, the Čerenkov light was converted to electrical signals by magnetic field tolerant photo-multiplier tubes. For the end-caps, photo triodes were used since they had to operate in the axial field of the magnet.

  The ECAL was equivalent to over 20 radiation lengths of material and therefore contained the electromagnetic showers. (Hadronic showering would also commence within this distance, meaning that information from the ECAL had to be combined with that from the HCAL to correctly reconstruct any hadronic events.) The intrinsic resolution of the lead glass blocks was approximately $\sigma_E/E \simeq 5\%/\sqrt{E}$ for incoming particles of energy E in GeV, though this was degraded by the effects of the pre-showering.

- **Presamplers**

  There was both a barrel and an end-cap electromagnetic presampler. The barrel presampler consisted of an array of drift tubes whilst the end-cap device comprised multiwire proportional chambers. The hit multiplicity in these gave an estimate of the corrections to be applied to the energy deposits recorded in the ECAL.

Fully hermetic electromagnetic calorimeter coverage down to 24 mrad from the beam axis was provided by further sub-detectors located close to the beam pipe,

ahead of the interaction vertex. These were the gamma catcher, the forward calorimeter (FD) and silicon-tungsten calorimeter (SW):

- **Gamma Catcher**

  This sub-detector was designed to fill the gap between the outer edge of the forward detector and the inner edge of the ECAL end-caps. It comprised two arrangements of lead-scintillator sandwich, covering the regions from 143 to 193 mrad from the beam pipe.

- **Forward Detector (FD)**

  The two modules of the FD [37] were located at ± 2.6 m from the interaction vertex and covered the angles 40-150 mrad from the beam axis. They presented over 20 radiation lengths of material in 35 layers of lead-scintillator sandwich.

- **Silicon-Tungsten Detector (SW)**

  The two modules of this detector [51] were located at ± 2.4 m and consisted of 18 layers of tungsten sandwiched between 19 layers of silicon. The SW provided calorimeter coverage from 54 mrad down to the limit of electromagnetic hermicity at 24 mrad. However, due to the tungsten shield installed in 1996 to protect the tracking chambers from synchrotron radiation, the effective limit of hermicity from this time lay at approximately 33 mrad from the beam.

2.2.3 Data Acquisition

Particle bunch crossings occurred in the detector once every 22 μs, though only some of these contained an actual interaction, or "event". The events of interest were selected using a sequence of fast electronics, starting with the trigger, before being reconstructed by a specialised software package and finally stored.

Triggering

Since the time taken to output the information from all detector subsystems was of order 10 ms, the recording of the information associated with any bunch crossing necessarily introduced a dead-time equivalent to the next several hundred bunch crossings. The trigger system [52] was therefore used to make real time decisions, based on the information from certain sub-detectors, restricting the read-out to only those bunch crossings in which a reaction occurred. A high efficiency for the subset of events that corresponded to physics processes of interest was achieved, whilst filtering out those events corresponding to unwanted backgrounds, such as noise, cosmic rays and interactions between the bunch particles and gas atoms. In the absence of any evidence for genuine physics, the trigger and its input detector systems could all be reset in time for next bunch crossing. The trigger translated the 45 kHz bunch crossing rate to an event rate of just 10 Hz suitable for the subsequent data acquisition chain.

Event Reconstruction

If an event which occurred in a certain bunch crossing was selected by the trigger, a signal flagging that bunch crossing was sent to all sub-detectors. On receipt of this they passed their information on the event to the event builder [53], which outputted event records to the filter [54]. The filter software classified the events by type (multihadron, dilepton, etc) and also performed a second level of rejection. Event information in the form of raw detector signals, such as the signal magnitudes from ECAL photo-tubes, was converted into quantities useful for physics studies, such as particle energies, by the software package ROPE (Reconstruction of OPAL Events) [55], aided by a calibration database (OPCAL). The ROPE output was then stored on disk in the form of Data Summary Tapes (DSTs) for subsequent analysis.

The reaction rate for the e^+e^- collisions at a machine such as LEP, $\frac{dN}{dt}$, is given by

$$\frac{dN}{dt} = \sigma\mathcal{L},$$

where σ is the total interaction cross-section and $\mathcal{L}$ the luminosity. Generally, the luminosity depends on the number of particles per bunch, the size of the bunches, the number of bunches in circulation and the revolution frequency. The integrated luminosity, given by

$$\int \mathcal{L}\, dt = \frac{N}{\sigma},$$

is then a measure of how much data has been taken over a certain period of time, usually expressed in pb^{-1} (where 1b = 1barn = 10^{-28} m^2). At OPAL, the forward detector and the silicon-tungsten detector, also referred to as the luminometers, were used to measure $\int \mathcal{L}\, dt$ by detecting small angle Bhabha scattering events ($e^+e^- \to e^+e^-$). Since the cross-section of this purely QED process can be calculated precisely, $\int \mathcal{L}\, dt$ could be found accurately from the number of events recorded, N.

Typical luminosities at LEP-2 were of order 5×10^{31} $cm^{-2}s^{-1}$. During its lifetime, OPAL recorded more than 1 fb^{-1} of data. The breakdown of this by centre-of-mass energy, $\sqrt{s}$, after 1997 is shown in table 2.1.

Year	$\sqrt{s}$/GeV	$\int \mathcal{L}\, dt/pb^{-1}$
1997	183	57
1998	189	187
1999	192	30
	196	78
	200	79
	202	38
2000	200-209	210

Table 2.1: The integrated luminosity, $\int \mathcal{L}\, dt$, recorded at OPAL by year and centre-of-mass energy, $\sqrt{s}$, from 1997 onwards.

2.3 Monte Carlo Modelling

The analysis of data collected at an experiment such as OPAL usually proceeds by comparison with the expectations obtained from a Monte Carlo event generator. Such a program can be used to generate a random set of events with statistics adhering to theoretically expected distributions. Subsequently, the observation of these events by the detector must also be modelled.

- **Monte Carlo Event Generation**

  A Monte Carlo event generator usually specialises in modelling a specific process. Parameters such as the incident beam particles, the centre-of-mass energy and the particle masses, lifetimes and branching ratios are taken as inputs, and the program will calculate the matrix element and consequently the expected cross-section for the process. A random set of events is outputted, in the form of an event list containing the four-vector and type for every final state particle in each generated event. This is the so called Monte Carlo truth.

- **Detector Simulation**

  Most LEP experiments use the software package GEANT [56] to model how the Monte Carlo truth events will appear in a detector. At OPAL the specially tailored package GOPAL (Geant at OPAL) [57] is employed. This contains information specific to the OPAL detector, such as its geometry and the nature of the materials that made up its volume. GOPAL simulates both the interactions of the generated particles with the various parts of the detector and the responses of each sub-detector to the passage of the particles. It then outputs the signals which would have been seen in the detector had the Monte Carlo events really occurred there. These pseudo-detector signals are processed by ROPE in exactly the same way as real OPAL events, giving reconstructed quantities in DST form that can be compared directly with the data.

2.4 Selection and Modelling of $e^+e^- \to \nu\bar{\nu}\gamma\gamma$

2.4.1 Selecting the $\nu\bar{\nu}\gamma\gamma$ Final State

The previous sections have outlined how the results of e^+e^- collisions at LEP were detected and recorded at OPAL, discarding the subset of uninteresting events. The first step in any analysis of this data is to make further selections from the events stored in the DSTs, in order to obtain those which correspond to the particular physics process of interest. For this work it is the events arising from the $e^+e^- \to \nu\bar{\nu}\gamma\gamma$ process that need to be identified from all those recorded at 183 GeV centre-of-mass energy and above.

The signal in the detector resulting from a $\nu\bar{\nu}\gamma\gamma$ event is just two energy deposits in the ECAL. Essentially this is what the selection routine must search for, though further cuts are needed to suppress unwanted backgrounds. Furthermore, from all the selected two-photon events, it is the subset in which the photons are acoplanar (not back to back) which is required: in this topology there must be some missing energy and momentum, signalling the presence of the neutrinos that escaped the detector unseen. The "sp046" event selection routine that performed these tasks was already available at the start of this work and it is described thoroughly in [58, 59]. Presented below is a brief summary of the main selection criteria.

Initial Candidate Selection Events are initially taken to be candidates if they satisfy either:

- at least two photons, both with energy $E_\gamma > 0.05E_{\text{beam}}$, where E_{beam} is the beam energy, and polar angle θ_γ satisfying $|\cos(\theta_\gamma)| < 0.966$ (referred to as the high energy selection) or,
- at least two photons, one with energy $E_\gamma > 1.75$ GeV, $|\cos(\theta_\gamma)| < 0.8$ and an associated in-time TOF hit, and a second with $E_\gamma > 1.75$ GeV and $|\cos(\theta_\gamma)| < 0.966$ (the low energy selection).

Events with more than two photons are accepted, with all subsequent background vetoes then applying to the two highest energy reconstructed photons.

Rejection of Background Events Background events which pass the initial candidate selection are suppressed using the following cuts:

- For the high energy selection, events containing a final state charged lepton are identified and rejected from hits in the CJ, CV and SI chambers. However, the selection is designed to retain the acceptance of events in which one or both photons converted within the jet chamber detectors. The low energy selection does not permit such photon conversions and demands there be no charged track in the event with 20 or more CJ hits.

- Events with two forward going electrons (common Bhabha scattering events) or muons accompanied by two photons are rejected using hit information from the forward calorimeters and the MIP-PLUG. However, very low angle Bhabhas could miss the inner edge of the SW and still take away several GeV of transverse momentum, leaving a $\gamma\gamma$ system with missing energy and no other detector signals. Such events are rejected by the requirement that $p_T^{\gamma\gamma} > 0.05 E_{\rm beam}$, where $p_T^{\gamma\gamma}$ is the transverse momentum of the system of the two highest energy photons.

- A number of procedures are implemented to cut against the cosmic ray background. Events with any muon track segments in the muon chambers or HCAL are rejected, and this also suppresses backgrounds from beam halo muons. Out of time hits in the ECAL are also associated with cosmic muons. Additionally, the candidate clusters have to satisfy certain quality criteria in terms of their extent and separation, in order to cut against muons that grazed the ECAL leaving extended energy deposits. Finally, events are rejected if the total cluster energy is found to exceed the beam energy.

Identification of Acoplanar Photon Pair Events Events that pass all of the above cuts are selected from DSTs and written to the sp046 ntuples [60] for analysis.

At this stage these include all events with two or more photons in the final state. The subset of acoplanar photon pair events are flagged if they satisfy all of the following criteria:

- The total visible ECAL energy is less than 95% of $\sqrt{s}$.
- The missing momentum vector calculated from the two highest energy photon candidates satisfies $|\cos\theta_{\mathrm{missing}}| < 0.95$.
- The acoplanarity angle, ϕ_{aco}, given by $\phi_{\mathrm{aco}} = ||(\phi_1 - \phi_2)| - 180^\circ|$, where ϕ_1 and ϕ_2 are the azimuthal angles of the two highest energy clusters, satisfies $\phi_{\mathrm{aco}} > 2.5^\circ$.
- For events with three final state photons, the sum of the three opening angles must be less than 350° and the transverse momentum greater than $0.1E_{\mathrm{beam}}$.

The efficiency for Standard Model $e^+e^- \to \nu\overline{\nu}\gamma\gamma(\gamma)$ events within the kinematic acceptance of the acoplanar photon pair selection is approximately 66 %. Refer to [59] for further details on this point. The combined expected background contribution from Standard Model processes other than $e^+e^- \to \nu\overline{\nu}\gamma\gamma(\gamma)$, cosmic rays and beam-related backgrounds is less than 1 % [58, 59].

2.4.2 Modelling the $\nu\overline{\nu}\gamma\gamma$ Final State with NUNUGPV

The $e^+e^- \to \nu\bar{\nu}\gamma\gamma$ process is modelled by the NUNUGPV Monte Carlo generator [61, 62]. All the tree-level Standard Model Feynman diagrams contributing to the process are included in this program. The contributions from the AQGC diagrams shown in figure 1.8 are also implemented, with the couplings a_0^{W}, $a_{\mathrm{c}}^{\mathrm{W}}$ and a_0^{Z}, $a_{\mathrm{c}}^{\mathrm{Z}}$ and the energy scale Λ being controlled by the user. The program makes the appropriate addition of the Standard Model and AQGC matrix elements to obtain the resulting cross-section as a function of the anomalous couplings.

Although NUNUGPV models only the $\nu\overline{\nu}\gamma\gamma$ final state, following their simulation in GOPAL the generated events must be subjected to the same selection criteria

as the data, since applying the cuts of 2.4.1 causes some genuine $e^+e^- \to \nu\bar{\nu}\gamma\gamma$ events to be lost.

Figure 2.3 shows the distributions of the energies and polar angles of the two photons in the data and NUNUGPV Standard Model Monte Carlo events passing the acoplanar photon pair selection. Additional cuts on the photon energies and angles have been applied, which are necessary due to the cuts imposed on the Monte Carlo events at generation time (refer to section 3.4). Good agreement is seen between the Standard Model expectation and the data, as has been reported elsewhere [27, 63].

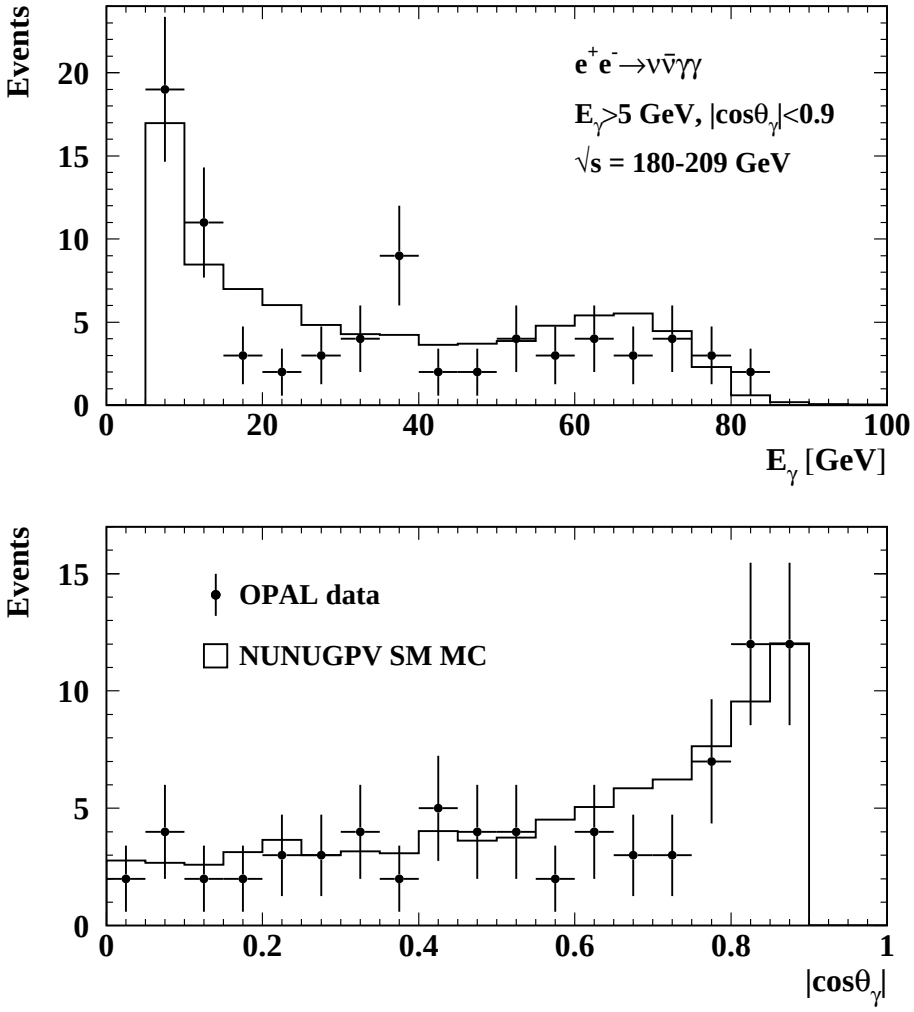

Figure 2.3: The distributions of the photon energy, E_γ, and polar angle, $|\cos\theta_\gamma|$, in the acoplanar photon pair events in the data compared to the Standard Model NUNUGPV Monte Carlo prediction. Note that each event contributes two photons to each distribution.

Chapter 3

Measuring the Anomalous Quartic Gauge Couplings

The sensitivity of the $e^+e^- \to \nu\overline{\nu}\gamma\gamma$ process to the possible WW$\gamma\gamma$ and ZZ$\gamma\gamma$ anomalous couplings is exploited in order to constrain the four parameters a_0^W, a_c^W, a_0^Z and a_c^Z. The binned maximum likelihood method employed is described in this chapter. Independent Monte Carlo samples are used to parametrise the effects of the AQGCs and further cuts are imposed to enhance their significance compared to the Standard Model contribution. The binning of the likelihood function is then optimised taking into account the systematic uncertainties, the identification and treatment of which are also reported here.

3.1 Standard Model Expectation for $\nu\overline{\nu}\gamma\gamma$

The expected Standard Model cross-sections for $\nu\overline{\nu}\gamma\gamma$ events passing the selection of section 2.4.1 have been evaluated using fully simulated NUNUGPV events generated with the anomalous couplings set to zero. At each centre-of-mass energy, the cross-section is found from the re-weighting of many different Monte Carlo samples as explained in section 3.4. The corresponding number of events expected by centre-of-mass energy are shown in table 3.1, based on the integrated luminosities also

listed. The luminosities quoted here take into account the detector status cuts appropriate for the $\nu\overline{\nu}\gamma\gamma$ final state and as such are slightly lower than the values given in table 2.1. This reduction is due to the occasional times when sub-detectors necessary for the recording of the $\nu\overline{\nu}\gamma\gamma$ events were not functioning properly.

All Monte Carlo expectations have been corrected to account for random coincidental activity in the detector which would have caused some real data events to fail the selection criteria. These events could arise from in-time cosmic rays passing through the detector, from randomly-occurring collisions of beam electrons with the beam pipe walls or residual gas molecules inside the beam pipe, or from detector noise [27]. The rate and characteristics of the events have been evaluated using samples of random beam-crossings collected throughout the data-taking periods [64]. Approximately 4.0-4.7% of the $\nu\overline{\nu}\gamma\gamma$ events, depending on the centre-of-mass energy, are expected to fail the selection if these unmodelled extra contributions are included: this was taken into account by applying a multiplicative factor of 0.953 - 0.960, as appropriate, to all Monte Carlo accepted cross-sections at a given energy.

To suppress the Standard Model contribution, principally the forward-peaked doubly-radiative return process, the following additional cuts were applied to the events passing the acoplanar photon pair selection:

- The energies of the highest and second highest energy reconstructed photons, $E_{\gamma 1}$ and $E_{\gamma 2}$, respectively, must both be greater than 10 GeV. This cut has little effect on the anomalous quartic coupling contribution, which gives rise predominantly to photons of high energy, but does help suppress the doubly-radiative return background.

- $|\cos\theta_{\gamma 1}| < 0.9$, $|\cos\theta_{\gamma 2}| < 0.9$, where $\theta_{\gamma 1}$ and $\theta_{\gamma 2}$ are the polar angles of the highest and second highest energy reconstructed photons. This requirement again helps suppress the doubly-radiative return background, which is forward peaked as expected for initial-state radiation photons.

No improvement in the sensitivity to the anomalous couplings could be gained by adjusting these suppression cuts in the optimisation procedure described in sec-

tion 3.5. All subsequent references to the accepted events refer to those passing both the acoplanar photon pair selection and the Standard Model suppression cuts. The number of events expected after these cuts at each centre-of-mass energy are shown in table 3.1.

$\sqrt{s}$ /GeV	$\int \mathcal{L}\, \mathrm{d}t$ /pb^{-1}	NUNUGPV Acoplanar Photon Pair Selection plus $E_\gamma > 10$ GeV, $\lvert\cos\theta_\gamma\rvert < 0.9$
183	54	2.5
189	175	7.9
192	29	1.3
196	72	3.1
200	74	3.0
202	37	1.5
206	211	8.3
183-206	652	27.6

Table 3.1: The number of expected events in the Standard Model corresponding to the integrated luminosities, $\int \mathcal{L}\, \mathrm{d}t$, at each centre-of-mass energy, corrected for the detector status. The full acoplanar photon pair selection of 2.4.1 and the Standard Model suppression cuts have been applied to the fully simulated NUNUGPV events.

3.2 Sensitivity of the $\nu\overline{\nu}\gamma\gamma$ Final State to AQGCs

In addition to the total cross-section for $e^+e^- \to \nu\overline{\nu}\gamma\gamma$ varying with the AQGC parameters, any anomalous couplings are also expected to affect the shapes of the distributions of certain observable quantities, as described below.

Total Cross-Section

The quadratic dependence of the total accepted cross-section on each of the anomalous coupling parameters is shown in figure 3.1. The sensitivity to the AQGCs increases with centre-of-mass energy.

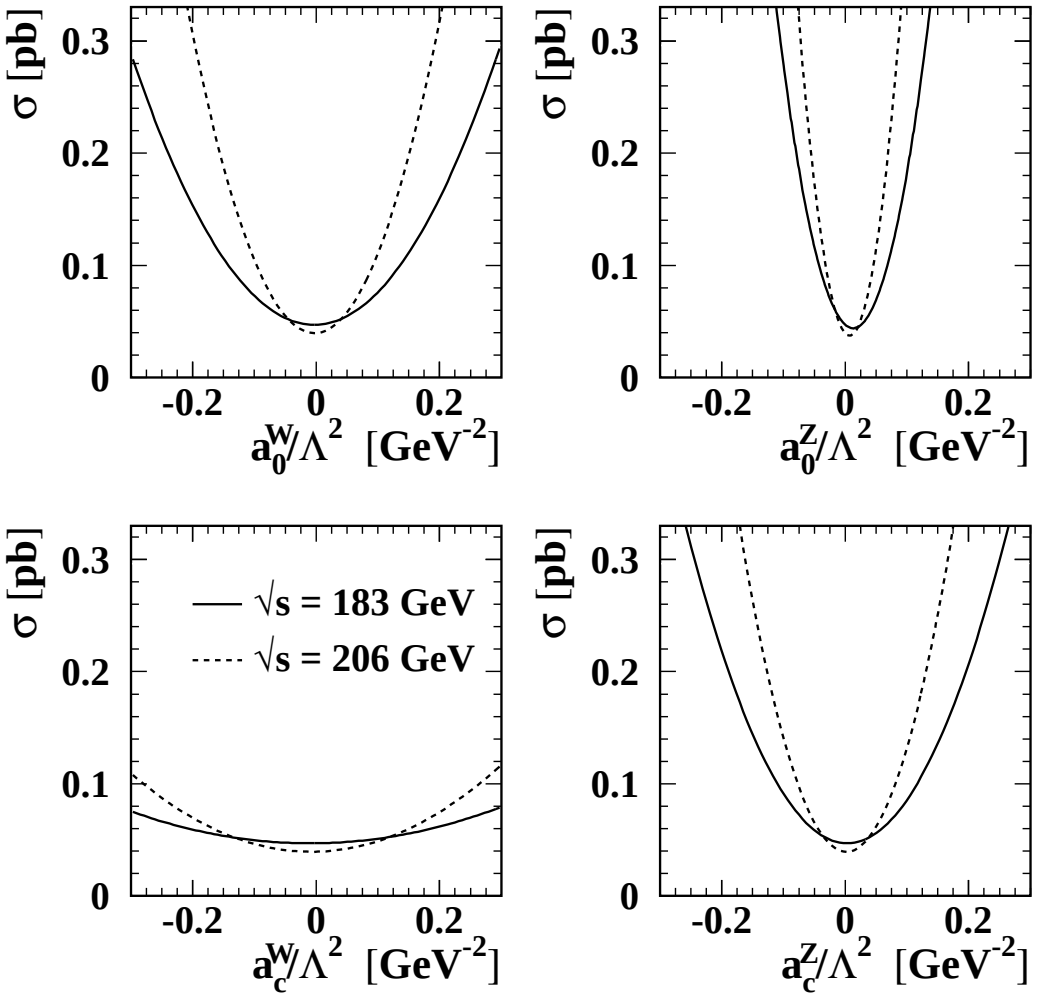

Figure 3.1: The dependence of the cross-section for $e^+e^- \to \nu\overline{\nu}\gamma\gamma$ on each of the four anomalous coupling parameters at 183 and 206 GeV centre-of-mass energies. The predictions of NUNUGPV have been simulated in the OPAL detector and the full acoplanar photon pair selection cuts applied.

The Recoil Mass Distribution

For the $e^+e^- \to \nu\overline{\nu}\gamma\gamma$ process, it is instructive to plot the distribution of the invariant mass of the neutrino system that recoils against the photons, referred to as the recoil mass distribution. The recoil mass, M_{rec}, is calculated from

$$\begin{aligned} M^2_{\text{rec}} &= E^2_{\nu\bar{\nu}} - p^2_{\nu\bar{\nu}} \\ &= E^2_{\text{missing}} - p^2_{\gamma\gamma}. \end{aligned}$$

The energy of the neutrino system, $E_{\nu\bar{\nu}}$, is given by the missing energy, E_{missing}, the difference between the centre-of-mass energy and the energy of the photon system detected by the ECAL. The magnitude of the momentum of the neutrino system, $p_{\nu\bar{\nu}}$, is equal to that of the photon system, $p_{\gamma\gamma}$, which is calculated from their energies using the θ and ϕ information also gathered from the ECAL.

The expected recoil mass distributions in the Standard Model scenario and in two possible anomalous $WW\gamma\gamma$ and $ZZ\gamma\gamma$ quartic coupling hypotheses are shown in figure 3.2. These are each based on 2 000 fully simulated events from NUNUGPV subject to the full acceptance cuts. The dominating Standard Model contribution to the cross-section, arising from the doubly-radiative return process leaving a Z to decay to two neutrinos, is apparent from the peak in M_{rec} centred on the Z mass. The contribution from the Standard Model WW fusion diagrams is found to the right of this peak [65]. Radiative return events in which a third photon escapes detection along the beam pipe, giving additional missing energy, also make a small contribution in this region.

There is a clear difference between the effects of W and Z couplings on the recoil mass distribution. Increasing the coupling a_0^{Z} at the anomalous $ZZ\gamma\gamma$ vertex has the effect of increasing the cross-section almost exclusively in the region around the Z mass peak, exactly as expected from the diagram shown in figure 1.8. A similar effect is observed for a_{c}^{Z}. In contrast, the effect of the anomalous $WW\gamma\gamma$ vertex is seen mainly in the region of the M_{rec} distribution to the left of the Z mass peak. Again, similar effects are seen for a_0^{W} (plotted) and a_{c}^{W}. Thus, different regions of the recoil mass plot are sensitive to the different possible anomalous processes.

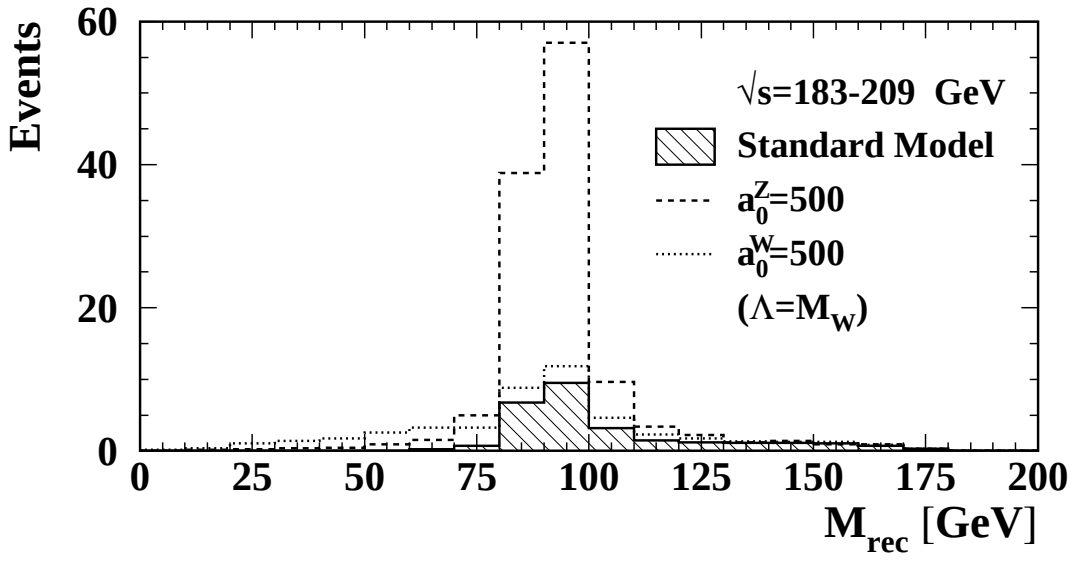

Figure 3.2: The recoil mass distributions for the accepted $\nu\overline{\nu}\gamma\gamma$ events in the Standard Model and with possible WW$\gamma\gamma$ and ZZ$\gamma\gamma$ anomalous couplings.

The Photon Energy Distributions

The recoil mass is not the only distribution with a shape sensitive to the AQGCs. The distributions of the reconstructed energies of the two highest energy photons, $E_{\gamma 1}$ and $E_{\gamma 2}$, also depend on the anomalous couplings. Studies of $E_{\gamma 1}$ and $E_{\gamma 2}$ indicated that the distribution of the energy of the second highest energy reconstructed photon offered the greatest sensitivity to any anomalous contribution. The effects of the different AQGC vertices on $E_{\gamma 2}$ are shown in figure 3.3.

3.3 The Binned Maximum Likelihood Method

The maximum likelihood method is a procedure suited to problems in which there are insufficient data to satisfy Gaussian statistics [66]. The method is applied here to constrain the AQGCs using the information contained in the total cross-section for $e^+e^- \to \nu\overline{\nu}\gamma\gamma$ and the $M_{\rm rec}$ and $E_{\gamma 2}$ distributions. Consider the events at one

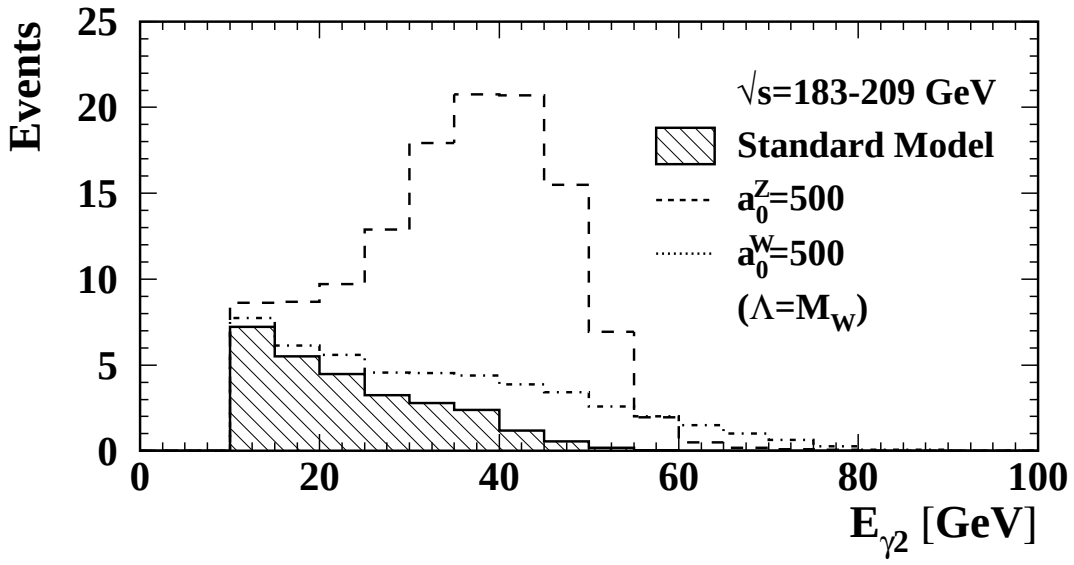

Figure 3.3: The distributions of the second highest reconstructed photon energy for the accepted $\nu\overline{\nu}\gamma\gamma$ events, in the Standard Model and with possible WW$\gamma\gamma$ and ZZ$\gamma\gamma$ anomalous couplings.

centre-of-mass energy in the case where a single anomalous parameter, a, can vary. It is assumed that the probability, P_i, for an event to fall into some bin, i, in the two-dimensional $M_{\rm rec}$ versus $E_{\gamma 2}$ distribution depends on a in a known way:

$$P_i = P_i(M_{\rm rec}, E_{\gamma 2}; a).$$

Then, if n_i is the number of data events in bin i, the likelihood function, $L(a)$, is given by

$$L(a) = f(N_{\rm obs}, N_{\rm ex}(a)) \prod_i P_i(a)^{n_i},$$

where the product is over all the bins and the extra term $f(N_{\rm obs}, N_{\rm ex}(a))$ normalises the likelihood to the total number of data events seen ($N_{\rm obs} = \sum_i n_i$). This normalisation term is the Poisson probability for having $N_{\rm obs}$ events in the data when $N_{\rm ex}(a)$ are expected for that value of the coupling and is given by

$$f(N_{\rm obs}, N_{\rm ex}(a)) = \frac{N_{\rm ex}(a)^{N_{\rm obs}} e^{-N_{\rm ex}(a)}}{N_{\rm obs}!}.$$

It is through this Poisson term that the information from the total cross-section is included in the likelihood function.

By construction, $L(a)$ is the likelihood of obtaining the overall data set with the parameter value a. However, by the theory of Bayes [67], finding the maximum of $L(a)$ yields the most likely value of a given the data collected. In the instance where the likelihood has a Gaussian dependence on the parameter a,

$$L(a) = Ce^{\frac{-(a-a_0)^2}{2\sigma^2}},$$

taking the natural log gives a parabola,

$$\ln L(a) = \ln C - \frac{(a-a_0)^2}{2\sigma^2},$$

which has a maximum at a_0. Since both $L(a)$ and $\ln(L(a))$ are maximised for the same value of a it is usual to work with $-\ln L(a)$ and seek the minimum of this, neglecting the constant $\ln C$ term. It is trivial to show that the points at $a_0 + \sigma$ and $a_0 - \sigma$ on the Gaussian likelihood curve map to the points on the parabola where $-\ln L(a)$ has increased by 0.5 from its minimum at $-\ln L(a_0)$. Similarly, the 95% confidence level limits on a_0, the points on the Gaussian at $a_0 + 1.96\sigma$ and $a_0 - 1.96\sigma$, correspond to an increase of 1.92 from the minimum of $-\ln L(a)$. In the case where two parameters, a_1 and a_2, can vary, $-\ln L(a_1, a_2)$ is a surface in three-dimensions describing the shape of a bowl. If the likelihood is Gaussian, the bowl is parabolic and contours can be drawn though the points of equal likelihood which are ellipses in the $a_1 - a_2$ plane. It can be shown that the contour containing 95% of the probability lies at $\Delta \ln L = 3.0$ above the minimum.

When extended to all centre-of-mass energies, the statistical $-$ln-likelihood function for a single AQGC parameter is given by

$$-\ln L(a) = -\sum_E \left(\sum_i n_i^E \ln P_i^E(a) + [N_{\text{obs}}^E \ln N_{\text{ex}}^E(a) - N_{\text{ex}}^E(a)] \right), \tag{3.1}$$

neglecting constant terms. The outer summation is over the centre-of-mass energies, E, and the sum in the first term is over the bins in the $(M_{\text{rec}}, E_{\gamma 2})$ plane. In this first term, n_i^E is now the number of data events observed in bin i at energy E. $P_i^E(a)$ is

given by

$$P_i^E(a) = \frac{\sigma_i^E(a)}{\sigma_{\rm total}^E(a)},$$

in which $\sigma_{\rm total}^E(a)$ is the total cross-section at energy E and $\sigma_i^E(a)$ the cross-section within bin i, as functions of a. The first term in $-\ln L(a)$ therefore makes use of only the shape information in the $M_{\rm rec}$ and $E_{\gamma 2}$ distributions. The second term originates from the Poisson normalisation. When the $-\ln$-likelihood function is not parabolic, a Gaussian approximation is used by MINUIT [68], the CERN numerical minimisation program, in the assignment of confidence limits.

3.4 Monte Carlo Templates and Reweighting

For the anomalous coupling parameters to be constrained when they can be varied together, the full $-\ln$-likelihood function, $-\ln L(a_0^{\rm W}, a_{\rm c}^{\rm W}, a_0^{\rm Z}, a_{\rm c}^{\rm Z})$, must be constructed. This requires the functional behaviour of the binned and total cross-sections on all four coupling parameters to be known, at each centre-of-mass energy. Since the cross-sections vary quadratically with each parameter independently, 15 Monte Carlo templates generated with different values of the couplings are sufficient to fully parametrise $\sigma_i^E(a_0^{\rm W}, a_{\rm c}^{\rm W}, a_0^{\rm Z}, a_{\rm c}^{\rm Z})$ and $\sigma_{\rm total}^E(a_0^{\rm W}, a_{\rm c}^{\rm W}, a_0^{\rm Z}, a_{\rm c}^{\rm Z})$. The 15 samples of 2 000 events generated at each of 183, 189, 192, 196, 200, 202 and 206 GeV centre-of-mass energies are listed in table 3.2. In producing these, generator level cuts of $E_\gamma > 3.5$ GeV and $|\cos\theta_\gamma| < 0.92$ were imposed on both photons. These cuts were chosen sufficiently far from the cuts on the reconstructed quantities to ensure that the detector simulation was unable to smear any events excluded at generator level into the kinematically accepted region.

The available Monte Carlo statistics were maximised using a reweighting routine provided with the Monte Carlo generator [69]. This is a common Monte Carlo technique used to reduce the number of events that actually have to be generated. Here, at each centre-of-mass energy, every sample has been reweighted to correspond to each of the other 14 settings of the anomalous coupling parameters.

Sample Number, s	a_0^{W}	$a_{\mathrm{c}}^{\mathrm{W}}$	a_0^{Z}	$a_{\mathrm{c}}^{\mathrm{Z}}$
1 (Standard Model)	0	0	0	0
2	+500	0	0	0
3	−500	0	0	0
4	0	+1500	0	0
5	0	−1500	0	0
6	0	0	+500	0
7	0	0	−500	0
8	0	0	0	+1500
9	0	0	0	−1500
10	+500	+1500	0	0
11	+500	0	+500	0
12	+500	0	0	+1500
13	0	+1500	+500	0
14	0	+1500	0	+1500
15	0	0	+500	+1500

Table 3.2: The NUNUGPV Monte Carlo samples. These 15 samples each containing 2 000 generated events were made for each of the seven centre-of-mass energies studied. For the values of the parameters shown it was assumed that the energy scale $\Lambda = M_{\mathrm{W}}$.

The probability for a single Monte Carlo event, k, to occur depends on the square of the matrix element, $|M_k(a_{\mathrm{gen}})|^2$, where a_{gen} denotes the values of the couplings with which the event was generated. The number of events or weight, w_k, the same event would correspond to if it were to occupy the same point in phase space under a different coupling scenario, a_{nequiv}, is equal to

$$w_k = \frac{|M_k(a_{\mathrm{rw}})|^2}{|M_k(a_{\mathrm{gen}})|^2}. \tag{3.2}$$

Thus, the four-vectors for the final state particles of every event in a reweighted sample are identical to those in the generated sample, but the weight of each event changes according to the relative probability of it being obtained under the new coupling values.

Consider the particular case of obtaining the cross-section in each bin of the likelihood function in the coupling scenario $a_0^{\rm W} = 500$ and $a_{\rm c}^{\rm W} = a_0^{\rm Z} = a_{\rm c}^{\rm Z} = 0$. This is modelled by sample 2 but by applying (3.2) to the events of every other sample the information from all available Monte Carlo can be used. (The reweighting of sample 2 itself leaves it unchanged.) The sum of the weights falling into bin i in each sample then gives the cross-section in that bin from that sample. Subsequently, these can be averaged to give the overall binned cross-section, $\sigma_i(500, 0, 0, 0)$.

Caution needs to be taken when the reweighting attempts to populate a region of phase space that was not well covered in the original events. If bin i, for example, lies in the low recoil mass region of the $M_{\rm rec}$ distribution, then in the Standard Model scenario (sample 1) it will contain very few events. When these are reweighted to the scenario in which the WW$\gamma\gamma$ coupling has been turned up, the result is a few events gaining very large weights, for which the statistical errors will be very large. This is taken into account by applying a factor $N^s_{{\rm eq},i}$ to the reweighted binned cross-section σ_i^s from each sample s. $N^s_{{\rm eq},i}$ is the number of equivalent events [70] from sample s in bin i and is given by

$$N^s_{{\rm eq},i} = \frac{(\sum_k w_k^s)^2}{\sum_k (w_k^s)^2},$$

in which the w_k^s are the weights of the events from sample s falling into the bin. Thus, the overall reweighted binned cross-section for bin i is given by

$$\sigma_i = \frac{\sum_s^{15} N^s_{{\rm eq},i} \sigma_i^s}{\sum_s^{15} N^s_{{\rm eq},i}}$$

where the sum is over the 15 samples. In this way, fully reweighted templates for the binned and total cross-sections at each of the 15 points in $(a_0^{\rm W}, a_{\rm c}^{\rm W}, a_0^{\rm Z}, a_{\rm c}^{\rm Z})$ space, at each centre-of-mass energy, have been obtained. It is then from these that the quadratic dependence of the cross-section in each bin and overall is extracted.

3.5 Incorporation of Systematic Effects and Optimisation of Binning

The $-\ln$-likelihood function defined in equation (3.1) reflects only the statistical tolerance of the analysis. Additional systematic uncertainties will broaden the function and thereby loosen any derived confidence limits. Systematic uncertainties are incorporated through the following modifications. The basic transformation is

$$-\ln L(a) \rightarrow -\ln L(a, y_j) + \sum_j \frac{y_j^2}{2},$$

where y_j is one of a set of free parameters $\{y_1, y_2, .. \, y_p\}$ associated with the p independent sources of systematic uncertainty and is given a Gaussian constraint. For a single source of systematic error, there is just one extra parameter y and the binned and total cross-sections transform as

$$\begin{aligned} \sigma_i^E(a) &\rightarrow \sigma_i^E(a, y) = \sigma_i^E(a, 0) + y(\Delta\sigma_i^E) \\ \sigma_{\rm total}^E(a) &\rightarrow \sigma_{\rm total}^E(a, y) = \sigma_{\rm total}^E(a, 0) + y(\Delta\sigma_{\rm total}^E) \end{aligned}$$

where $\Delta\sigma_i^E$ and $\Delta\sigma_{\rm total}^E$ are the expected errors on the binned and total cross-sections, respectively, introduced by the systematic uncertainty. These are evaluated at the Standard Model values of the couplings. Thus, the shape term becomes

$$P_i^E(a, y) = \frac{\sigma_i^E(a, 0) + y(\Delta\sigma_i^E)}{\sigma_{\rm total}^E(a, 0) + y(\Delta\sigma_{\rm total}^E)}.$$

Any uncertainty $\Delta\sigma_{\rm total}^E$ produces a corresponding uncertainty in the total number of expected events, $\Delta N_{\rm ex}^E$, which prompts

$$N_{\rm ex}^E(a) \rightarrow N_{\rm ex}^E(a, y) = N_{\rm ex}^E(a, 0) + y\Delta N_{\rm ex}^E, \tag{3.3}$$

in the normalisation term.

The optimisation of the binning, not yet made explicit in the above formalism, was performed in a quantitative way through the use of Standard Model Monte Carlo samples as data-like input to the fit. In this procedure, the Standard Model samples themselves were excluded from the parametrisation of the cross-section.

Figure 3.4 shows the resulting likelihood curves for each parameter for a selection of possible binning choices. In each case the coupling parameters not varied were kept fixed at their Standard Model values (zero). As expected, the most likely value of the coupling being varied was always found to be zero. More binning possibilities

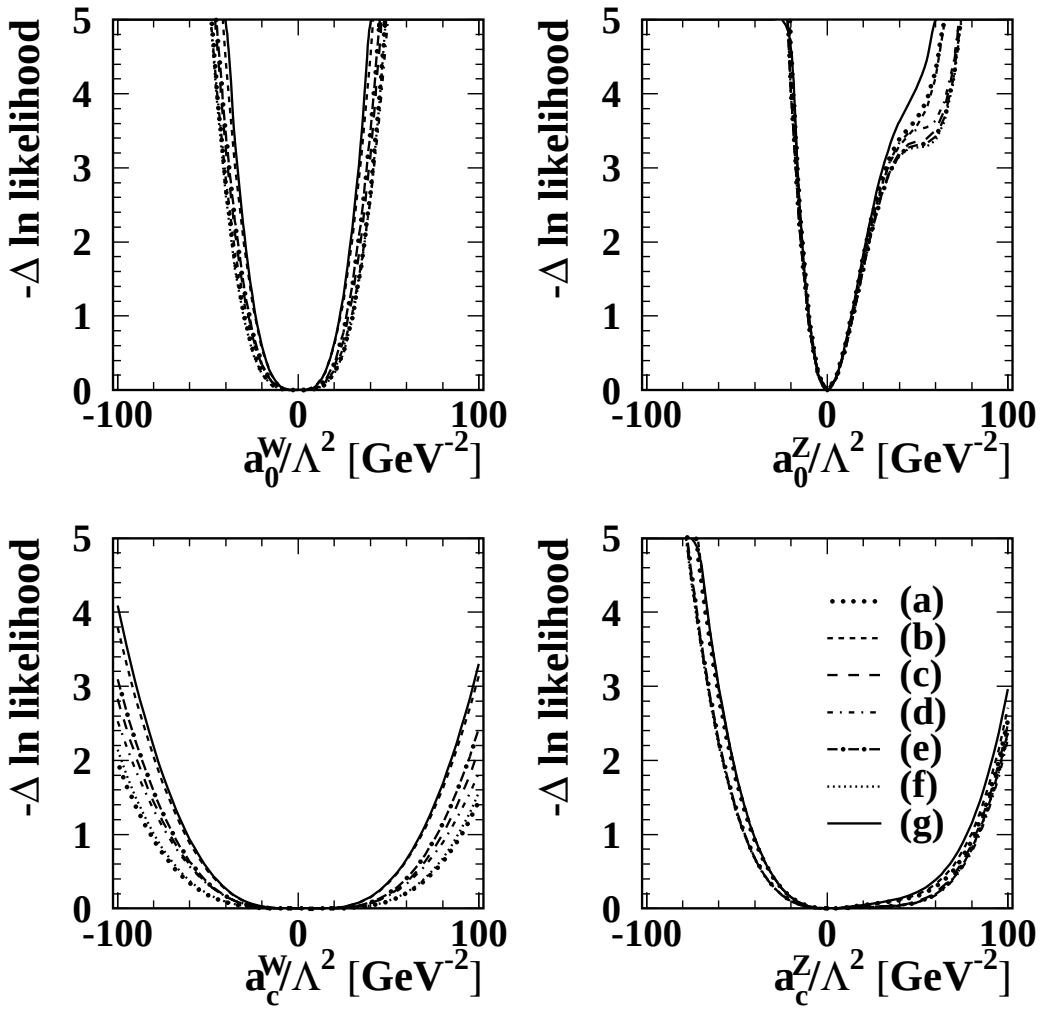

Figure 3.4: The one-dimensional likelihood curves for each of the anomalous coupling parameters obtained by inputting Standard Model Monte Carlo to the fit. Many more than the 7 (a-g) binning scenarios shown here were tested. Case (g) represents the optimal 10-bin final choice.

than those shown in figure 3.4 were studied but the scenario (g) was always found to yield the tightest limits on all four couplings. This optimisation of sensitivity was performed inclusive of systematic effects, the discussion of which is simplified if the optimal binning choice (g) is stated here:

1	$0 < M_{\rm rec} < 60$ GeV	and	$10 < E_{\gamma 2} < 25$ GeV
2	$0 < M_{\rm rec} < 60$ GeV	and	$25 < E_{\gamma 2} < 45$ GeV
3	$0 < M_{\rm rec} < 60$ GeV	and	$E_{\gamma 2} > 45$ GeV
4	$60 < M_{\rm rec} < 80$ GeV	and	$10 < E_{\gamma 2} < 25$ GeV
5	$60 < M_{\rm rec} < 80$ GeV	and	$25 < E_{\gamma 2} < 45$ GeV
6	$60 < M_{\rm rec} < 80$ GeV	and	$E_{\gamma 2} > 45$ GeV
7	$80 < M_{\rm rec} < 120$ GeV	and	$10 < E_{\gamma 2} < 25$ GeV
8	$80 < M_{\rm rec} < 120$ GeV	and	$25 < E_{\gamma 2} < 45$ GeV
9	$80 < M_{\rm rec} < 120$ GeV	and	$E_{\gamma 2} > 45$ GeV
10	$M_{\rm rec} > 120$ GeV		

This choice is consistent with the differing effects of the anomalous couplings on the $M_{\rm rec}$ and $E_{\gamma 2}$ distributions, as illustrated in figure 3.5. Events lying in bins 7, 8 and 9 in the recoil mass are sensitive to the enhancement of the Z mass peak as the ZZ$\gamma\gamma$ coupling is increased. Conversely, bins 1, 2 and 3 are sensitive primarily to the anomalous WW$\gamma\gamma$ vertex. The intermediate bins 4, 5 and 6 help isolate these two regions, preserving their sensitivities to their associated couplings. Events in the region of the $(M_{\rm rec}, E_{\gamma 2})$ plane covered by bin 10 showed little dependence on any of the anomalous couplings and left unisolated this region would serve only to dilute the overall sensitivity of the likelihood function. The cuts at 25 and 45 GeV in the $E_{\gamma 2}$ distribution select the region where the ZZ$\gamma\gamma$ couplings dominate and isolate the tail of the distribution where the WW$\gamma\gamma$ couplings have the greatest influence. Any finer bin granularity was prohibited by the constraint that the total number of equivalent events in each bin i, $\sum_s N^s_{{\rm eq},i}$, should remain 10 or more, where the sum is over all fifteen of the reweighted Monte Carlo samples.

The Standard Model suppression cuts on the photon energies and angles were also considered while testing the different binning scenarios; however, no adjustment was found to result in an improvement in sensitivity.

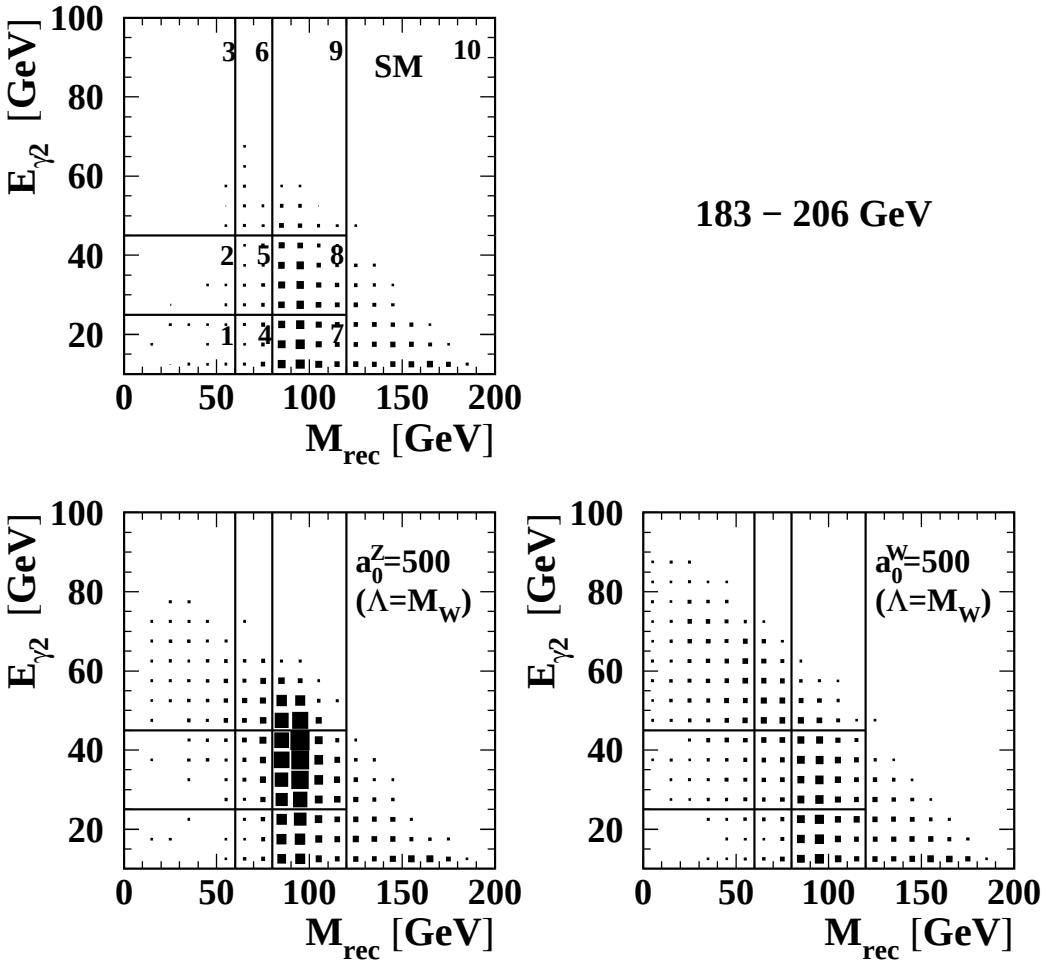

Figure 3.5: The optimal binning of $(M_{\mathrm{rec}}, E_{\gamma 2})$ superimposed on the expected shapes of the two-dimensional distribution in the Standard Model and anomalous WW$\gamma\gamma$ and ZZ$\gamma\gamma$ quartic coupling scenarios. The AQGC distributions have been normalised to the Standard Model expectation.

3.6 Sources of Systematic Uncertainty

Energy Scale and Resolution Uncertainty

The main experimental source of systematic uncertainty arose from the accuracy of the modelling of the energy scale and resolution of the ECAL. The evaluation of this was based on a comparison of reconstructed events with two beam energy photons in the final state with those simulated by the RADCOR [71] Monte Carlo generator. The $e^+e^- \to \gamma\gamma$ events were selected from those passing the sp046 two photon selection by applying the following criteria:

- $E_\gamma > E_{\rm beam}/2$ and $|\cos(\theta)| < 0.9$ for both photons
- $|\cos(\theta_1) + \cos(\theta_2)| < 0.01$ and $||(\phi_1 - \phi_2)| - \pi| < 0.02$, where $\theta_{1,2}$ and $\phi_{1,2}$ are the polar and azimuthal angles of the two photons, respectively, since the two photons should be back to back
- less than 40 CJ hits near the clusters, since there should be no charged particle tracks

The comparison was performed separately for the barrel ($|\cos(\theta_\gamma)| < 0.7$) and end-cap ($0.7 < |\cos(\theta_\gamma)| < 0.9$) regions of the detector and for each year of data-taking. The results are shown in figure 3.6. By fitting Gaussians over a 2σ range of the data and Monte Carlo photon energy distributions, correction factors $C_{\rm R}$ and $C_{\rm S}$ for the energy resolution and scale, respectively, were found from

$$C_{\rm R} = \frac{\text{width of reconstructed data energy distribution}}{\text{width of reconstructed MC energy distribution}},$$
$$C_{\rm S} = \frac{\text{centre of reconstructed data energy distribution}}{\text{centre of reconstructed MC energy distribution}}.$$

The values of $C_{\rm R}$ and $C_{\rm S}$ for the barrel and end-cap parts are given by year in table 3.3: the energy scale of the detector is well modelled for all years, but the fits reveal poor resolution modelling in the barrel region for 1998 and in the end-cap for 2000.

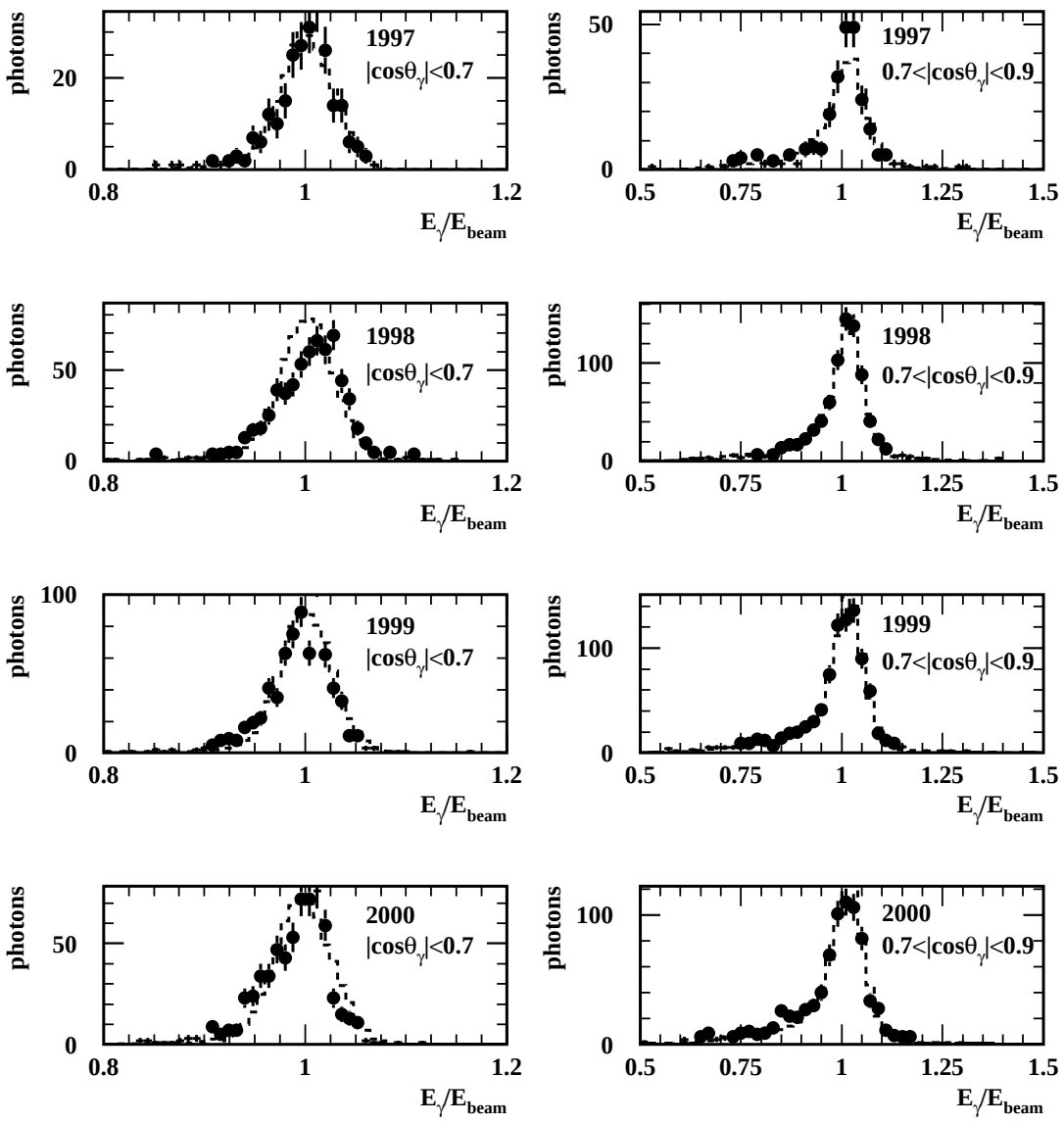

Figure 3.6: Photon energy distributions normalised to the beam energy in the barrel ($|\cos(\theta_\gamma)| < 0.7$) and end-cap ($0.7 < |\cos(\theta_\gamma)| < 0.9$) regions of the detector, in the four years of interest. The points with error bars show the OPAL data and the dashed histograms represent the fully simulated RADCOR Monte Carlo events.

	BARREL		END-CAP	
Year	C_{S}	C_{R}	C_{S}	C_{R}
1997	1.002±0.003	0.96±0.10	1.006±0.005	0.70±0.09
1998	1.003±0.001	1.15±0.06	1.001±0.003	0.96±0.07
1999	0.996±0.001	1.04±0.06	0.999±0.003	1.00±0.06
2000	0.994±0.001	1.00±0.05	0.995±0.004	1.18±0.09

Table 3.3: Correction factors C_{R} and C_{S} parametrising the difference between the energy distributions of generated and simulated two-photon events.

During the optimisation stage, the corrections

$$\begin{aligned} E_{\mathrm{R}} &= E_{\mathrm{MC}} + C_{\mathrm{R}}(E - E_{\mathrm{MC}}), \\ E_{\mathrm{S}} &= C_{\mathrm{S}} E \end{aligned}$$

were applied to the Monte Carlo samples at each centre-of-mass energy, where E is the reconstructed photon energy, E_{MC} is the generated photon energy and E_{R} and E_{S} are the resolution and scale corrected reconstructed photon energies, respectively. Comparing the reweighted Standard Model templates based on the unadjusted photon energies E with those containing the adjusted quantities E_{R} and E_{S} then gives the uncertainties in the binned and total cross-sections, $\Delta\sigma_i^E$ and $\Delta\sigma_{\mathrm{total}}^E$, in a particular binning scenario. If it was found from the Gaussian fits that $\sigma(C_{\mathrm{R,S}}) > |1 - C_{\mathrm{R,S}}|$, where $\sigma(C_{\mathrm{R,S}})$ is the error on the correction factor, then $1 \pm \sigma(C_{\mathrm{R,S}})$ was taken as the adjustment, whichever gave the greatest change in the total cross-section. The photon energies were not simply corrected by C_{R} and C_{S}, since strictly these factors apply only for beam energy photons.

The uncertainties on the Standard Model cross-sections are summarised in table 3.4. The relative signs of the errors are important as they show how the shifting and smearing of the photon energies during their reconstruction can change the distribution of events among the bins. Although the uncertainties were evaluated at each of the seven centre-of-mass energies studied, only eight independent y-parameters are assigned, four for the scale uncertainty and four for the resolution uncertainty, since the calibration of the detector was constant over each of the four years of interest.

Theoretical Uncertainty

The Standard Model expectation from a second Monte Carlo generator, KK2F [72] was used to crosscheck the results from NUNUGPV. The predictions for the total accepted cross-section at each centre-of-mass energy are in excellent agreement, as shown in the final column of the lower section of table 3.4. A comparison of binned cross-sections from the two generators was also made, in order to evaluate any possible uncertainty in the shapes of the Standard Model $M_{\rm rec}$ and $E_{\gamma 2}$ distributions, not manifest in the good agreement of the total cross-sections. These results have also been entered into table 3.4: for some bins the errors are large due to the low statistics available from KK2F, though in the bins with higher statistics (7 and 8) good agreement is again seen. Any unknown theoretical difference between the two generators was associated with a single extra free y-parameter.

A further theoretical uncertainty has been assigned by comparing the NUNUGPV prediction for the variation in the cross-section of $\mathrm{e^+e^-} \to \mathrm{Z}\gamma\gamma$ with the anomalous couplings with that reported by Belanger *et al.* [24]. Their findings are reproduced in figure 3.7 and using the same cuts on the final state photons ($E_\gamma > 5$ GeV and $20^\circ < \theta_\gamma < 160^\circ$) the results from NUNUGPV are superimposed. The parameters k_0 and $k_{\rm c}$ used by Belanger *et al.* are related to a_0 and $a_{\rm c}$ by

$$a_{0,\rm c} = 4g^2 k_{0,\rm c},$$

where $g = e/\sin\theta_W$ and the constraint that $a_{0,\rm c} = a^{\rm W}_{0,\rm c} = a^{\rm Z}_{0,\rm c}$ is imposed. Since NUNUGPV models the $\nu\overline{\nu}\gamma\gamma$ final state rather than the more general $\mathrm{Z}\gamma\gamma$ production, an additional cut of $80 < M_{\rm rec} < 120$ GeV has been applied to the NUNUGPV $M_{\rm rec}$ distribution in order to select the $\mathrm{Z}\to\ \nu\overline{\nu}\gamma\gamma$ part of the $\mathrm{e^+e} \to \nu\overline{\nu}\gamma\gamma$ signal. The NUNUGPV cross-section has also been multiplied by a factor of five to account for the other possible Z decay channels. It is found that the NUNUGPV cross-sections are up to 10% lower than the Belanger *et al.* curves, though it is estimated that approximately 6% of the NUNUGPV signal is lost through the $M_{\rm rec}$ cut. An uncertainty of 4% is therefore assigned to the binned and total cross-sections at all centre-of-mass energies.

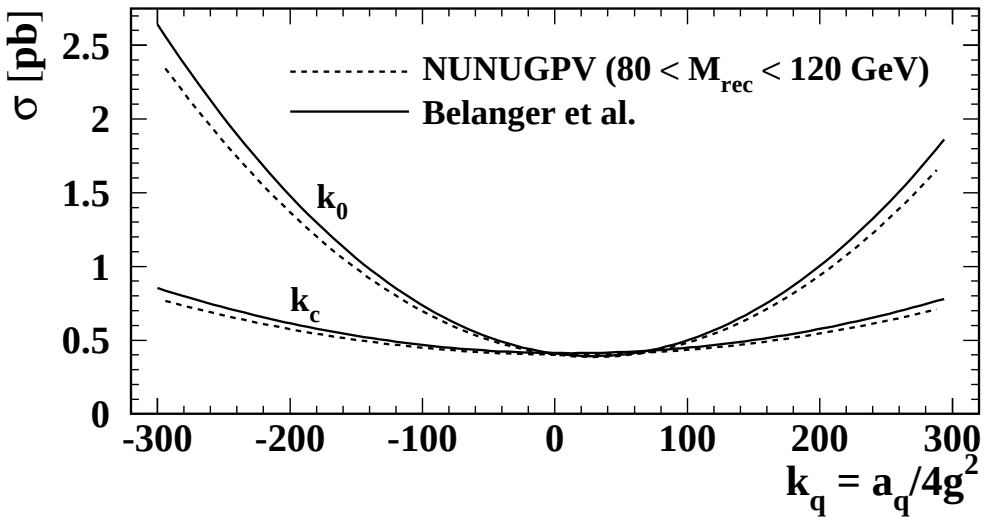

Figure 3.7: The cross-section for $e^+e^- \to Z\gamma\gamma$ as a function of the anomalous couplings at the $ZZ\gamma\gamma$ vertex, comparing the prediction of NUNUGPV with the results of Belanger *et al.* [24] at $\sqrt{s} = 200$ GeV. The energy scale $\Lambda = M_W$. Cuts on the photons of $E_\gamma > 5$ GeV and $20° < \theta_\gamma < 160°$ were used.

Normalisation Uncertainty

In addition to the 4% theoretical error from above, other sources of systematic uncertainty also taken to affect the binned and total cross-sections by the same proportion have been considered. Consequently, these leave the first (shape) term of the likelihood function unaltered and affect only the overall normalisation through equation (3.3).

The uncertainty associated with extra initial-state radiation (ISR) corrections has been assessed by comparing the Standard Model expected cross-sections obtained from NUNUGPV with ISR enabled to those obtained when the ISR photons are produced with no transverse momentum ($\pm 5\%$ on the normalisation). The luminosity error, obtained using the ROCROS software [73], is $\pm 0.3\%$. The systematic error associated with the correction for losses due to coincidental random detector hits is much less than 1% and so is neglected, as is the error associated with the expected background contribution from processes other than $e^+e^- \to \nu\overline{\nu}\gamma\gamma(\gamma)$.

Altogether, an uncertainty of 6.4% on all cross-sections is therefore assigned, taken to be independent of energy. A final additional free y-parameter is introduced, bringing the total number of free parameters in the likelihood fit to 10 for the systematics in addition to up to four anomalous couplings.

$\sqrt{s}$/GeV	Likelihood Bin Number										Total
	1	2	3	4	5	6	7	8	9	10	
ECAL Scale Uncertainty											
183	-26	-26	2.7	-4.1	-18	-27	0.59	1.3	5.9	-0.31	0.30
189	-9.3	43	-2.2	40	30	6.7	-0.91	-0.10	6.8	-1.2	0.38
192	-0.82	8.5	4.6	18	19	1.5	-0.71	-0.55	1.8	-0.23	<0.1
196	20	8.1	-1.8	14	8.2	26	-0.72	-0.29	-0.10	-0.10	0.10
200	-0.21	36	26	17	8.8	6.6	-1.0	-0.45	0.67	0.50	0.10
202	4.0	16	3.6	15	10	15	-0.61	-0.49	0.32	0.20	0.19
206	37	81	28	24	24	17	-1.5	-1.2	-0.33	-0.13	0.18
ECAL Resolution Uncertainty											
183	-1.0	0.50	16	3.6	7.2	-9.6	-0.22	0.52	2.3	-0.30	0.14
189	-0.12	0.62	1.1	10	12	3.0	-0.31	-0.11	1.4	-0.32	-0.13
192	1.3	-5.0	-6.6	-9.4	-9.7	-6.3	0.12	-0.12	-1.1	0.53	-0.24
196	2.7	-32	-2.4	-7.1	-5.3	-6.4	0.11	-0.70	-1.7	0.39	-0.42
200	<0.1	-0.44	-1.9	-8.9	-5.7	-5.9	0.22	<0.1	-1.7	0.13	-0.23
202	-1.7	1.3	-5.4	-6.9	-4.4	-6.9	0.28	0.18	-1.2	0.23	-0.10
206	0.54	-11	-6.7	-13	-11	-9.4	0.91	<0.1	-2.2	-0.62	-0.42
Theory Shape Uncertainty											
183	-82	130	120	0.12	-29	-18	2.2	-3.6	-30	-9.1	-1.8
189	-36	-34	6	8.9	4.1	42	1.9	-0.10	45	-3.5	0.91
192	180	230	-100	64	6.8	11	0.51	-5.1	-7.3	-9.9	-1.9
196	-9.9	86	-12	8.1	-13	-6.3	1.8	-1.9	11	-13	-2.2
200	14	260	-100	0.51	-1.7	51	2.9	-4.9	-17	-5.9	-1.9
202	34	11	260	-7.8	-15	-18	-3.1	-4.5	-20	-3.6	-4.4
206	-33	100	86	12	-10	69	3.1	-9.5	-13	-6.2	-3.6

Table 3.4: Percentage errors on the Standard Model accepted cross-sections in each of the 10 bins of the likelihood function, arising from the ECAL energy scale and resolution uncertainties and the uncertainty in the shapes of the $M_{\rm rec}$ and $E_{\gamma 2}$ distributions. The results at each centre-of-mass energy are shown. The errors on the total accepted cross-sections are given in the final column. Large errors are found in some bins for the theoretical uncertainty due to the low population of these bins by the KK2F statistics.

Chapter 4

Results and Conclusion

This chapter presents the constraints found on the anomalous couplings at the WW$\gamma\gamma$ and ZZ$\gamma\gamma$ vertices from the analysis of the OPAL $\nu\overline{\nu}\gamma\gamma$ events. These limits are combined with those from OPAL analyses of other processes also sensitive to the same anomalous couplings.

4.1 Monte Carlo Studies

Before comparing the Monte Carlo expectations with the data, bias tests were performed to ensure that the likelihood fit procedure behaved correctly. The limits on the anomalous couplings that may be expected from the OPAL data were also found from an ensemble test.

4.1.1 Bias Tests

The bias tests used Monte Carlo samples generated with different anomalous couplings as inputs to the likelihood fit. The tests were intended to verify that for a sample generated with an anomalous coupling $a = a_{\rm gen}$ a minimum in $-\ln(a)$ at $a_{\rm fit} = a_{\rm gen}$ is returned by the fit. In each case, the sample used as the input was

excluded from the fifteen samples that were reweighted to obtain $\sigma_i^E(a_0^{\rm W}, a_{\rm c}^{\rm W}, a_0^{\rm Z}, a_{\rm c}^{\rm Z})$ and $\sigma_{\rm total}^E(a_0^{\rm W}, a_{\rm c}^{\rm W}, a_0^{\rm Z}, a_{\rm c}^{\rm Z})$. For each anomalous coupling parameter studied the other three were kept fixed at zero and the systematic uncertainties were neglected.

The results are shown in figure 4.1. Due to the quadratic dependence of the cross-section on each of the coupling parameters, a second minimum is always found at $a_{\rm fit} = -a_{\rm gen}$ (not plotted.) However, in all but one of the eight tests with non-zero anomalous couplings, this false minimum was always at a higher value of $-\ln L(a)$ than the true minimum. It is concluded that the likelihood function used can successfully constrain the anomalous coupling parameters from the OPAL data.

4.1.2 Ensemble Test

In this test, 5 000 sub-samples were selected from each Standard Model Monte Carlo sample, such that the number of events in each sub-sample had a Poisson distribution with a mean equal to the number expected in the data at that centre-of-mass energy. For each coupling a, the distribution of the difference, $\Delta \ln L(a)$, between the minimum value of the $-\ln$-likelihood returned by the fit and the value of the $-\ln$-likelihood with $a = 0$ was obtained. The other three anomalous coupling parameters were fixed at zero as were the parameters governing the systematic uncertainties. The fraction of the 5 000 samples with $\Delta \ln L(a) > 1.92$ was 2.7%, 2.6%, 2.0% and 1.8% for the couplings $a_0^{\rm W}$, $a_{\rm c}^{\rm W}$, $a_0^{\rm Z}$ and $a_{\rm c}^{\rm Z}$ respectively. A $\Delta \ln L(a)$ interval of 1.92 therefore represents a confidence level of slightly more than the Gaussian 95%. That the actual 1.92 likelihood interval contains about half the number of sub-samples expected from Gaussian statistics reflects the fact that in cases where the number of events fluctuates below the Standard Model expectation the likelihood fit is constrained to return $a_{\rm fit} \approx 0$.

The expected 95% confidence level limits on each parameter were obtained by

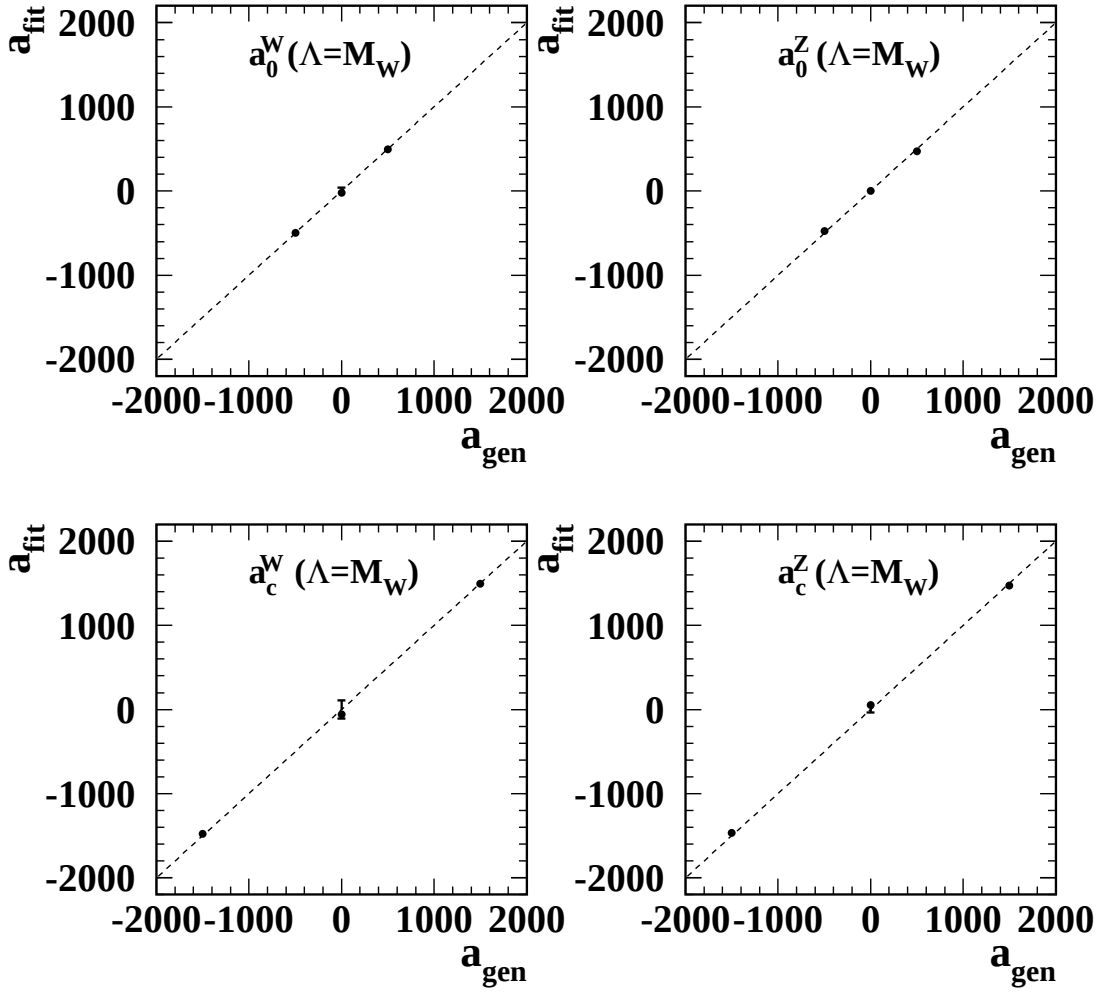

Figure 4.1: Bias test results. For each of the four couplings, the value of the parameter extracted from the fit, $a_{\rm fit}$, is plotted against the coupling value with which the input sample was generated, $a_{\rm gen}$. The 95% confidence level error bars are drawn.

averaging the 5 000 upper and lower limits from the ensemble test:

$$\begin{aligned}
-0.040\ \mathrm{GeV}^{-2} < \quad a_0^{\mathrm{W}}/\Lambda^2 \quad &< 0.046\ \mathrm{GeV}^{-2}, \\
-0.095\ \mathrm{GeV}^{-2} < \quad a_{\mathrm{c}}^{\mathrm{W}}/\Lambda^2 \quad &< 0.095\ \mathrm{GeV}^{-2}, \\
-0.014\ \mathrm{GeV}^{-2} < \quad a_0^{\mathrm{Z}}/\Lambda^2 \quad &< 0.025\ \mathrm{GeV}^{-2}, \\
-0.034\ \mathrm{GeV}^{-2} < \quad a_{\mathrm{c}}^{\mathrm{Z}}/\Lambda^2 \quad &< 0.033\ \mathrm{GeV}^{-2}.
\end{aligned}$$

Assuming that the Standard Model describes the data, these are the limits reflecting the statistical tolerance of the analysis which may be expected on the anomalous coupling parameters.

4.2 Events Selected from OPAL Data

Within the 1997 to 2000 OPAL data set, the numbers of events passing the full acceptance cuts at each centre-of-mass energy are shown in table 4.1. Good agreement is seen with the NUNUGPV Standard Model expectations. The total number of observed and expected events falling into each of the ten bins of the likelihood function is given in table 4.2.

The distributions of M_{rec} and $E_{\gamma 2}$ for the data events compared to the Standard Model expectations are shown in figure 4.2. In both cases, the Standard Model Monte Carlo describes the data well.

4.3 Limits on AQGCs from $\mathrm{e^+e^-} \to \nu\overline{\nu}\gamma\gamma$

Single parameter fits have been performed by minimising the $-\ln$-likelihood as a function of the AQGC parameter of interest, together with the parameters controlling the systematic errors. The resulting one-dimensional likelihood curves are presented in figure 4.3. It can be seen that the systematic uncertainties have a very small effect on the curves, which are dominated by the data statistics.

$\sqrt{s}$/GeV	$\int \mathcal{L}\ \mathrm{d}t/\mathrm{pb}^{-1}$	NUNUGPV SM	Data
183	54	2.5	0
189	175	7.9	10
192	29	1.3	1
196	72	3.1	0
200	74	3.0	3
202	37	1.5	1
206	211	8.3	5
Total	652	27.6	20

Table 4.1: The number of accepted $\nu\overline{\nu}\gamma\gamma$ events in Standard Model Monte Carlo and OPAL data by centre-of-mass energy.

Bin Number	M_{rec}/GeV	$E_{\gamma 2}$/GeV	Observed	Expected
1	< 60	10 - 25	0	0.1
2	< 60	25 - 45	0	$<$0.1
3	< 60	$>$45	0	$<$0.1
4	60 - 80	10 - 25	1	0.5
5	60 - 80	25 - 45	2	0.4
6	60 - 80	$>$45	0	0.1
7	80 - 120	10 - 25	5	11.7
8	80 - 120	25 - 45	6	8.3
9	80 - 120	$>$45	1	0.8
10	> 120	–	5	5.7
Total	–	> 10	20	27.6

Table 4.2: The total number of accepted events in Monte Carlo and data in each of the ten bins of the likelihood function.

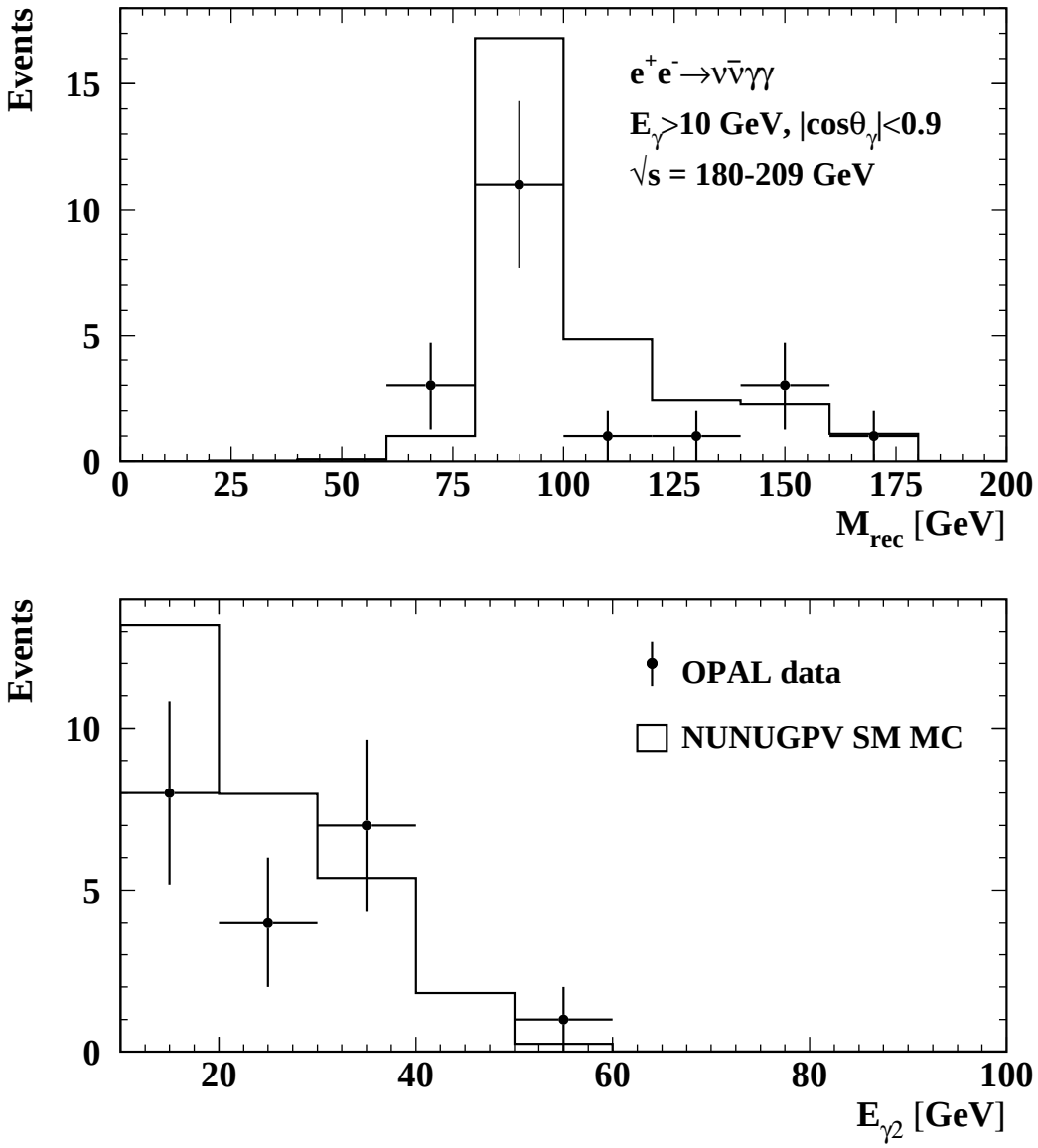

Figure 4.2: Recoil mass and second photon energy distributions for the accepted $\nu\overline{\nu}\gamma\gamma$ events in OPAL data and Monte Carlo.

The Gaussian 95% confidence level intervals consistent with the data on the anomalous couplings varied individually are:

$$
\begin{aligned}
-0.040\ \mathrm{GeV}^{-2} < \ & a_0^{\mathrm{W}}/\Lambda^2 \ & < 0.037\ \mathrm{GeV}^{-2}, \\
-0.114\ \mathrm{GeV}^{-2} < \ & a_{\mathrm{c}}^{\mathrm{W}}/\Lambda^2 \ & < 0.103\ \mathrm{GeV}^{-2}. \\
-0.009\ \mathrm{GeV}^{-2} < \ & a_0^{\mathrm{Z}}/\Lambda^2 \ & < 0.026\ \mathrm{GeV}^{-2}, \\
-0.034\ \mathrm{GeV}^{-2} < \ & a_{\mathrm{c}}^{\mathrm{Z}}/\Lambda^2 \ & < 0.039\ \mathrm{GeV}^{-2}.
\end{aligned}
$$

These are all compatible with zero and are in good agreement with the expected Standard Model limits from the ensemble test of section 4.1.2. They are comparable to the AQGC limits found by ALEPH in this channel [32]. As expected, since the total cross-section for $\mathrm{e^+e^-} \to \nu\overline{\nu}\gamma\gamma$ depends more strongly on the possible anomalous $\mathrm{ZZ}\gamma\gamma$ contribution than on possible $\mathrm{WW}\gamma\gamma$ contribution (figure 3.1), the a^{Z} coupling parameters are more tightly constrained than their a^{W} counterparts.

The results of a fit allowing two AQGC parameters to vary simultaneously are shown in figure 4.4, again with the two parameters not plotted fixed at zero. The 95% confidence level contour is drawn at a $-\ln$-likelihood interval of +3.0 and all systematic effects are included. The relatively tighter constraints on the Z couplings compared to the W couplings are evident in these plots. Furthermore, since the anomalous $\mathrm{ZZ}\gamma\gamma$ and $\mathrm{WW}\gamma\gamma$ couplings affect different regions of the invariant mass and second photon energy distributions, the limits on the a_0^{Z} and a_0^{W} are uncorrelated. The same is true for the limits on $a_{\mathrm{c}}^{\mathrm{Z}}$ and $a_{\mathrm{c}}^{\mathrm{W}}$.

Two-dimensional projections of the full four-dimensional fits are superimposed in figure 4.4. In these plots, at each point in the plane defined by the two AQGC parameters of interest, the likelihood is also minimised with respect to the other two AQGC parameters. Again, due to the choice of binning of the M_{rec} and $E_{\gamma 2}$ distributions, in the cases where the two AQGC parameters plotted are associated with the same vertex, plots (b) and (d), allowing the other two parameters to float has only a small effect on the width of the likelihood function. The minimum in these plots represents the overall most likely values of the four AQGC parameters favoured by the $\mathrm{e^+e^-} \to \nu\overline{\nu}\gamma\gamma$ data. The results are in excellent agreement with the Standard Model: no evidence for new physics is found.

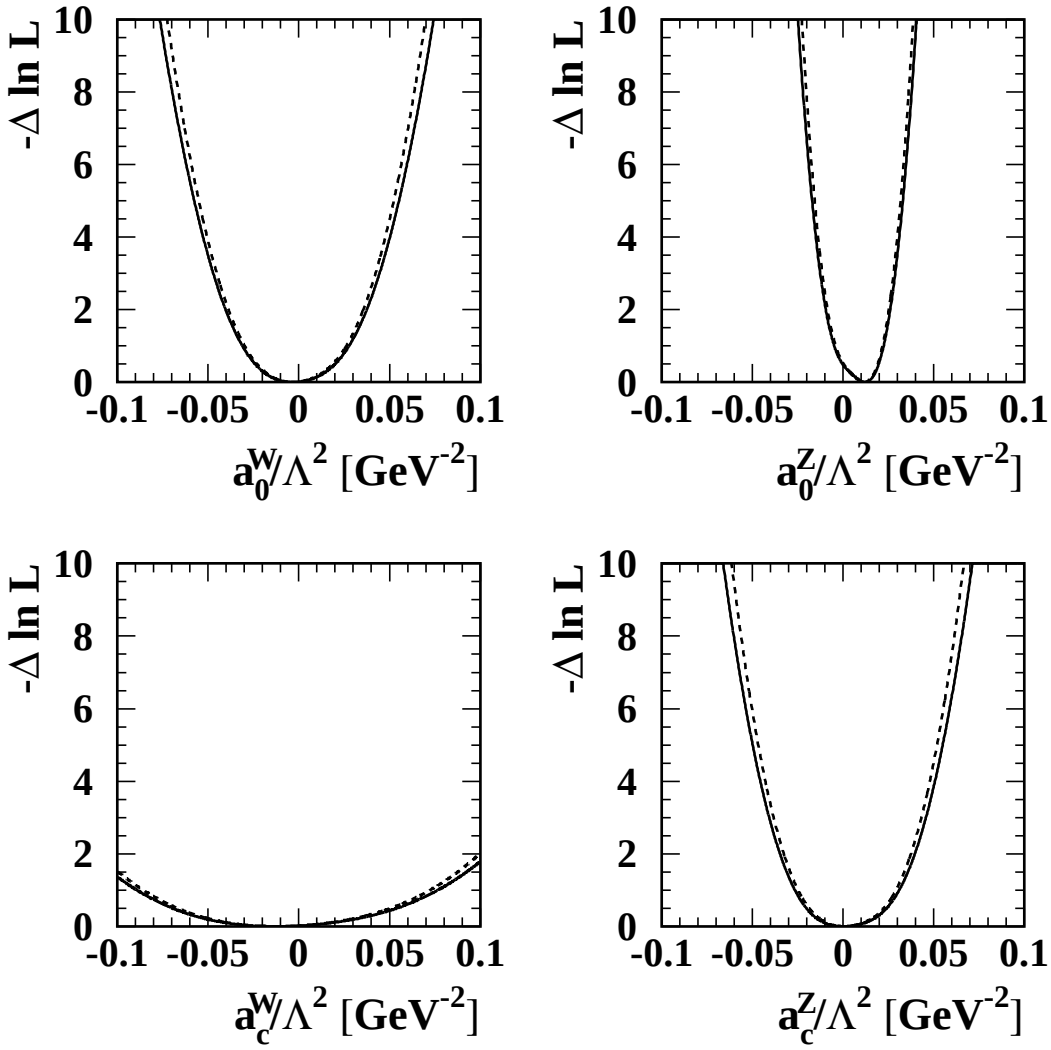

Figure 4.3: The one-dimensional likelihood curves for each of the anomalous coupling parameters from $e^+e^- \to \nu\overline{\nu}\gamma\gamma$ with (solid line) and without (dashed line) the systematic uncertainties. The parameters not plotted are fixed at zero.

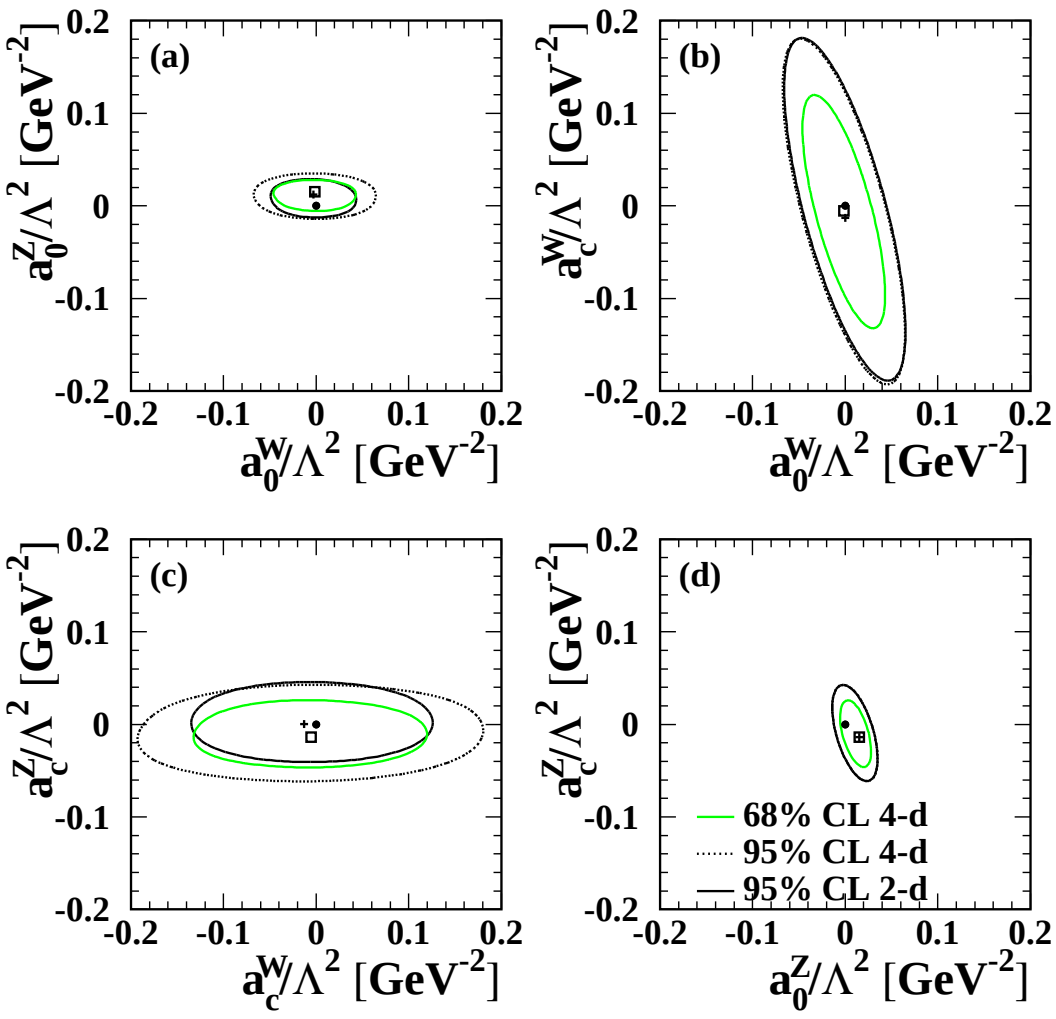

Figure 4.4: Confidence level likelihood contours on the anomalous coupling parameters from $e^+e^- \to \nu\overline{\nu}\gamma\gamma$. Systematic uncertainties are included. The solid black lines are the 95% confidence level contours obtained with the two anomalous parameters not plotted set to zero. The minimum in these fits is indicated with a cross. The grey lines and dotted black lines are the two-dimensional projections of the 68% and 95% confidence level contours from fits to all four parameters. In (b) and (d) these correspond closely to the two-parameter fits. The squares show the overall most likely values of the four AQGC parameters and the circles show the Standard Model expectations for comparison.

4.4 Combined Limits on AQGCs

Limits on the parameters a_0^W and a_c^W have been found in a recent OPAL study of the $e^+e^- \to W^+W^-\gamma$ process [26]. In addition, limits have been placed on a_0^Z and a_c^Z from the $q\bar{q}\gamma\gamma$ final state [74]. The results from these channels have been combined with those from the $\nu\bar{\nu}\gamma\gamma$ final state through the addition of the appropriate likelihood curves. The actual combinations have been performed by Mark Thomson in the preparation of [74].

Combined limits on the WW$\gamma\gamma$ couplings

The one-dimensional likelihood curves for the a_0^W and a_c^W coupling parameters obtained from the $\nu\bar{\nu}\gamma\gamma$ and $W^+W^-\gamma$ channels are superimposed in figure 4.5. There are no significant correlated error sources between the two channels so the combination is made by summing the two curves. Allowing both WW$\gamma\gamma$ parameters to vary simultaneously gives the combined likelihood contour of figure 4.6. The AQGC parameters a_0^Z and a_c^Z are fixed at zero.

The inclusion of the results from the $\nu\bar{\nu}\gamma\gamma$ final state provides only a small additional constraint on the anomalous WW$\gamma\gamma$ couplings found from the $W^+W^-\gamma$ analysis. Double-minima are seen in the summed likelihood curves, arising from the double-minima seen in the likelihood curves from the $W^+W^-\gamma$ channel. The combined 95% confidence level limits on the coupling parameters are:

$$\begin{aligned} -0.020\ \text{GeV}^{-2} < \ & a_0^W/\Lambda^2 \ < 0.020\ \text{GeV}^{-2}, \\ -0.052\ \text{GeV}^{-2} < \ & a_c^W/\Lambda^2 \ < 0.037\ \text{GeV}^{-2}. \end{aligned}$$

No deviations from the Standard Model are seen.

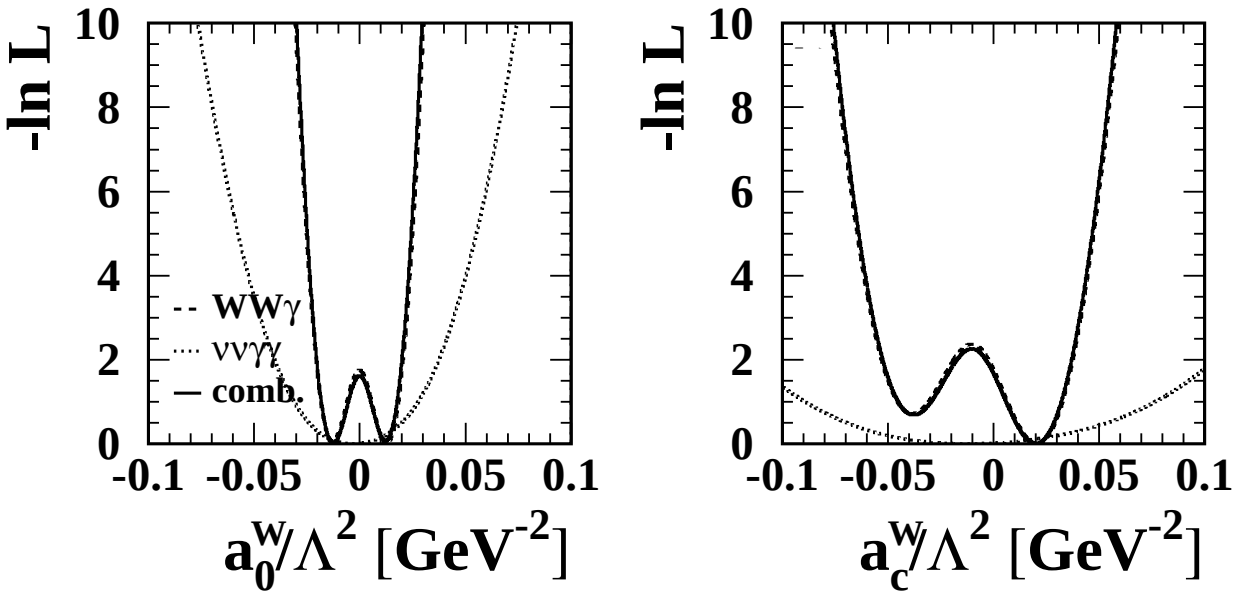

Figure 4.5: Combined one-dimensional likelihood curves for a_0^{W} and $a_{\mathrm{c}}^{\mathrm{W}}$ from the $\nu\overline{\nu}\gamma\gamma$ and $\mathrm{W^+W^-}\gamma$ channels.

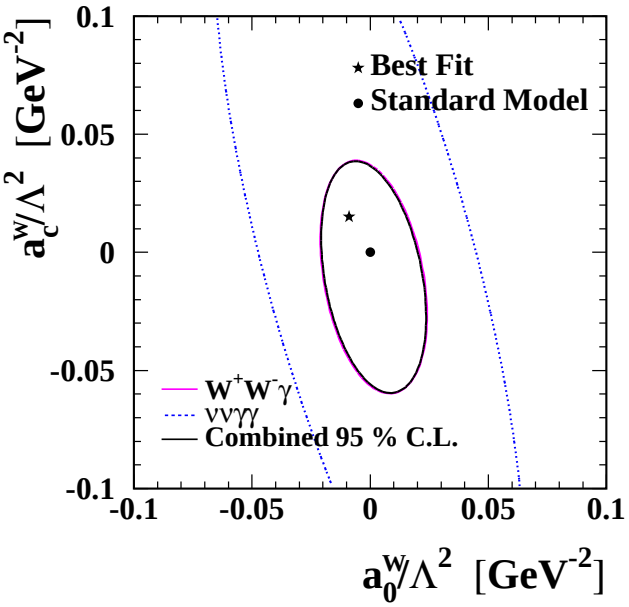

Figure 4.6: Combined 95% confidence level contour for $(a_0^{\mathrm{W}}, a_{\mathrm{c}}^{\mathrm{W}})$ from the $\nu\overline{\nu}\gamma\gamma$ (dotted line) and $\mathrm{W^+W^-}\gamma$ (grey line) channels. The limits from the $\mathrm{W^+W^-}\gamma$ channel dominate to such an extent that they coincide almost exactly with the combined limits (black line). The minimum of the $-\ln L$ surface is indicated with a star.

Combined limits on the ZZ$\gamma\gamma$ couplings

The summed one-dimensional likelihood curves for the parameters a_0^Z and a_c^Z from the $q\overline{q}\gamma\gamma$ and $\nu\overline{\nu}\gamma\gamma$ final states are shown in figure 4.7, again assuming independent systematics for the two channels. Similar sensitivity to these AQGCs is provided by both channels. Allowing both ZZ$\gamma\gamma$ parameters to vary simultaneously gives the likelihood contours of figure 4.8. The AQGC parameters a_0^W and a_c^W are fixed at zero.

The corresponding combined 95% confidence level limits on the possible anomalous contributions to the ZZ$\gamma\gamma$ vertex are

$$\begin{aligned} -0.007 \text{ GeV}^{-2} < \quad a_0^Z/\Lambda^2 \quad < 0.023 \text{ GeV}^{-2}, \\ -0.029 \text{ GeV}^{-2} < \quad a_c^Z/\Lambda^2 \quad < 0.029 \text{ GeV}^{-2}. \end{aligned}$$

Again, no deviations from the Standard Model are observed.

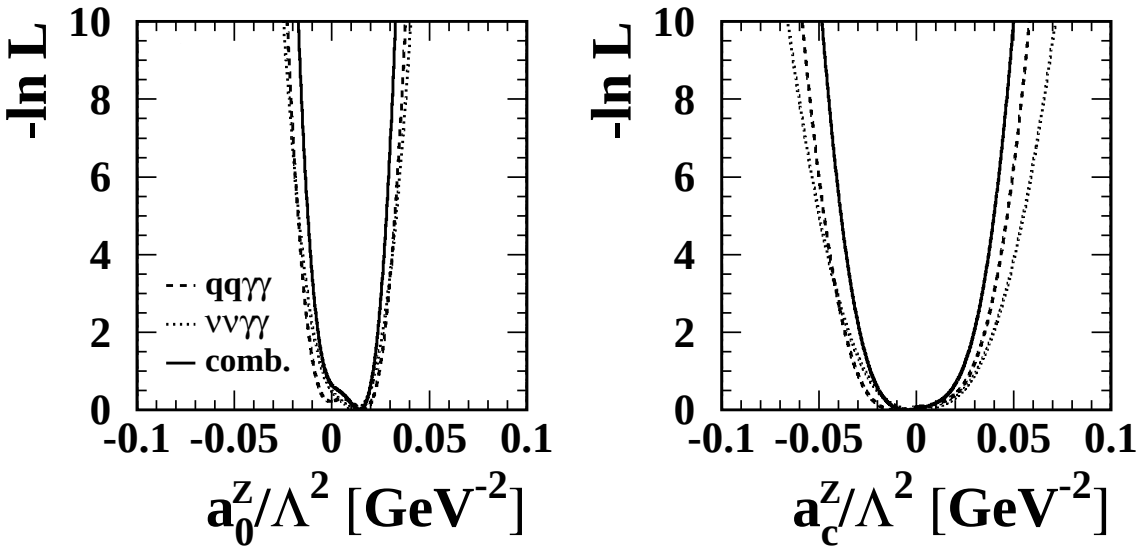

Figure 4.7: Combined one-dimensional likelihood curves for a_0^Z and a_c^Z from the $\nu\overline{\nu}\gamma\gamma$ and $q\overline{q}\gamma\gamma$ channels.

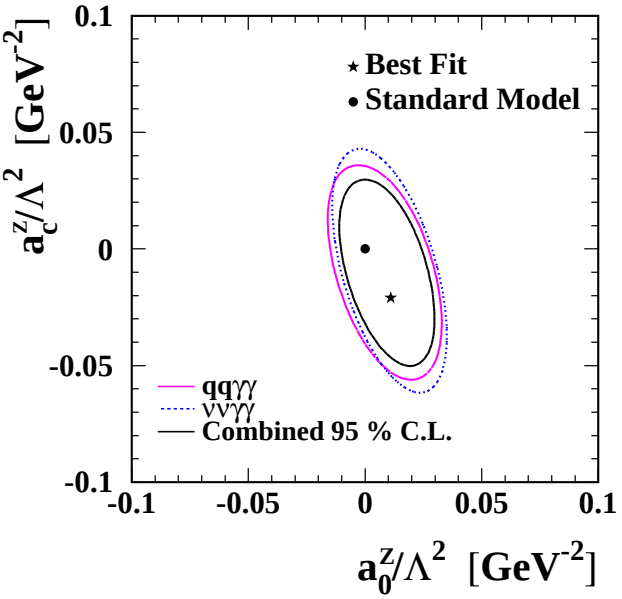

Figure 4.8: Combined 95% confidence level contour for (a_0^Z, a_c^Z) from the $\nu\overline{\nu}\gamma\gamma$ (dotted line) and $q\overline{q}\gamma\gamma$ (grey line) channels. The minimum of the $-\ln L$ surface is indicated with a star.

Combined Limits on a_0 and a_c

Since OPAL and other LEP experiments have reported limits on the WW$\gamma\gamma$ and ZZ$\gamma\gamma$ AQGCs in terms of the parameters a_0 and a_c [29, 31, 30, 27], limits are also reported here imposing the extra condition that $a_0^W = a_0^Z = a_0$ and $a_c^W = a_c^Z = a_c$. This constraint allows the likelihood curves from the $\nu\overline{\nu}\gamma\gamma$, $q\overline{q}\gamma\gamma$ and $W^+W^-\gamma$ channels to be combined. The results for the one- and two- dimensional fits are shown in figures 4.9 and 4.10.

The 95% confidence level limits on the parameters a_0 and a_c are

$$\begin{aligned} +0.002\ \text{GeV}^{-2} < \quad a_0/\Lambda^2 \quad < 0.019\ \text{GeV}^{-2}, \\ -0.022\ \text{GeV}^{-2} < \quad a_c/\Lambda^2 \quad < 0.029\ \text{GeV}^{-2}. \end{aligned}$$

Due to the influence of the double-minima, the Standard Model is disfavoured by $\Delta \ln L = 2.0$ in the a_0 fit. In the Gaussian approximation this corresponds to only 2.0 standard deviations, however. Thus, the results from this overall combination of channels are consistent with the Standard Model.

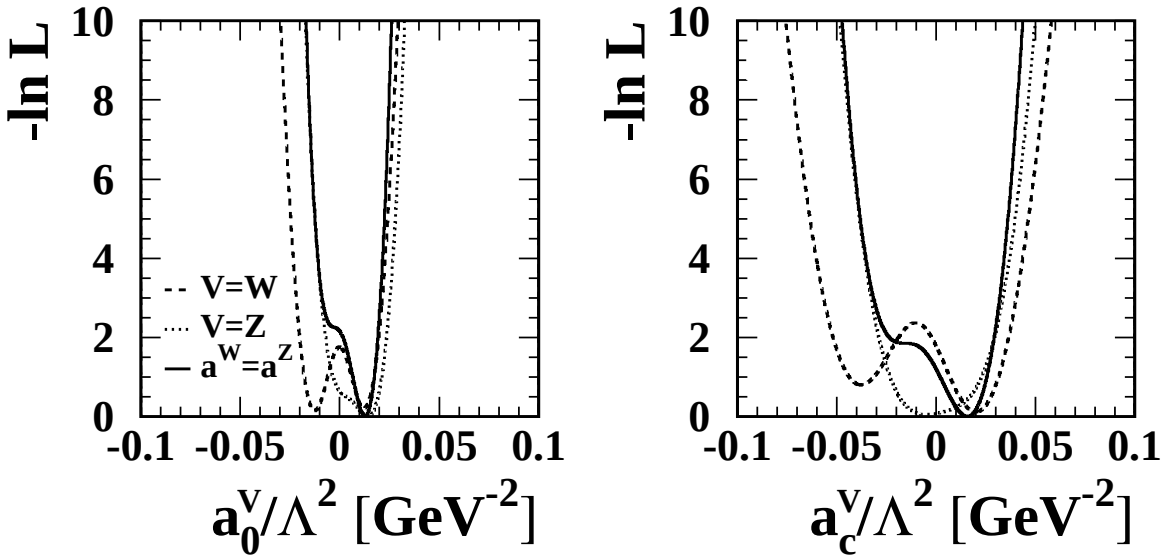

Figure 4.9: Combined one-dimensional likelihood curves for a_0 and a_c. The dashed lines show the combined constraints on the a^W parameters from $\nu\overline{\nu}\gamma\gamma$ and $W^+W^-\gamma$, the dotted lines on the a^Z parameters from $\nu\overline{\nu}\gamma\gamma$ and $q\overline{q}\gamma\gamma$ and the solid lines the overall combined limits assuming $a^W = a^Z$.

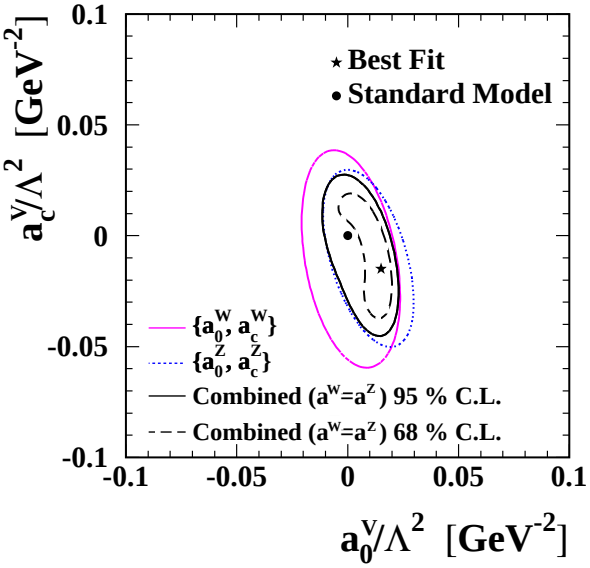

Figure 4.10: Confidence level contours for (a_0^V, a_c^V). The grey line shows the combined (a_0^W, a_c^W) 95% confidence level contour from $\nu\overline{\nu}\gamma\gamma$ and $W^+W^-\gamma$. The dotted line shows the combined (a_0^Z, a_c^Z) 95% confidence level contour from $\nu\overline{\nu}\gamma\gamma$ and $q\overline{q}\gamma\gamma$. The dashed and solid lines then show the 68% and 95% confidence regions, respectively, in (a_0, a_c) assuming $a_0^W = a_0^Z$ and $a_c^W = a_c^Z$.

4.5 Summary

It has been shown in chapter 1 how the $\nu\overline{\nu}\gamma\gamma$ final state is sensitive to possible AQGCs of the form WW$\gamma\gamma$ and ZZ$\gamma\gamma$. The acoplanar photon pairs arising in this final state have been selected from OPAL data at centre-of-mass energies 183-209 GeV, using the event selection criteria outlined in chapter 2. Subsequently, the maximum likelihood function constructed in chapter 3 has been used to constrain the anomalous coupling parameters a_0^{W}, $a_{\mathrm{c}}^{\mathrm{W}}$, a_0^{Z} and $a_{\mathrm{c}}^{\mathrm{Z}}$. Both the selection of the acoplanar photon pair events and the binning of the likelihood function were optimised in order to attain maximal sensitivity to the possible AQGCs. The systematic uncertainties, although small, were considered in this optimisation.

The resulting 95% confidence limits on the AQGC parameters from the $\nu\overline{\nu}\gamma\gamma$ final state are

$$\begin{aligned}
-0.040\ \mathrm{GeV}^{-2} < \ & a_0^{\mathrm{W}}/\Lambda^2 \ < 0.037\ \mathrm{GeV}^{-2}, \\
-0.114\ \mathrm{GeV}^{-2} < \ & a_{\mathrm{c}}^{\mathrm{W}}/\Lambda^2 \ < 0.103\ \mathrm{GeV}^{-2}, \\
-0.009\ \mathrm{GeV}^{-2} < \ & a_0^{\mathrm{Z}}/\Lambda^2 \ < 0.026\ \mathrm{GeV}^{-2}, \\
-0.034\ \mathrm{GeV}^{-2} < \ & a_{\mathrm{c}}^{\mathrm{Z}}/\Lambda^2 \ < 0.039\ \mathrm{GeV}^{-2}.
\end{aligned}$$

where Λ is the energy scale of the new physics. Combining these results with those from the q$\overline{\mathrm{q}}\gamma\gamma$ and $\mathrm{W}^+\mathrm{W}^-\gamma$ final states at OPAL, these limits are tightened to

$$\begin{aligned}
-0.020\ \mathrm{GeV}^{-2} < \ & a_0^{\mathrm{W}}/\Lambda^2 \ < 0.020\ \mathrm{GeV}^{-2}, \\
-0.052\ \mathrm{GeV}^{-2} < \ & a_{\mathrm{c}}^{\mathrm{W}}/\Lambda^2 \ < 0.037\ \mathrm{GeV}^{-2}, \\
-0.007\ \mathrm{GeV}^{-2} < \ & a_0^{\mathrm{Z}}/\Lambda^2 \ < 0.023\ \mathrm{GeV}^{-2}, \\
-0.029\ \mathrm{GeV}^{-2} < \ & a_{\mathrm{c}}^{\mathrm{Z}}/\Lambda^2 \ < 0.029\ \mathrm{GeV}^{-2}.
\end{aligned}$$

Limits obtained when allowing two parameters to vary have also been reported. All results are consistent with the current Standard Model expectations.

Chapter 5

The ATLAS Semiconductor Tracker Barrel System Test

ATLAS (A Toroidal LHC ApparatuS) is a multi-purpose detector being constructed at CERN to study the physics in the TeV mass range that will be accessible by the Large Hadron Collider (LHC). This chapter gives an introduction to the LHC, ATLAS and the ATLAS Inner Detector, of which the Semiconductor Tracker (SCT) forms one component. This is followed by a description of the physical principles and operation of the silicon micro-strip detectors that make up the SCT. The results of tests performed at the SCT barrel system test are then presented. The final section describes and demonstrates techniques for the measurement of common-mode noise in binary read-out systems.

5.1 Experimental Framework

5.1.1 Introduction to the LHC

The LHC is being constructed in the 27 km circumference tunnel that previously housed the LEP synchrotron. Consisting of two beam pipes, the new accelerator will

collide protons at $7 + 7$ TeV, though due to the composite nature of these particles only a small fraction of the total 14 TeV centre-of-mass energy will be available for hard physics processes. The expected luminosity is 10^{33} cm^{-2}s^{-1} initially, rising to 10^{34} cm^{-2}s^{-1} in the high luminosity phase after three years. Like LEP, there will be four interaction points around the ring where the new detectors ATLAS [75], CMS, ALICE and LHC-B are being constructed.

5.1.2 The ATLAS Experiment: An Overview

The 44 m long and 22 m high ATLAS detector (figure 5.1) is intended to realise the main physics goals of the LHC project: searches for the Higgs boson and for supersymmetric particles. Extending outwards from the beam pipe, ATLAS comprises an Inner Detector (ID), a solenoid magnet, a liquid argon (LAr) electromagnetic calorimeter, a hadronic calorimeter and a muon spectrometer with an air-core toroid system. The ID and SCT will be outlined in more detail below: for a description of the other components refer to [75].

The LHC bunch crossing rate will be 40 MHz, with a projected total interaction rate of 1 GHz. Each detector subsystem has a pipeline memory to hold the events pending a level-1 trigger [76], which will reduce the rate to a maximum of 100 kHz. Following the level-2 trigger, the filter and the event builder, events will be stored at 100 Hz, amounting to approximately 10^9 Mb of data per year of running.

5.1.3 The Inner Detector: Introducing the SCT

The ID [77] will occupy the most central region of ATLAS and is designed to provide precision tracking of charged particles from the interaction region to the electromagnetic calorimeter. The complete sub-detector (figure 5.2) is 7 m long and extends to a radius of 1.15 m. Its location inside the solenoid allows the momentum and charge sign of charged particles to be measured from the curvature of their paths in the 2 T magnetic field.

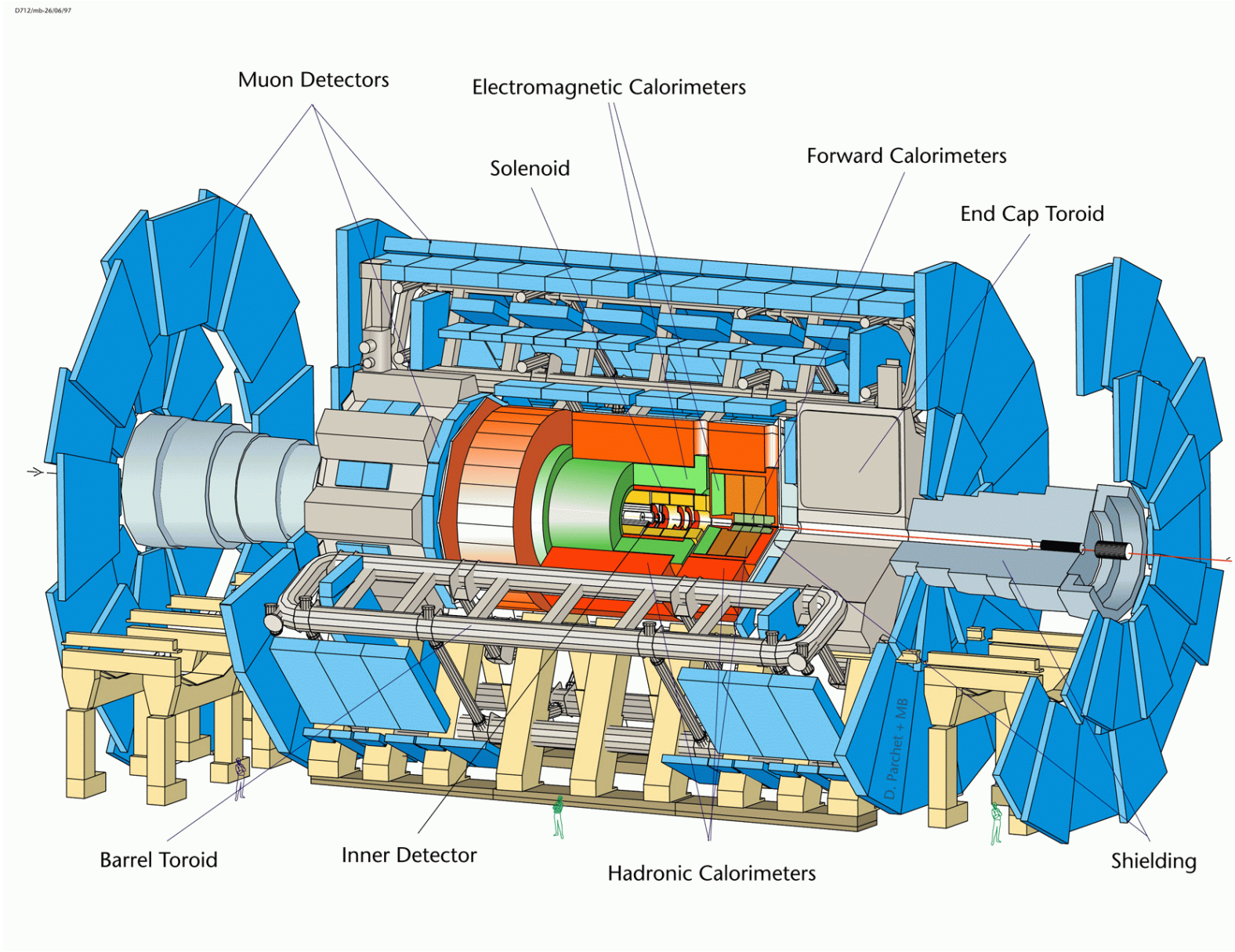

Figure 5.1: The complete ATLAS detector.

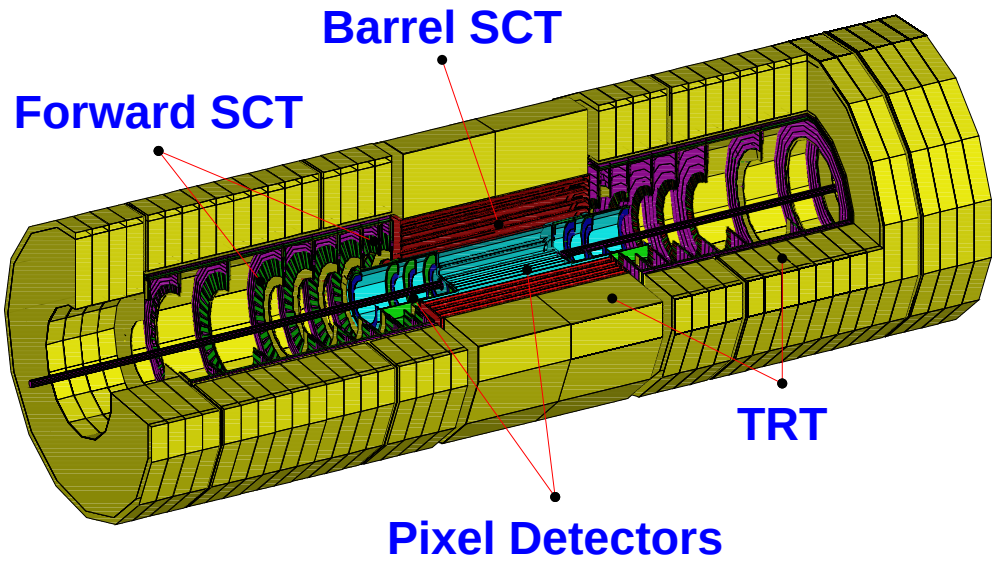

Figure 5.2: The ATLAS Inner Detector.

The SCT [77, 78, 79] is intended to contribute to the momentum, vertex and impact parameter measurements of the ID by finding four precision points per particle track. The barrel component will cover the 30 to 55 cm intermediate radial range of the ID with four nested barrels 1.5 m in length and is capped at each end by two end-caps, each of 9 disks. The four SCT barrel layers are to be tiled with a total of 2 112 identical modules [79, 80] in 32, 40, 46 and 56 rows of 12. These modules are described in detail in the next section.

In addition to the SCT, the ID comprises also a PIXEL detector and a Transition Radiation Tracker (TRT). Compared to the silicon strips of the SCT, the PIXEL technology to be used in the inner-most part of the ID is more expensive and requires more material per track. However, the PIXEL sub-system is necessary to provide the high granularity required for track reconstruction and secondary vertex finding in the high track density p-on-p environment. The outer Transition Radiation Tracker (TRT) will measure a further 36 points per track, giving overall reliable pattern recognition for the track finding algorithms.

5.2 The ATLAS Silicon Micro-Strip Detectors

The SCT employs silicon micro-strip technology which has been in use for over 10 years, though the 61 m^2 area of the SCT is an order of magnitude larger than any such previous generation detector. A brief introduction to the principles of operation of silicon detectors is given in the first part of this section: a more comprehensive review can be found in [81]. The following parts describe the SCT barrel modules and their noise performance in more detail.

5.2.1 Physics of Silicon Detectors

The electron energy levels of pure crystalline silicon are grouped into bands. At absolute zero, all atoms retain their four valence shell electrons and the valence band energy levels are fully occupied. These electrons can be easily thermally excited into the conduction band, however, the bottom of which lies at just 1.1 eV above the top of the valence band. Since the electrons promoted to the conduction band, and the resulting hole states which are created in the valence band, are mobile, silicon is a semiconductor at room temperature.

Silicon may be doped by introducing either a small group V or group III type impurity. The first of these forms of doping produces n-type silicon, in which the donor atoms of the group V element contribute additional electrons to the conduction band. In the second case, the acceptor atoms easily attach electrons from the silicon, and consequently the resulting p-type material has an excess of holes in the valence band.

The detectors of the SCT modules consist of an n-type silicon bulk. The micro-strips are formed by implanting strips of p^+-type material, in which the doping with an acceptor impurity is heavier than the doping of the bulk with the donor atoms. At the resulting p^+-n junction, the electrons in the conduction band of the n-type material diffuse to fill the holes in the valence band of the p-type material, creating a potential difference across the junction and a region almost devoid of free charge

carriers. This depletion zone extends further into the n-type material due to its weaker relative doping. By applying a reverse bias voltage, the intrinsic potential difference of the diode is enhanced and the depletion region can be made to extend throughout the n-type bulk.

Charged particles traversing the bulk material deposit energy according to the Bethe-Bloch equation [82]. In the 285 μm thick silicon of the SCT detectors, the most probable amount of energy deposited by one minimum ionising particle is 85 keV. Since approximately 3.6 eV is required to create one electron-hole pair, this corresponds to the production of about 24000 such pairs. The liberated holes are swept by the field to the p^+-type implants closest to where the incident charged particle passed through the bulk. The resulting signals induced in the aluminium micro-strips, which are bonded on a layer of insulator above the p^+ implants, can then be read out.

5.2.2 The Barrel SCT Modules

A single module (figure 5.3) comprises four silicon detectors, each of which has an active area of approximately 6 mm by 6 mm covered by 768 channels of 80 μm pitch. These detectors are joined in pairs end to end to create two 12 cm long sensors which are then glued back to back with a 40 mrad stereo angle, either side of a thermally conductive baseboard. The read-out of charge from the micro-strips is performed in groups of 128 by twelve ABCD front-end ASICs [83]. These are mounted on a hybrid card which wraps around the middle of the four detectors, as visible in figure 5.3. The charge collected in one channel is amplified by the gain ($\approx$ 50mV/fC) and discriminated against some threshold (1 fC or $\approx$ 50 mV), with the resulting binary output being stored in a pipeline memory.

The spatial resolution perpendicular to the strips of a single detector is approximately 23 μm. Within a double-sided module the actual r-ϕ resolution is improved to approximately 20 μm. Owing to the stereo offset between the two detector planes, a resolution in the z-direction of around 1000 μm is achieved.

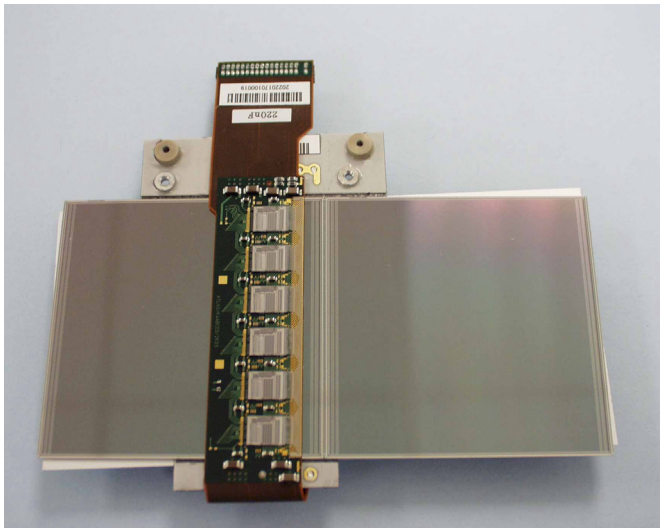

Figure 5.3: Photograph of a single SCT barrel module. The six chips on the upper side of the hybrid card are visible.

5.2.3 Noise in Binary Read-Out Systems

In a binary read-out system the level of noise is a crucial parameter since it determines how high the threshold must be set in order to limit the rate of false hits which arise due to the noise, which in turn influences the detection efficiency. If the threshold is set too low, the number of noise hits is increased, which leads to a reduced tracking performance. Moreover, the total amount of data which has to be read out is also increased. However, the threshold cannot be made arbitrarily high without a loss of efficiency.

The random noise in any detector channel can be assumed to have an independent Gaussian distribution given by

$$P(x) = \frac{1}{\sqrt{2\pi Q_{\mathrm{rnd}}^2}} \exp\left(-\frac{x^2}{2Q_{\mathrm{rnd}}^2}\right),$$

where the size of the noise in units of charge, x, has an RMS value given by the width Q_{rnd}. This RMS value is conventionally taken as a measure of the size of the noise present. The observed occupancy, O, arising due to the noise, above some

threshold, $Q_{\rm thr}$, is then given by

$$O(Q_{\rm thr}) = \int_{Q_{\rm thr}}^{\infty} P(x)dx,$$

which evaluates to the complementary error function, or "S-curve":

$$O(Q_{\rm thr}) = \frac{1}{2}{\rm erfc}\left(\frac{Q_{\rm thr}}{\sqrt{2Q_{\rm rnd}^2}}\right).$$

In the SCT, the high occupancy due to real hits demands that the noise hit rate be less than 5×10^{-4} [77]. Under the Gaussian assumption, this requires that $Q_{\rm thr}$ be set at 3.3 times the width of the noise distribution, $Q_{\rm rnd}$. The nominal operating threshold of 1 fC, designed to give 99% efficiency, therefore dictates that the RMS noise be less than 0.3 fC, equivalent to the charge on 1900 electrons (1900 ENC). This limit accounts for the anticipated lifetime of the experiment: the design limit on the noise is 1500 ENC, which includes the contributions from the detectors and the ASICs.

A summary of the design specifications referred to in this section is given in table 5.1. Comprehensive testing of the modules is required to ensure they meet these standards and the system test, the subject of the next section, has played a significant role in this quality assurance.

Parameter	Specification
Operating Temperature	-7°C
Operating Threshold	1 fC
Resolution in r-ϕ	< 20 μm
Resolution in z	< 1000 μm
Noise	< 1500 e^-
Occupancy due to noise	$< 5 \times 10^{-4}$

Table 5.1: Specified operating conditions, resolution and noise performance of the SCT modules.

5.3 The SCT Barrel System Test

The system test of the barrel SCT [84] was conducted at CERN from 2000 to 2003. Its primary goal was to operate as many of the modules as possible in a configuration as close as possible to that of the final SCT, thereby testing the behaviour of the modules in such a system and comparing to their stand-alone performance. The system test also served as a test-bed for various grounding and shielding options.

5.3.1 Setup of the System Test

The system test simulated a section of the inner-most SCT barrel in all the details of the mounting, cooling, supply and shielding of the modules. A drawing of the barrel design is shown in figure 5.4. Figure 5.5 is a photograph of the actual system test arrangement, the key components of which are outlined below. For a full description refer to [84, 85].

Mechanical Support

The modules were mounted on the carbon-fibre sector by further carbon-fibre brackets. The sector could accommodate a maximum of four rows of 12 modules, though not all positions were instrumented with power tapes and read-out fibres (see below).

A plastic cover was used to shield the modules from light and provide a gas-tight enclosure. Under the usual operating conditions, the enclosed volume was flushed with dry nitrogen, resulting in an atmosphere with a humidity of 40% or less.

Cooling

When operated the modules each produce up to 10 W of heat and this was dissipated by the cooling pipes on to which the baseboards were clamped. Three cooling pipes

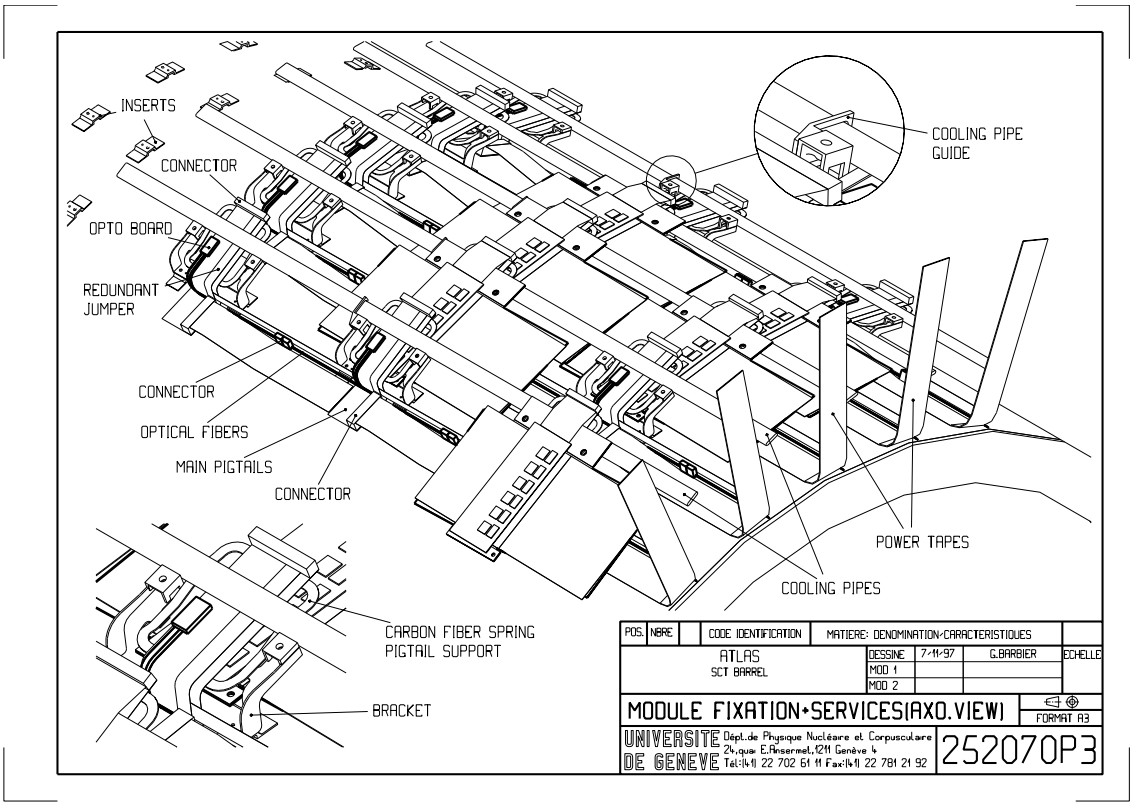

Figure 5.4: The design of an SCT barrel as used at the system test [86].

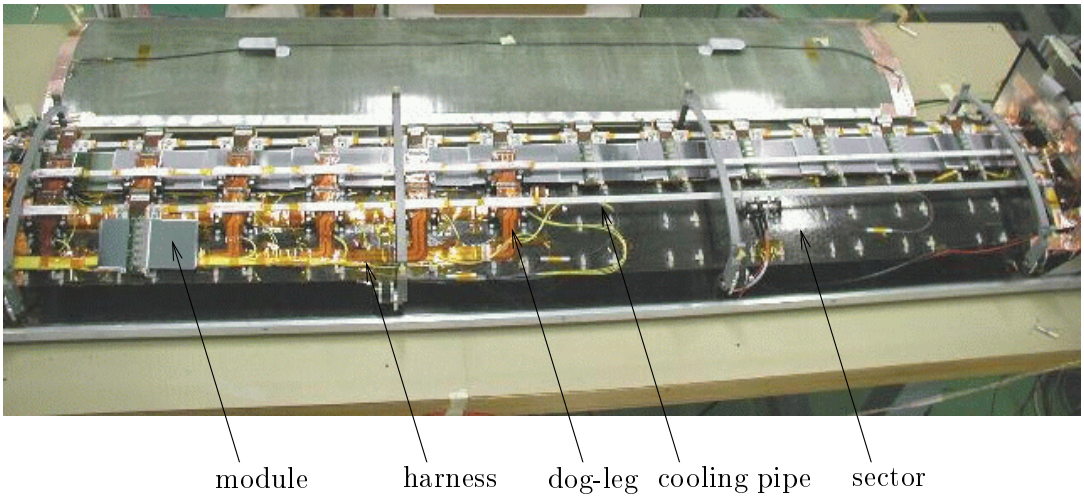

Figure 5.5: Photograph of the barrel system test populated with 13 modules, including one full row of 12

ran the full length of the sector. An ethanol-water mixture was pumped through the pipes at 10°C, keeping the operating temperature of the modules at around 25°C.

Power Delivery and Data/Command Transfer

The modules were powered and read out by prototype opto-harnesses [87]. These consisted of 50 μm thick aluminium-on-kapton tapes to deliver the low voltage (LV) power to the ABCD chips and the high voltage (HV) for the detector bias, together with optical fibre bunches for the transfer of command signals and data packets to and from the chips, respectively. Each harness could serve 6 modules and they entered from either end of the sector: there were three harnesses to supply 18 modules on one half of the sector with a further single harness entering from the other end to supply 6 more modules there. Thus, at most one full row of 12 modules, plus two additional half rows of 6, could be operated.

Each module was interfaced to the power lines on the main opto-harness with a *dog-leg*. These also held the *opto-package* which converted both the optical commands sent to the chips to electrical signals and the data from the chips to optical signals for transmission to the DAQ system. The chips were operated at their nominal voltages of 3.5 V for the analogue and 4 V for the digital circuits. The detectors were biased at 100 V.

Power Supply and Read-Out Scheme

Power supply and read-out were provided by a VME-based system drawn schematically in figure 5.6 [88]. LV power for the chips and opto-packages and the HV detector bias came from the SCT-LV and SCT-HV components, respectively. The CLOAC and SLOG generated the 40 MHz clock, command and trigger signals. These were both connected to the OPTIF, which converted the commands from electrical to optical signals for transmission to the modules and the data received from the chips back to electrical signals for subsequent decoding by the MUSTARD. The system was controlled by the ROOT-based DAQ software SCTDAQ [89] running on a win-

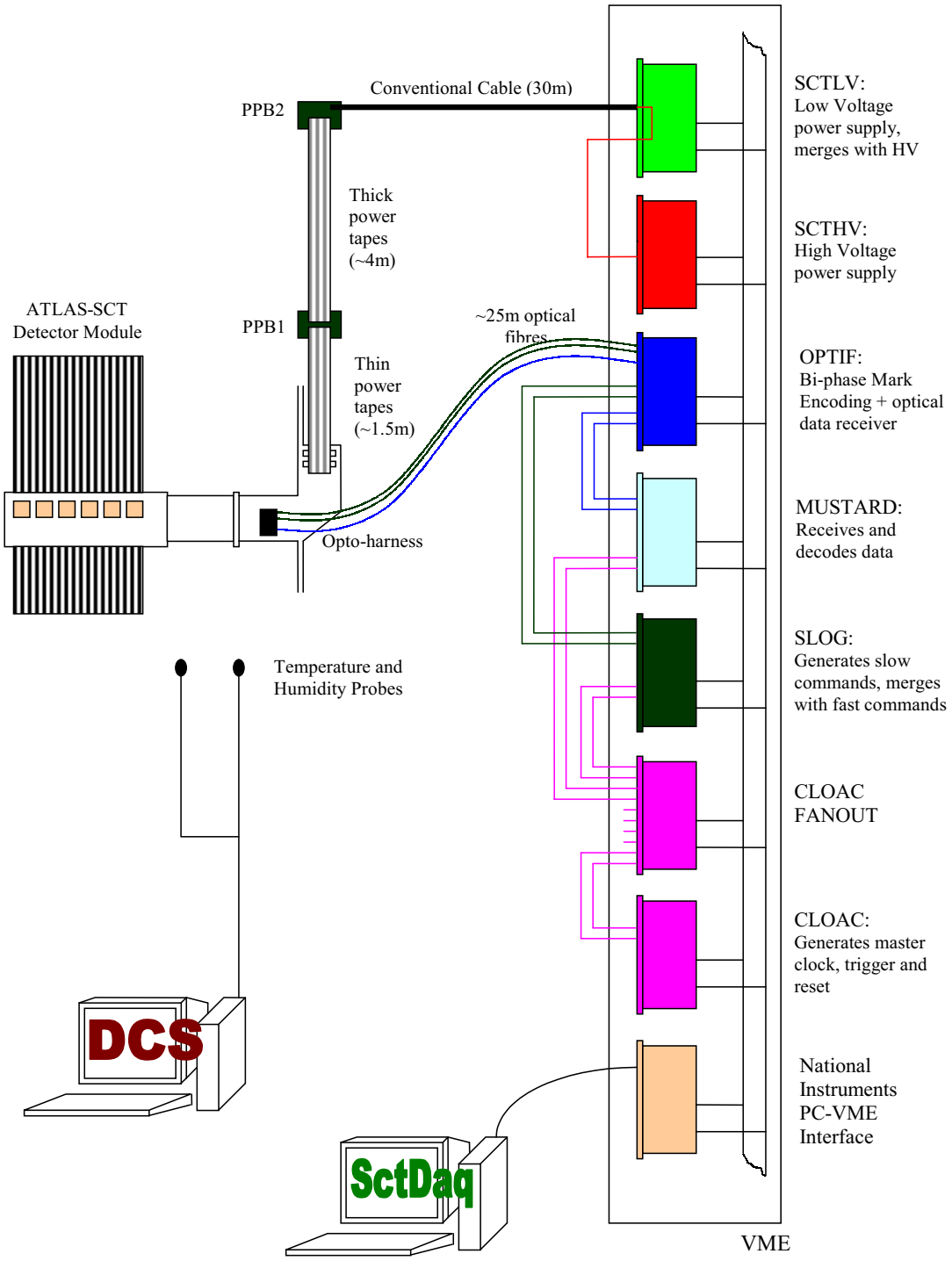

Figure 5.6: The system-test DAQ-system.

dows NT PC connected to the VME system via a National Instruments interface card. A second PC was used to run the Detector Control System (DCS) to monitor the ambient and cooling pipe temperatures and the humidity.

Shielding

The system test considered two alternative grounding and shielding schemes. However, in the absence of extra noise being forced into the system, no difference between the two schemes was observed. All results shown here are for the "standard configuration": refer to [84] and [90] for the precise details.

5.3.2 Analysis Methods and Results

Results are presented here of tests with one full row of 12 modules. The two halves of the row were served by independent harnesses so this configuration checked for possible interference effects between them. The results are interpreted by comparison not only to the SCT design specifications but with reference to each module's stand-alone performance recorded on the electrical-read-out test bench. Before being operated on the sector, all modules were first tested on this electrical stand, which bypassed the optical link and had well controlled shielding, with the module under test sitting in a grounded metal box. In principle the modules' optimal performance should have been returned in this system.

Three Point Gain Scans

These scans were used to find the amplifier gain and the noise, Q_{rnd}, for all channels of the modules. Triggers were issued at a few tens of kHz in conjunction with a known amount of charge being injected into every channel from the calibration circuits on the ABCD chips. The channel occupancies were measured as a function of the threshold in mV, yielding the characteristic S-curve for each channel charting the fall in occupancy with increasing threshold. The responses (in mV) of the amplifiers

to the injected charge were then obtained from the threshold values at which the occupancies had fallen to 50%. In the so called "three point gain" approach, the 50% points were plotted for input charges of 1.5, 2.0 and 2.5 fC and the gain determined from the slope of this response curve. The gain was then used to derive Q_{rnd} from the width of the S-curve obtained from the 2 fC scan. Gain and ENC values averaged over the 128 channels of each chip are usually quoted.

Figure 5.7 compares the ENC values measured from the row of 12 modules operated on the sector with each one's individual noise performance on the electrical stand. In this and all following similar plots, the module names on the x-axis reflect the physical arrangement of the modules on the sector. The multi-module results are comparable to those seen on the electrical stand. The general trend for the multi-module noise values to be slightly lower most likely resulted from the pre-biasing of the detectors when operated on the sector (see below). Typical noise values were around 1600 ENC compared to the specified limit of 1500 ENC. However, the specification applies to the low temperature (-7°C) conditions within ATLAS and an improvement of approximately 6 ENC per 1°C temperature decrease can be expected over the room temperature results shown here [84].

Noise Occupancy Scans

In these tests the occupancy arising from noise alone was measured, in the absence of any injected charges. Results are quoted at the nominal operating threshold (1 fC), at which the noise occupancy should be less than 5×10^{-4}. As shown in figure 5.8 all modules performed well within this noise occupancy limit, despite being outside the Q_{rnd} ENC limit as measured with the three point gain scans.

The noise occupancy as a function of the threshold measured in units of charge, Q_{thr}, could be obtained by scanning Q_{thr} and sending varying numbers of triggers, between 2000 and 10^6, to compensate for the decreasing number of noise hits as the threshold was increased. Assuming a Gaussian random noise distribution for each

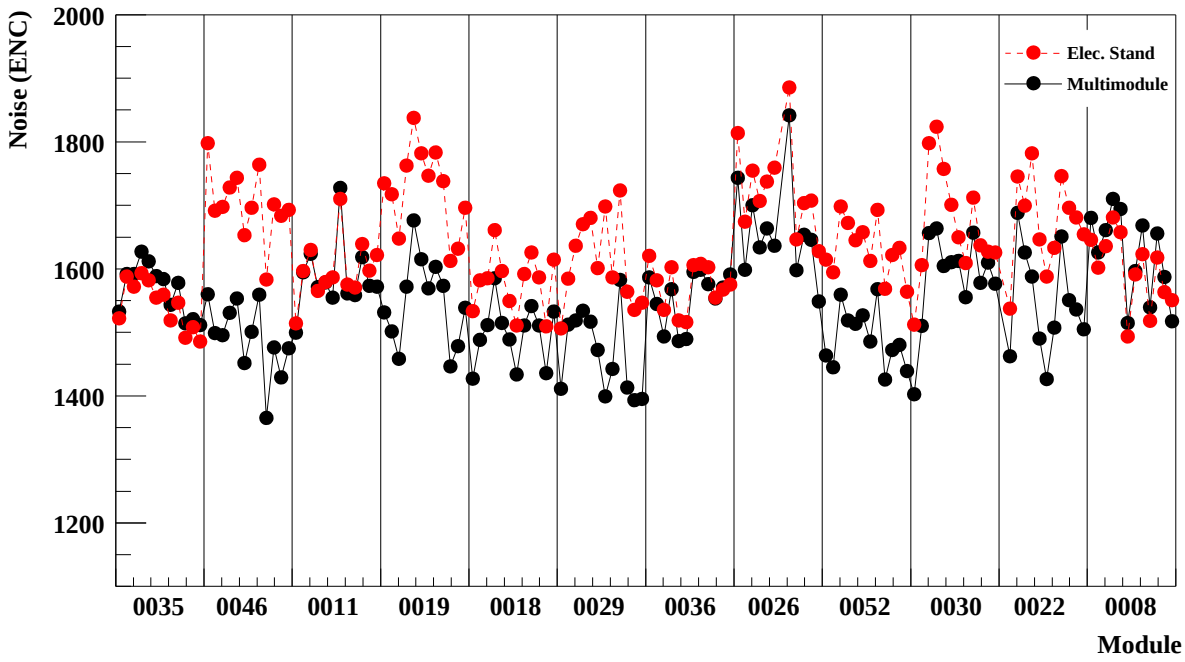

Figure 5.7: The ENC values by chip as derived from three point gain scans, comparing module performance in a row of 12 on the sector with their stand-alone performance. The module names are given on the x-axis: the 12 points per module correspond to the chip averaged noise values. The ENC values are in units of the electron charge.

channel, the occupancy O should vary with the $Q_{\rm thr}$ for $Q_{\rm thr} \gg Q_{\rm rnd}$ as

$$\ln O \approx -\frac{1}{2}\frac{Q_{\rm thr}^2}{Q_{\rm rnd}^2}.$$

The resulting linear dependence of $\ln(O)$ on $Q_{\rm thr}^2$ seen in one chip is shown in figure 5.9. Any deviations from such behaviour are indicative of non-Gaussian noise pick-up: none are seen.

The $Q_{\rm rnd}$ values in ENC extracted from the slopes of $\ln(O)$ vs $Q_{\rm thr}^2$ for all chips are shown in figure 5.10. The noise occupancy method therefore offers an alternative way of determining the ENC values to the three point gain scans. The two approaches are not completely independent, however, since the three point gain scans are required to measure the gain and thereby allow $Q_{\rm thr}$ to be found from the threshold DAC value in mV. The input noise values given by the noise occupancy method are slightly lower than those obtained from the three point gain scans, which is consistent with

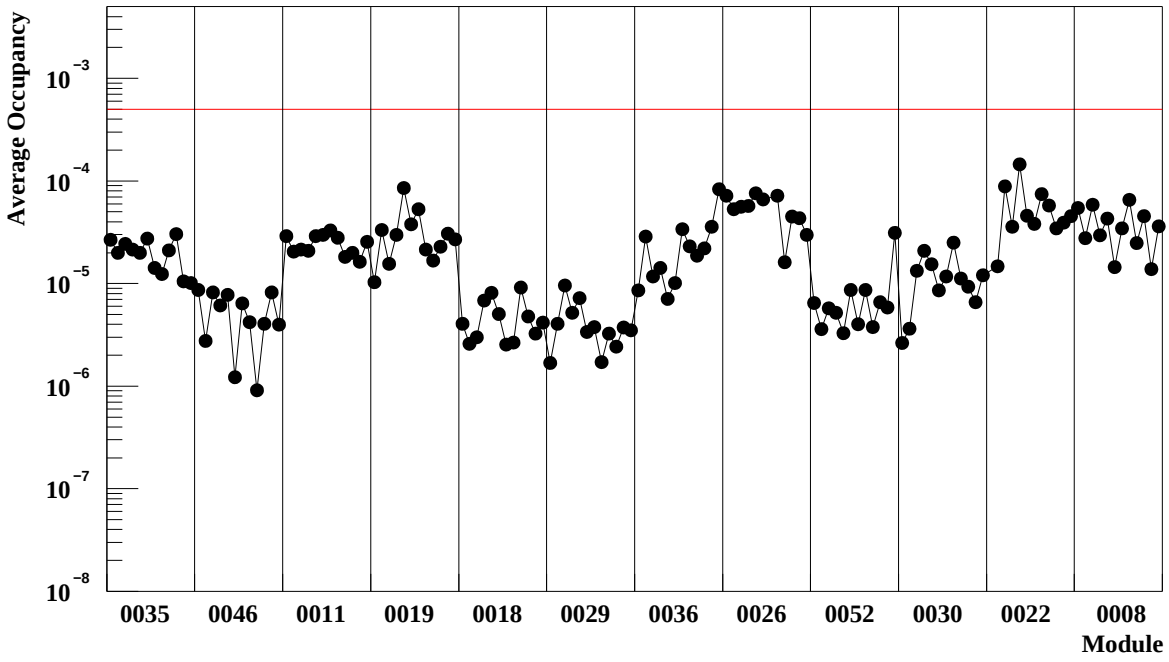

Figure 5.8: The noise occupancy values at 1 fC threshold by chip for a row of 12 modules on the sector, compared to the specified limit of 5×10^{-4}. The module names are given on the x-axis: the 12 points per module correspond to the chip averaged noise values.

the observation that the three point gain scans recorded lower noise values when lower values of injected charge were used: the noise measured with a 0.5 fC injected signal was approximately 20% lower than with a 2 fC injected signal.

Repeated Noise Measurements

The ENC by chip was measured over a sustained period of time, either by repeating the three point gain or noise occupancy scans. If the modules were biased for several hours before commencing the data taking, the noise occupancy tended to be stable, as shown in figure 5.11(a). However, if the measurements commenced immediately after biasing the detectors, the noise occupancy was seen to decrease with time. An extreme example is shown in figure 5.11(b). Following subsequent investigation, this trend is understood in terms of the similar change with time seen in the inter-strip

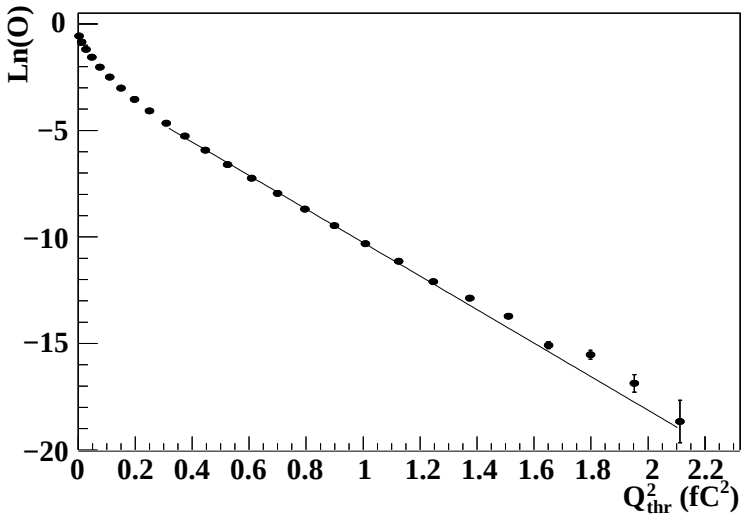

Figure 5.9: The typical ln-occupancy versus $Q^2_{\rm thr}$ behaviour of one chip. The ABCD chips are not designed to be operated with their threshold set close to zero. It is concluded that no deviations from the linear dependence, which would indicate non-Gaussian noise pick-up, are seen.

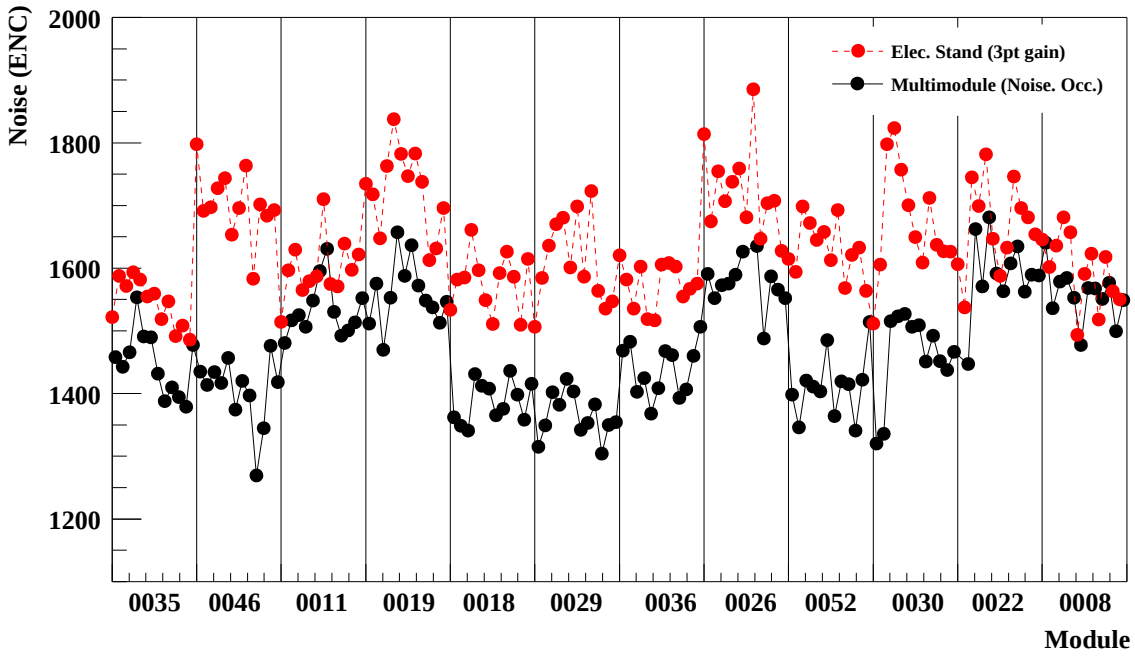

Figure 5.10: The ENC values by chip comparing between a row of 12 modules on the sector with their stand-alone performance, as derived from noise occupancy measurements. The module names are given on the x-axis: the 12 points per module correspond to the chip averaged values.

capacitance of the detectors [91, 92].

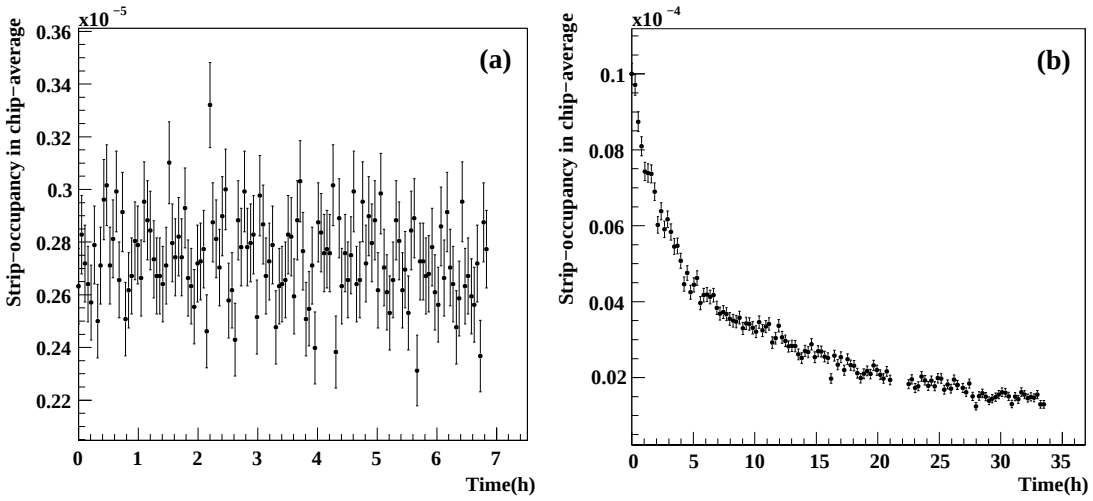

Figure 5.11: The typical noise occupancy values for one chip over a period of several hours with (a) and without (b) pre-biasing of the modules.

Cross Talk

The system test has been the only place to simulate the SCT multi-module arrangement and it was therefore prudent to test for possible cross talk between the detectors when arranged in their true geometry. Real signals were produced in the detectors of one of the modules (0029) using a Sr90 β^- source. These were triggered on using a scintillator connected to the CLOAC external trigger feature. The scintillator was placed underneath module 0029 and the timing and discrimination adjusted for maximum efficiency. During data taking the full hit pattern for every event was recorded. Subsequently, events with a hit in the top and bottom of the target module were selected.

The quantity χ for every channel has been calculated from

$$\chi = \frac{(O_{\rm src} - O_{\rm ref})}{(\sqrt{2}\sigma)}, \tag{5.1}$$

where $O_{\rm src}$ is the probability of a hit in conjunction with a real hit and $O_{\rm ref}$ is a reference occupancy, with spread σ, taken from an equivalent data set collected in

the absence of the source. In the case where $O_{\mathrm{src}} = O_{\mathrm{ref}}$, the χ distribution will be centred on zero with unit spread. As indicated in figure 5.12, neglecting one unmasked noisy channel, no evidence for any cross talk between modules was seen.

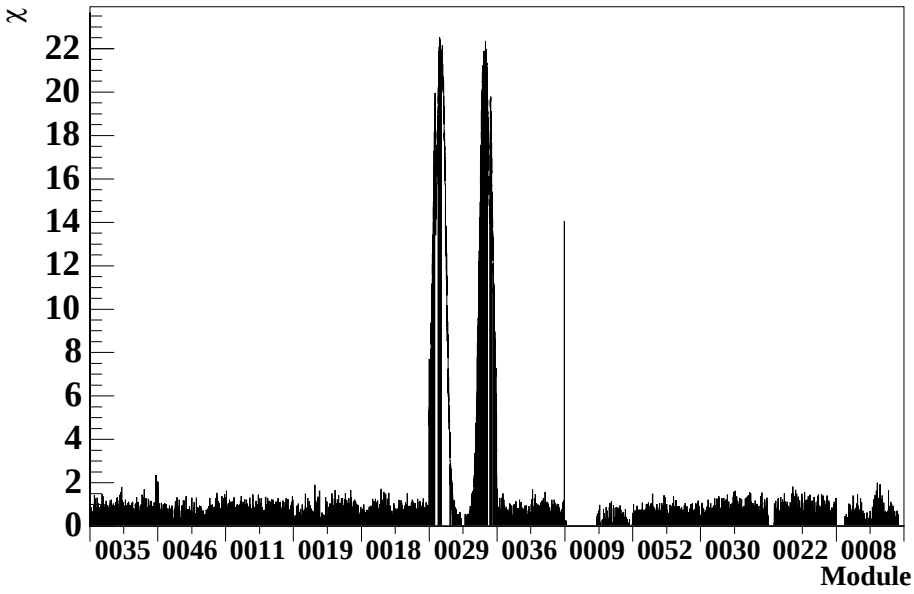

Figure 5.12: The quantity χ of equation 5.1 plotted for all channels. Real hits were generated in module 0029. The results are consistent with there being no cross talk.

5.3.3 Conclusions

System tests with a row of 12 SCT modules showed the noise performance of the modules on the sector to be within the SCT design specifications and comparable to individual module tests. Many other measurements were made, including the use of a different geometry of modules and operating the modules at 0°C. The exhaustive results can be found at [85]. In summary, the system test has been invaluable in providing assurance of the functionality of the final SCT design.

Using the standard analysis tools reported in this section, no indications of non-Gaussian noise pick-up were seen. This motivated more sensitive tests for the presence of common-mode noise, as described in the next section.

5.4 Measurement of Common-Mode Noise

Common-mode noise is of particular concern in the analysis of binary data obtained from analogue signals that may have been affected by coherent distortions. In the case of the SCT, an external noise source in the proximity of the detectors could lead to coherent variations in the signals across groups of channels. If the read-out were analogue, this common-mode contribution could easily be deduced from the pedestal heights and subtracted from the signals on an event by event basis. However, such corrections cannot be made in the binary read-out system employed in the SCT, demanding that the common-mode noise pick-up be negligible.

It is assumed throughout this work that the common-mode source has a Gaussian distribution which adds coherently to the Gaussian random noise on a group of channels. For the SCT modules it is natural to consider such a group to be the 128 channels of a single chip sub-system. Working in this theoretical framework, methods to detect and measure common-mode noise have been reported elsewhere [93]. In the first part of this section this framework is established and the methods reviewed before being extended. In the following section they are applied to a barrel SCT module operated at the system test.

5.4.1 Theoretical Framework

All noise levels are normalised to the single channel random noise, Q_{rnd}. The threshold, τ, is also expressed in units of Q_{rnd}. In this notation, the distribution of the random noise in any channel is now given by

$$P(x) = \frac{1}{\sqrt{2\pi}} \exp\left(-\frac{x^2}{2}\right),$$

which has unit width. The distribution of common-mode noise, z, is

$$P(z) = \frac{1}{\sqrt{2\pi s^2}} \exp\left(-\frac{z^2}{2s^2}\right),$$

and adhering to the usual convention the width s is taken as the magnitude of the common-mode noise, in units of Q_{rnd} ($Q_{\mathrm{cmn}} = sQ_{\mathrm{rnd}}$). The two Gaussians are

convolved to give a total noise distribution

$$P(a) = \frac{1}{\sqrt{2\pi(1+s^2)}} \exp\left(-\frac{a^2}{2(1+s^2)}\right),$$

where $a = x + z$. The observed occupancy above some threshold τ is then given by

$$O(\tau) = \int_{\tau}^{\infty} P(a)da$$

which evaluates to the complementary error function (S-curve),

$$O(\tau) = \frac{1}{2}\mathrm{erfc}\left(\frac{\tau}{\sqrt{2(1+s^2)}}\right).$$

In the three point gain method of measuring the noise performance, the S-curve for each channel is obtained by scanning the threshold whilst injecting a known charge into the amplifier. In the Gaussian approximation, the width of this S-curve is given by the sum in quadrature of the random noise on that channel with any common-mode noise that the channel is sensitive to; $1 + s^2$ in this notation. In principle, s can be determined by comparing to a similar measurement taken in an environment free of common-mode noise, though such a method is likely to be insensitive to small s due to the extra errors introduced by the change in operating conditions. More sophisticated techniques are therefore required to measure s when the common-mode pick-up is small.

Although the common-mode noise is generally not expected to have a Gaussian distribution, it may still be approximated by a Gaussian when it represents a small component of the total noise and the complementary error function remains a close fit to the S-curves. If the common-mode noise leads to a non-Gaussian behaviour of the total noise it can be detected by employing less refined methods than those described here, for example by looking for non-linear deviations in the $\ln O$ vs Q^2_{thr} behaviour [93].

Any common-mode noise pick-up across the channels of one chip leads to a correlation between their occupancies. The correlation matrix for all channels of a chip therefore gives an immediate indication of the presence of common-mode noise. The amount of correlation gives a measure of the magnitude of the common-mode noise.

The correlation between two channels A and B at some threshold τ is given by [93]

$$C_{AB}(\tau) = \frac{O_{AB}(\tau) - O_A(\tau)O_B(\tau)}{\sqrt{O_A(\tau) - O_A(\tau)^2}\sqrt{O_B(\tau) - O_B(\tau)^2}},$$

where $O_{A(B)}(\tau)$ is the occupancy of channel A (B) and $O_{AB}(\tau)$ refers to the occupancy of channels A and B together, given by the number of common hits divided by the number of events.

The distributions of the *uncorrelated* random noise in channels A and B are given by the Gaussians

$$P_A(x) = \frac{1}{\sqrt{2\pi}} \exp\left(-\frac{x^2}{2}\right),$$

$$P_B(y) = \frac{1}{\sqrt{2\pi}} \exp\left(-\frac{y^2}{2}\right),$$

where it is assumed that the size of the random noise is the same in each channel. Studies of the behaviour of SCT modules have demonstrated that this assumption is a good approximation for the channels of one chip [80]. From these it is possible to define a two dimensional noise distribution, $P(x, y)$, given by the product of the Gaussians associated with each channel:

$$P(x, y) = P(x)P(y).$$

The occupancies above some threshold τ can then be obtained by evaluating the

more general integrals

$$\begin{aligned} O_A(\tau) &= \int_{-\infty}^{\infty}\int_{\tau}^{\infty} P(x,y)dx\ dy, \\ O_B(\tau) &= \int_{\tau}^{\infty}\int_{-\infty}^{\infty} P(x,y)dx\ dy, \\ O_{AB}(\tau) &= \int_{\tau}^{\infty}\int_{\tau}^{\infty} P(x,y)dx\ dy. \end{aligned} \tag{5.2}$$

$O_A(\tau)$ and $O_B(\tau)$ evaluate to the same complementary error function with unit width: the size of the random noise is the same in both channels and so at a given threshold their occupancies are equal. In the absence of common-mode noise, $O_{AB}(\tau)$ is just $O_A(\tau)^2$ (or $O_B(\tau)^2$) giving $C_{AB}(\tau) = 0$: for purely random noise there is no correlation between the occupancies of two channels.

On the introduction of common-mode noise via $P(z)$, the distributions of the total noise in each channel are given by $P_A(a)$ and $P_B(b)$ where as before $a = x + z$ and $b = y + z$. Since $P_A(x + z)$ and $P_B(y + z)$ are correlated by virtue of their common component $P(z)$,

$$P(a,b) = P(x+z, y+z) \neq P(x+z)P(y+z).$$

However, since the three distributions $P_A(x), P_B(y), P(z)$ are all independent

$$P(x,y,z) = P(x)P(y)P(z)$$

and subsequently $P(a,b)$ can be obtained by means of a change of variable to $P(x+z, y+z, z)$ and integration over all z. The result is

$$P(a,b) = \frac{1}{2\pi\sqrt{(1+2s^2)}} \exp\left(-\frac{1}{2(1+2s^2)}((1+s^2)a^2 + (1+s^2)b^2 - 2abs^2)\right).$$

In the absence of common-mode noise ($s = 0$) this reduces once again to the product of two Gaussians. The occupancies $O_A(\tau)$, $O_B(\tau)$ and $O_{AB}(\tau)$ are now given by equations 5.2, replacing $P(x,y)$ with $P(a,b)$ from above. $O_A(\tau)$ and $O_B(\tau)$ are the complementary error function with width $1+s^2$. $O_{AB}(\tau)$ must be solved numerically and is greater than $O_A(\tau)^2$ (or $O_B(\tau)^2$) giving $C_{AB}(\tau) > 0$. The correlation between channels A and B as a function of s is plotted in figure 5.13 for several different thresholds.

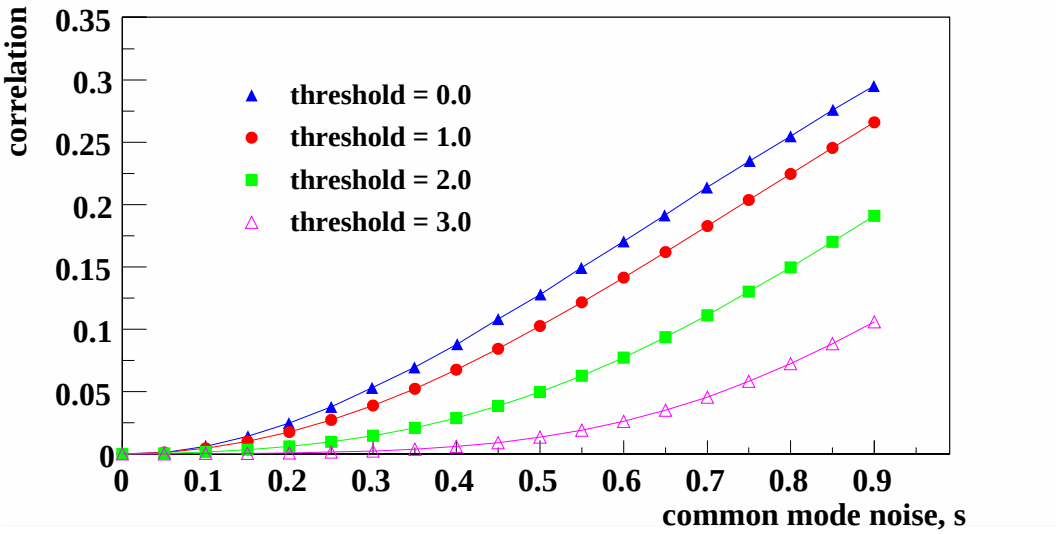

Figure 5.13: The correlation between two channels as a function of common-mode noise, s, for thresholds, $\tau = 0, 1, 2, 3$.

It should be noted that in addition to the correlations between the channels of one chip, it is also possible to measure the correlations between pairs of chips within or between detector modules. The correlation between any two chips C_1 and C_2 is found by averaging the correlations between each channel i of the 128 channels read out by chip C_1 with its counterpart i' of 128 in chip C_2:

$$C_{C_1C_2} = \frac{1}{128} \sum_{i,i'=1}^{i,i'=128} C_{ii'}.$$

This gives the required result that the correlation of any chip with itself is unity.

If the two chips can be represented by two channels A and B, assuming they are both susceptible to the same source of common-mode noise it is possible to write in analogy with the previous section

$$P(a,b) = \frac{1}{2\pi\sqrt{(1+2s^2)}} \exp\left(-\frac{1}{2(1+2s^2)}((1+rs^2)a^2 + (1+s^2)b^2 - 2abrs^2)\right),$$

where r is the ratio of the noise pick-up in chip A to that in chip B. Thus, once the size of the common-mode noise in each chip is known, the correlation between

them is predicted and is generally non-zero if the amount of noise pick-up is not identical ($r \neq 1$). In a matrix of correlations between two chips, then, there is no new information that is not concealed in the unit entries along the diagonal. Chip-chip correlations are not considered any further here.

Coherent Occupancy Method

Any common-mode noise causes coherent fluctuations in the occupancies of groups of channels from one event to the next above or below that expected from purely random noise. The distribution of the number of channels in an event registering a hit above threshold, N_{ev}, is therefore sensitive to common-mode noise. In the absence of common-mode noise the N_{ev} distribution is binomial, denoted by $P(N_{\mathrm{ev}}) = \mathrm{Bin}(N_{\mathrm{ev}}; O(\tau))$ for a hit probability $O(\tau)$ and threshold τ. The mean number of hits is given by the binomial mean

$$\overline{N_{\mathrm{ev}}} = nO(\tau),$$

where there are $n = 128$ channels and the variance of the distribution is

$$\mathrm{Var}(N_{\mathrm{ev}}) = nO(\tau)(1 - O(\tau)) = \overline{N_{\mathrm{ev}}}(1 - \overline{N_{\mathrm{ev}}}/n).$$

Hence the expected variance can be found from the observed mean number of hits per event, $\overline{N_{\mathrm{ev}}}$. An observed distribution wider than this indicates the presence of common-mode noise. To measure the size of this common-mode contribution requires quantifying the difference between the observed and expected variances of the N_{ev} distribution.

A common-mode noise contribution to the random noise signal is equivalent to shifting the threshold for all channels susceptible to the common-mode noise in the opposite direction by the same amount. Assuming Gaussian common-mode noise, this shift can be modelled by giving the thresholds a Gaussian distribution [93]:

$$g(\tau) = \frac{1}{\sqrt{2\pi s^2}} \exp -\frac{(\tau - \tau_0)^2}{2s^2},$$

where τ_0 is the original threshold. The $N_{\rm ev}$ distribution becomes a superposition of binomial distributions for varying thresholds,

$$P(N_{\rm ev}) = \int_{-\infty}^{\infty} \mathrm{Bin}(N_{\rm ev}; O(\tau)) g(\tau) d\tau$$

which has a mean

$$\overline{N_{\rm ev}} = \int_{-\infty}^{\infty} n O(\tau) g(\tau) d\tau$$

and variance

$$\mathrm{Var}(N_{\rm ev}) = \overline{N_{\rm ev}}(1 - \overline{N_{\rm ev}}) + n(n-1) \int_{-\infty}^{\infty} O^2(\tau) g(\tau) d\tau$$

The observable Γ was introduced in [93] where it was defined as

$$\Gamma^2 = \frac{\sin(\alpha)}{1 - \sin(\alpha)}$$

with

$$\alpha = 2\pi \frac{\mathrm{Var}(N_{\rm ev}) - \overline{N_{\rm ev}}(1 - \frac{\overline{N_{\rm ev}}}{n})}{n(n-1)}.$$

If the observed variance is equal to that expected from binomial statistics then Γ and the common-mode noise contribution are zero, no matter how many channels there are or how the threshold is set. Figure 5.14 shows Γ plotted as a function of s for several different thresholds. Defined in this way, Γ has the useful property of approximating the ratio of common-mode noise to single channel random noise when operating at the 50% occupancy point ($\tau = 0$). However, it is unlikely that detectors would really be operated in this regime, and the measurement of common-mode noise at high thresholds will be more important (see next section) at which Γ loses much of its sensitivity. This motivates the definition of an alternative observable, Ω, given by

$$\Omega = \frac{n}{(n-1)} \left(\frac{\mathrm{Var}(N_{\rm ev})}{\overline{N_{\rm ev}}^2} - \frac{1}{\overline{N_{\rm ev}}} + 1 \right) - 1.$$

Again, Ω quantifies the difference between the observed and expected variances but is now chosen so that the first term in the brackets leads to the cancellation of the $O(\tau)$ in the integral expressions for $\overline{N_{\rm ev}}$ and $\mathrm{Var}(N_{\rm ev})$ which previously rendered Γ less sensitive in the high threshold, low common-mode noise regime. Ω is plotted in figure 5.15.

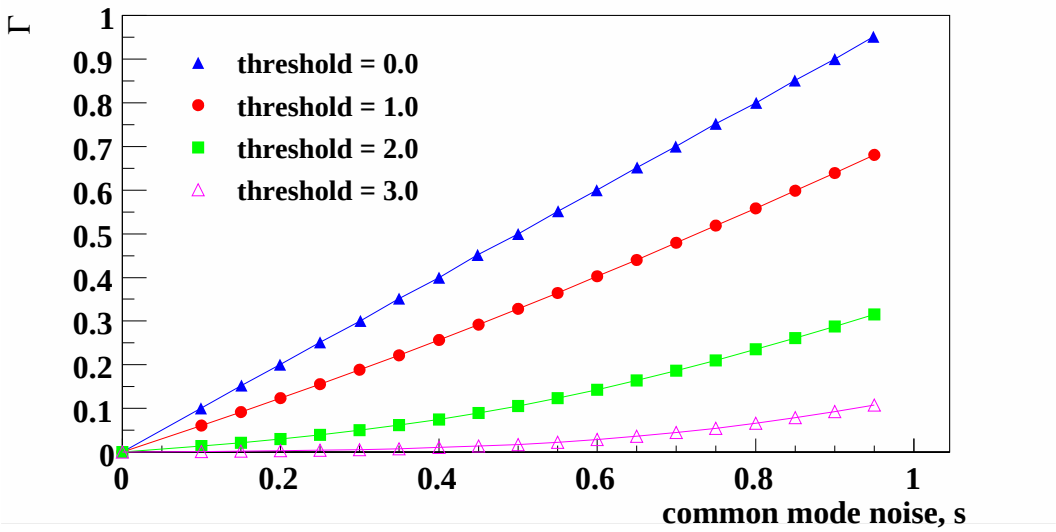

Figure 5.14: The observable Γ as a function of common-mode noise, s, for $\tau = 0, 1, 2, 3$.

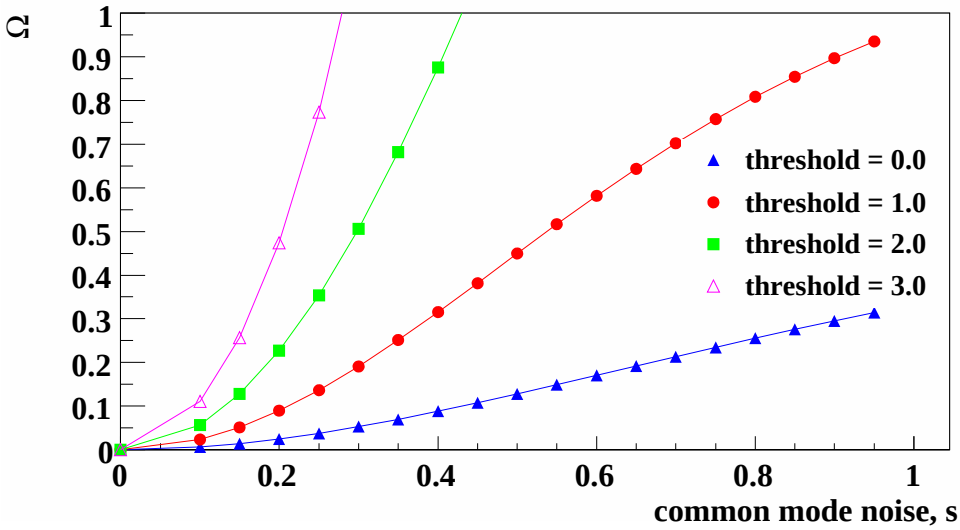

Figure 5.15: The observable Ω as a function of common-mode noise, s, for $\tau = 0, 1, 2, 3$.

The mathematical assumptions of both methods require that the thresholds for all channels in the chip under consideration be identical. This is achieved through the "trimming" procedure [89] in which the offsets for all channels within a chip, or ideally an entire module, are adjusted to equalise their physical thresholds for a globally set DAC threshold. The residual spread in the thresholds of the 128 channels about their set value is not modelled in either method. In addition, this tuning is optimised at the nominal operating threshold of the detectors. Since the gain is not precisely the same for all channels, the further the threshold is moved from its nominal setting the more dispersed the threshold becomes. Some variation of the results with threshold is therefore to be expected, and the best estimate for the common-mode noise will be obtained when the threshold is set as close as possible to its nominal value.

5.4.2 Application of Methods to the SCT

The two methods described in the previous section were applied to six ATLAS SCT modules operated on the sector. The results for one of the modules are discussed in this section, though similar findings were obtained using the others. It was known that coherent noise effects in the system used were small [84] and so common-mode noise was created by injecting a 10 MHz sine wave signal into the shield that surrounded the detectors. It is assumed that the noise measured without this injection is purely random. The S-curve for every channel of each of the twelve chips was measured with and without the noise injection and the results averaged by chip, to give the total noise Q_{tot} and the random noise Q_{rnd} for each chip, respectively. The quadratic difference between these noise measurements gives a measure of the size of the common-mode noise pick-up in each chip, $s = Q_{\mathrm{cmn}}/Q_{\mathrm{rnd}}$, from $Q^2_{\mathrm{cmn}} = Q^2_{\mathrm{tot}} - Q^2_{\mathrm{rnd}}$. This is plotted by chip in figure 5.16. The error bars arise from the estimated error on the measured S-curve random and total noise values.

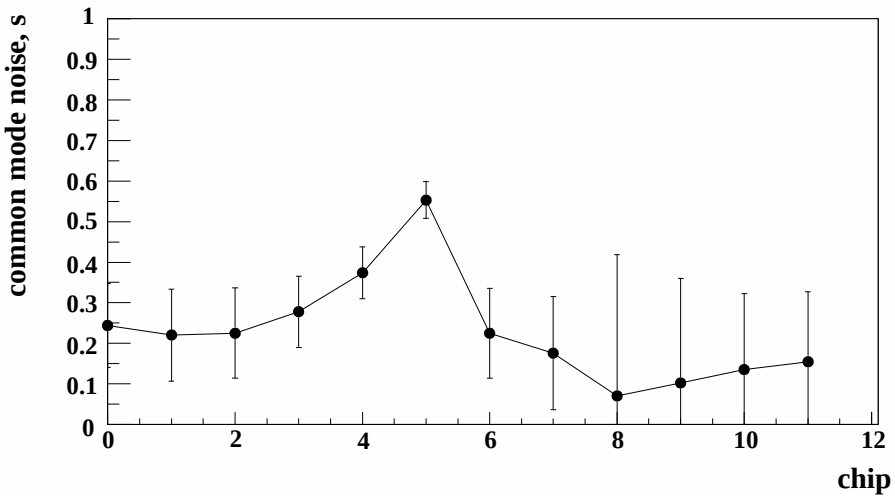

Figure 5.16: Common-mode noise by chip, obtained from the quadratic difference between the S-curve noise values Q_{rnd} (without noise injection) and Q_{tot} (with noise injection).

The nominal operating threshold for the SCT is 1 fC. Thus, for the reasons given in 5.4.1, the common-mode noise was sought when operating with the threshold set as close as possible to this value. Normalising to the typical random noise in the system gives $\tau \approx 4.5$. In practice, therefore, it was necessary to compromise on the threshold such that in a reasonable time sufficient events could be read out to provide adequate statistics. This was particularly relevant when applying the correlation matrix method, for which the data taking and analysis routines were slow due to the need to read-out the full hit pattern in the detector on an event by event basis.

The Correlation Matrix Method

The theory for the correlation matrix method outlined in section 5.4.1 considers only a two-channel system. To obtain a value for the noise pick-up within a chip therefore requires some average of the correlations between all the channel-pairs of that chip, $\overline{C_{AB}(\tau)}$. The correlation matrices obtained for the 12 chips are shown in figure 5.17.

The distribution of strip-strip correlations is approximately uniform within any one chip but varies notably between chips, reflecting the spatial distribution of noise pick-up across the module seen in figure 5.16: chip 5 clearly shows the greatest noise pick-up, due to its proximity to the cooling pipe, and correspondingly the most notable strip-strip correlations.

The individual plots of the correlations between the channels of one chip are approximately uniform, so the chip-average $\overline{C_{AB}(\tau)}$ was obtained from

$$\overline{C_{AB}(\tau)} = \frac{\overline{O_{AB}(\tau)} - \overline{O_A(\tau)}\;\overline{O_B(\tau)}}{\sqrt{\overline{O_A(\tau)} - \overline{O_A(\tau)}^2}\sqrt{\overline{O_B(\tau)} - \overline{O_B(\tau)}^2}},$$

by measuring the quantities $\overline{O_A(\tau)}(= \overline{O_B(\tau)})$ and $\overline{O_{AB}(\tau)}$ representative of that chip.

The theory then predicts how $\overline{C_{AB}(\tau)}$ should vary with the ratio of common-mode noise over random noise, s, at a given threshold. However, the intrinsic random noise will generally be unknown as the S-curves yield Q_{tot} in the presence of common-mode noise. Given the quadratic relation between Q_{rnd}, Q_{tot} and Q_{cmn}, however, it is possible to convert observations on the correlation and the total noise into the size of the common-mode noise expressed as s using an iterative technique.

The results at 0.2, 0.4 and 0.6 fC threshold, based on samples of 100 000, 300 000 and 500 000 events, respectively, are shown in figure 5.18. The precision on the common-mode noise measurement in each chip is limited by the error on the total noise values obtained from the S-curve chip-averages and the statistical errors on the measurements of $\overline{O_A}$ and $\overline{O_{AB}}$, which worsen at higher thresholds, requiring larger sample sizes as τ is increased. At 0.6 fC the large number of events required to measure $\overline{O_{AB}}$ with reasonable accuracy became prohibitive to any further increase in threshold.

The Coherent Occupancy Method

As with the correlation method, an iterative technique has to be employed to convert the measured values of Ω into common-mode noise values by chip, given the chip-

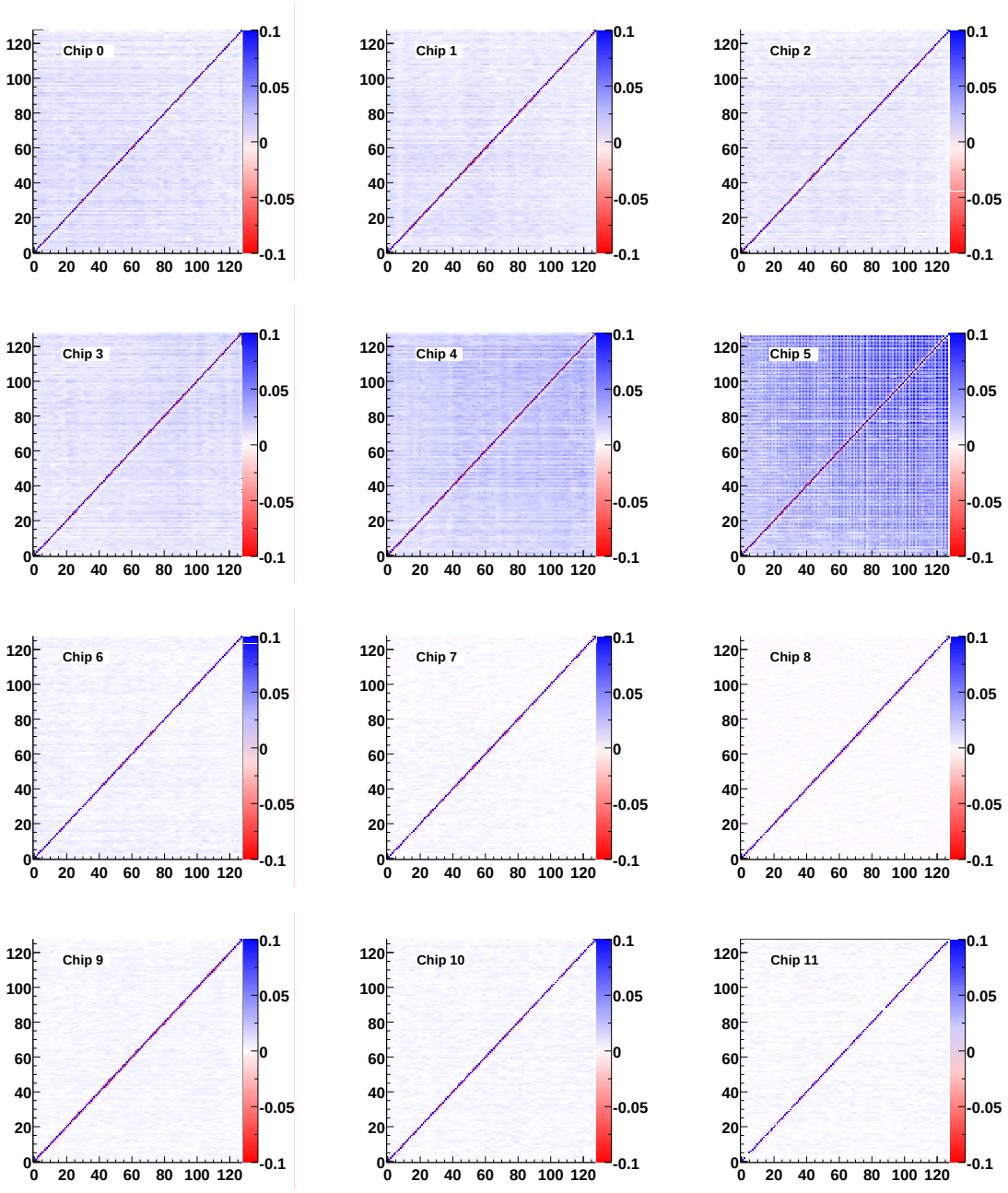

Figure 5.17: Correlation matrices seen with noise injection. The x- and y-axes indicate the channel number from 0 to 127 and the gray-scale shows the amount of correlation. It is evident that the greatest noise pick-up was seen by chip 5.

averaged measured values of Q_{tot}. Since the measurement of Ω requires the recording only of the total number of hit strips per event, not the actual hit pattern, faster data taking permits higher thresholds to be used. The results at thresholds up to 0.8 fC (1 000 000 events) are shown in figure 5.19.

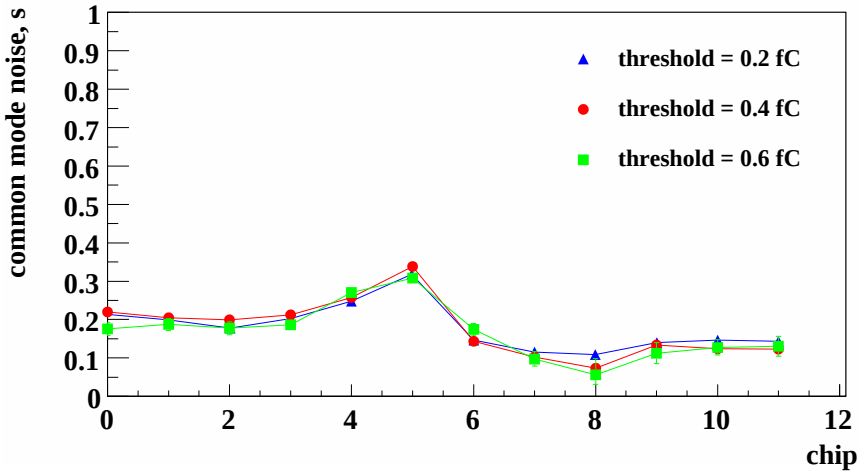

Figure 5.18: Common-mode noise by chip from the correlation method at 0.2, 0.4, 0.6 fC threshold.

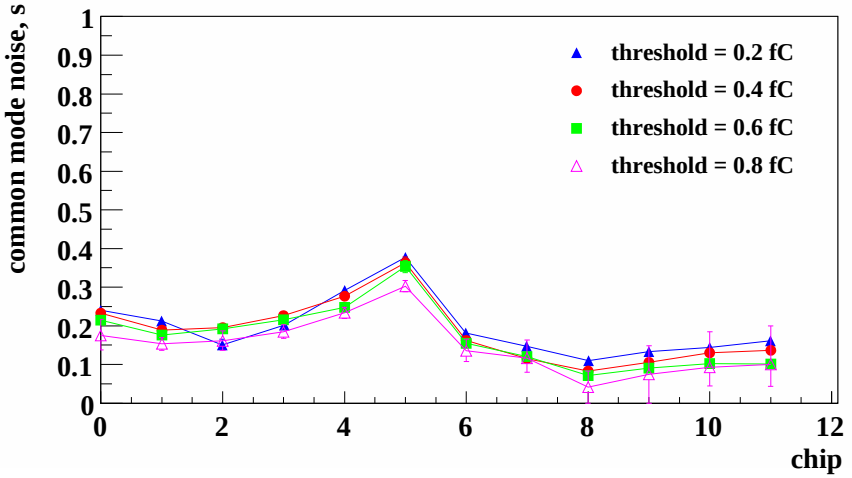

Figure 5.19: Common-mode noise by chip from the Ω method at 0.2, 0.4, 0.6, 0.8 fC threshold.

Good agreement is seen between the two methods and the shape of the distribution of the common-mode noise across the chips is in agreement with that seen from the direct comparison of the random and total noises in each chip taken from their respective S-curves. However, the results from both methods tend to underestimate the common-mode noise compared to this direct measurement. This may be explained by the different ways in which noise is measured. The S-curves whose widths give the total noise Q_{tot} are obtained using 2 fC signals injected into the amplifiers, whereas no charge is deliberately injected when obtaining the correlation matrices or the N_{ev} distributions. As mentioned in 5.3.2, the noise measured at the input to the amplifiers depends on the size of the signal presented. With larger injected signals, the measured noise tends to be higher, which could lead to the higher values for the common-mode noise deduced from the three-point-gain measurements.

5.4.3 Summary

Common-mode noise in a system where the data are read out using a binary scheme can be measured in several ways. It leads to measurable correlations between the occupancies of groups of channels. Alternatively, the effect of coherent noise pick-up on the N_{ev} distribution for a group of channels may be used to measure the magnitude of the pick-up. Either method relies only on information taken from the system in the presence of common-mode noise; no bench mark ($s = 0$) measurements are necessary for comparison.

The effect of an unmodelled dispersion in thresholds has been investigated using a Monte Carlo technique and is found to be a reduction in the observed variance and therefore Ω, for a given level of common-mode noise. The effect is small, however: with a threshold of 0.6 fC, an unmodelled typical Gaussian spread of 0.05 fC would result in a common-mode noise pick-up of $0.2Q_{\mathrm{rnd}}$ being underestimated by 5% by the coherent occupancy method. For the correlation matrix method the effect of any

threshold dispersion is cancelled by the act of averaging over the chip. The effect on the results shown in figures 5.18 and 5.19 is negligible. It should be noted that the correct modelling of the Gaussian spread in thresholds becomes important as the spread increases. With an unmodelled 0.12 fC dispersion, a $0.2Q_{\mathrm{rnd}}$ common-mode noise pick-up would be underestimated by 20%. Large dispersions in the threshold may arise after irradiation of the detectors and front-end electronics.

The method based on the average occupancy per event is much faster than the correlation matrix method, since it requires only the total number of hit strips per event to be recorded. This saves the use of slow data taking and analysis routines required to read-out the full hit pattern in the detector on an event by event basis and thereby calculate the correlation matrix. When working with a system in which the nominal threshold is high compared to the random noise, as is the case for the SCT, the Ω method is therefore the most appropriate choice.

5.4.4 Measurement of Common-Mode Noise on the Sector

Having validated the methods, the intrinsic common-mode noise on the sector was measured. The coherent occupancy method was applied, *without* injecting any noise into the shield. The results for the 12 module test are shown in figure 5.20, based on a sample of 500 000 events taken at a threshold of 0.8 fC. The errors are generally large due to the low total noise, but the upper limit on the common-mode noise pick-up was found to be less than 300 ENC. For most chips, Q_{cmn} was between 100 and 150 ENC. The modules which showed the smallest uncertainty on common-mode noise were those with comparably high total noise, such as 0026, though the actual common-mode noise component for these was not any higher than in the other modules. Thus, no pattern in the noise pick-up was seen and it is concluded that the variations in the total noise resulted only from the differing levels of random noise in the modules.

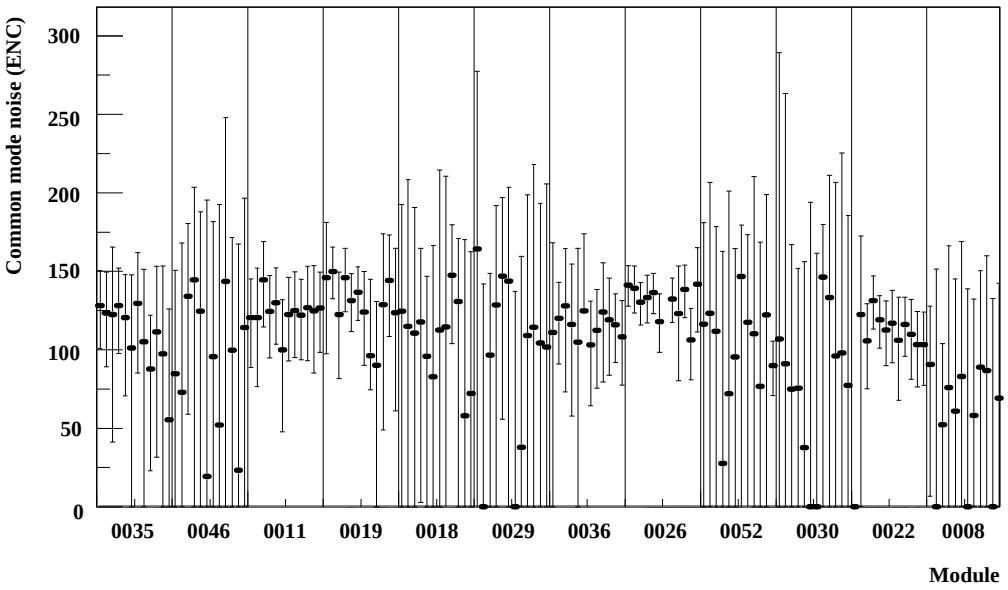

Figure 5.20: The common-mode noise values in ENC by chip for 12 modules operated on the sector. The module names are given on the x-axis: the 12 points per module correspond to the chip averaged values.

Chapter 6

The W$\gamma\gamma$ Process at ATLAS

In this final chapter an introductory Monte Carlo study of the $q\overline{q} \rightarrow W\gamma\gamma$ process at the LHC is presented. This process is sensitive to a possible anomalous $WW\gamma\gamma$ vertex. The Monte Carlo generator W2GRAD implemented as part of the ATLFAST detector simulation program is used to model the $l^{\pm}\nu_{l^{\pm}}\gamma\gamma$ final state at ATLAS. The principal backgrounds, which are expected to arise from events in which jets are mis-identified as photons, are also evaluated.

6.1 Physics Processes at ATLAS

The collisions recorded by the detectors at LEP were between elementary electrons and positrons and occurred in the centre-of-mass frame. At the LHC, however, it is composite protons which will collide at $\sqrt{s} = 14$ TeV. It is the partonic constituents of these which can undergo hard scatters and as these partons each carry some unknown fraction of their parent proton's momentum the partonic level interaction does not occur in the centre-of-mass frame. Of the 14 TeV centre-of-mass energy of the protons, only the parton centre-of-mass energy $\sqrt{\hat{s}}$ is available for physics processes.

Since $\sqrt{\hat{s}}$ is a priori unknown, straightforward momentum conservation cannot be

used in the reconstruction of events produced in p-on-p collisions. However, before such a collision takes place, it is known that the momentum in the plane transverse to the beam is approximately zero. The presence of any final state particles with high transverse momentum, p_T, given by $p_T^2 = p_x^2 + p_y^2$, therefore indicates that a hard scatter has occurred. Any missing transverse momentum, p_T^{miss}, within the acceptance and limitations of the detector, can be associated with neutrinos.

Due to its cylindrical symmetry, it is natural to describe events within ATLAS using a coordinate system which takes the beam direction as the z-axis and uses the azimuthal angle, ϕ, with the interaction point as the origin. However, rather than using θ, the pseudorapidity η, given by

$$\eta = -\ln \tan \frac{\theta}{2},$$

is a more useful quantity, since in the limit of massless particles differences in η are invariant under longitudinal Lorentz boosts.

6.2 The W$\gamma\gamma$ Process and AQGCs

The LHC will be able to probe anomalous quartic gauge boson couplings through the processes of vector boson fusion and triple vector boson production. The possibilities for studying the theoretically most interesting quartic vertices which involve four massive gauge bosons, for example through the scattering of W bosons (refer to section 1.2.3), have already been the subject of study (see for example [94]).

The first sign of triple vector boson production at the LHC is likely to come from the W$\gamma\gamma$ process. Tri-boson production of three massive gauge bosons will be much harder to observe, since such processes cannot play a role at $\sqrt{\hat{s}}$ below, for example, $3M_{\text{W}}$, in the case of WWW production. Furthermore, the subsequent decays of all three massive vector bosons must proceed leptonically if the products are not to be swamped by the much larger QCD background. This is to be contrasted with the W$\gamma\gamma$ signal, which will be visible from $\sqrt{\hat{s}} > M_{\text{W}}$ and which has a cross-section leading to observable final states suppressed by only one branching ratio.

As shown in figure 6.1, W$\gamma\gamma$ production is sensitive to the coupling at the WW$\gamma\gamma$ vertex. The effects of a possible AQGC contribution to this vertex on the $q\overline{q} \rightarrow l^{\pm}\nu_{l\pm}$

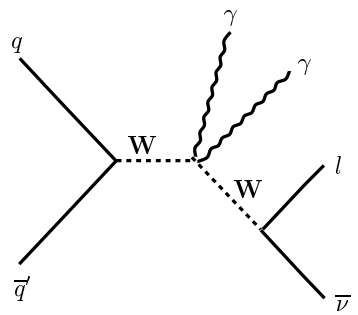

Figure 6.1: The lowest order Standard Model QGC diagram contributing to the W$\gamma\gamma$ process, which may receive an anomalous contribution. The other Standard Model diagrams can be found explicitly in [95].

cross-section at the LHC have been studied in [33]. The authors worked in the same effective Lagrangian framework as that of section 1.2.3, with the condition that $a_0^{\mathrm{Z}} = a_0^{\mathrm{W}} = \beta_0$ and $a_{\mathrm{c}}^{\mathrm{Z}} = a_{\mathrm{c}}^{\mathrm{W}} = \beta_{\mathrm{c}}$. A minimal set of cuts were employed to avoid the infrared and collinear divergences present in the W$\gamma\gamma$ cross-section and guarantee that the photons and the charged leptons were isolated:

- Transverse momentum of photons, $p_{T_\gamma} > 20$ GeV, with psuedorapidity, $|\eta_\gamma| < 2.5$
- Transverse momentum of electron (muon), $p_{T_{e(\mu)}} > 20$ (25) GeV, with pseudo-rapidity $|\eta_{e(\mu)}| < 2.5$ (1.0)
- Transverse momentum of neutrino, $p_{T_\nu} > 20$ GeV
- Separation of final state photons and charged leptons, $\Delta R > 0.4$, (where $\Delta R = \sqrt{(\Delta\phi)^2 + (\Delta\eta)^2}$)

A further cut on the transverse mass of the lepton-neutrino system, $M_T^{(l,\nu)}$, was then imposed in order to select that part of the $l^{\pm}\nu_{l\pm}\gamma\gamma$ signal not arising from final state photon radiation from the charged lepton. This transverse mass is given by:

$$M_T^{(l,\nu)} = (p_{T_e} + p_{T_\nu})^2 - (\vec{p_{T_e}} + \vec{p_{T_\nu}})^2.$$

For W$\rightarrow l^{\pm}\nu_{l\pm}$, $M_T^{(l,\nu)}$ satisfies $0 < M_T^{(l,\nu)} < M_{\mathrm{W}}$ and the distribution of $M_T^{(l,\nu)}$ peaks at the W mass. However, in events in which one or both photons are emitted from the charged lepton, the four momenta of the final state lepton and neutrino will not reconstruct to that of the W, and the transverse mass is reduced below M_{W}. Imposing the cut

$$65 < M_T^{(l,\nu)} < 100 \text{ GeV}$$

therefore selects the W$(\rightarrow l^{\pm}\nu_{l\pm})\gamma\gamma$ part of the total $l^{\pm}\nu_{l\pm}\gamma\gamma$ signal.

Assuming a detector efficiency of 85% for electrons, muons and photons the expected LHC cross-section reported by [33] for $\mathrm{q\overline{q}} \rightarrow \mathrm{W}(\rightarrow l^{\pm}\nu_{l\pm})\gamma\gamma$ using the above selection was 1.08 fb. In 30 fb^{-1} of data, corresponding to the first three years of LHC operation, approximately 32.4 events are therefore expected.

The effects of a possible WW$\gamma\gamma$ AQGC on the distribution of the transverse momentum of the most energetic photon, $p_{T_{\gamma 1}}$, is shown in figure 6.2. The significance of the AQGC contribution can be enhanced by cutting on $p_{T_{\gamma 1}}$ at around 200 GeV, above which there is very little contribution from the Standard Model processes. It was found that the distribution of the invariant mass of the photon pair, $M_{\gamma\gamma}$, offers the greatest sensitivity to the possible anomalous WW$\gamma\gamma$ coupling. This distribution is plotted in figure 6.3.

6.3 Measuring the W$\gamma\gamma$ Process at ATLAS

In this work the W$\gamma\gamma$ process at ATLAS has been studied using events generated by the W2GRAD Monte Carlo program and processed by the ATLFAST [96] detector simulation software. The approach, including the event selection criteria, is described in this section.

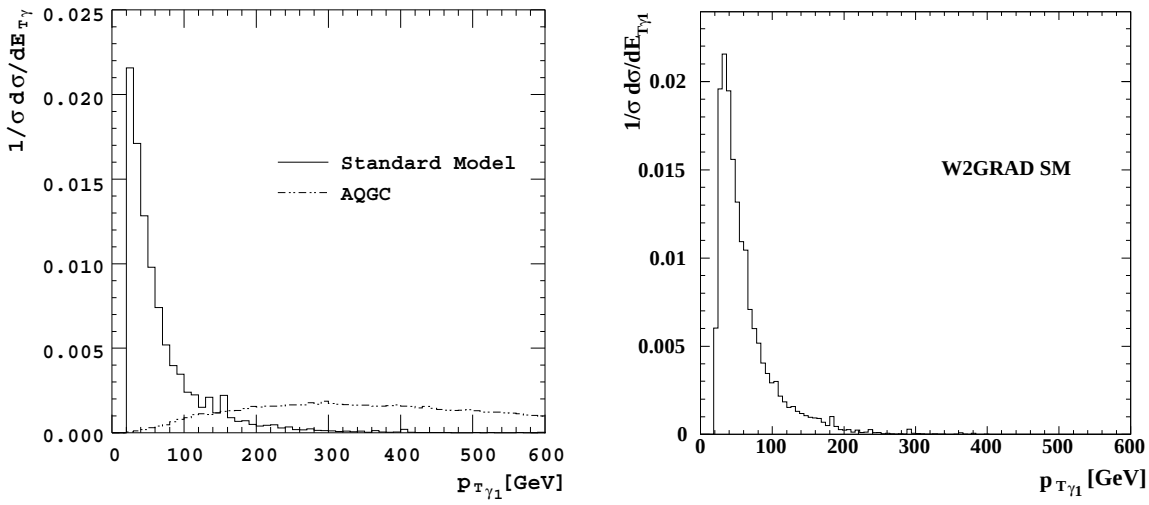

Figure 6.2: Left: The normalised transverse momentum distribution for the most energetic photon in the $q\overline{q} \to l^{\pm}\nu_{l^{\pm}}\gamma\gamma$ process in the Standard Model and with the AQGC parameter $\beta_0 \neq 0$. Taken from [33]. Right: The same Standard Model distribution obtained from the Monte Carlo program W2GRAD: refer to section 6.3.1.

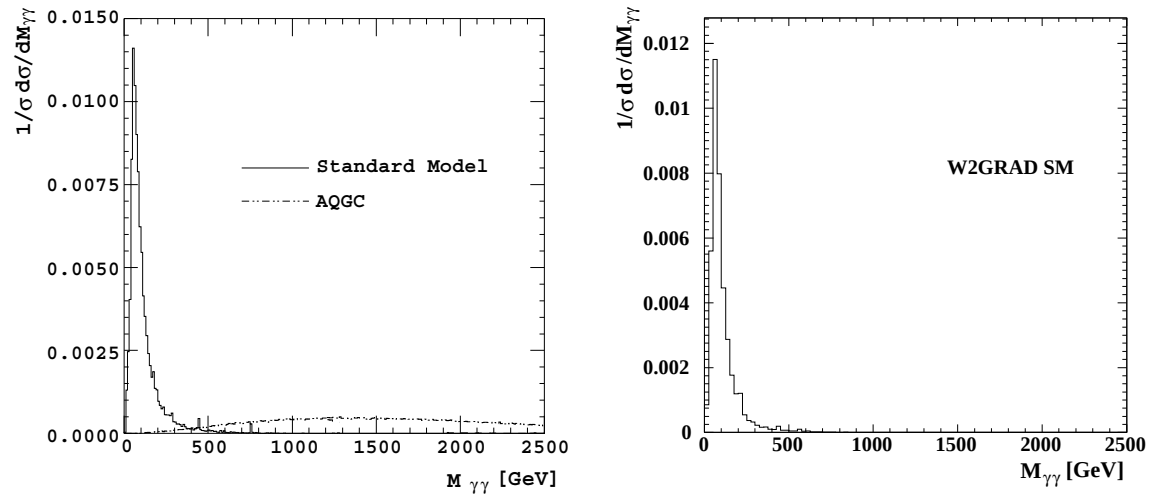

Figure 6.3: Left: The normalised invariant mass distribution for the photon-pair in the $q\overline{q} \to l^{\pm}\nu_{l^{\pm}}\gamma\gamma$ process in the Standard Model and with the AQGC parameter $\beta_0 \neq 0$. Taken from [33]. Right: The same Standard Model distribution obtained from the Monte Carlo program W2GRAD: refer to section 6.3.1.

6.3.1 Monte Carlo Signal Generation

The Monte Carlo program W2GRAD [97] of Baur and Stelzer has been used to generate the W$\gamma\gamma$ signal events at leading order. The program includes all Standard Model diagrams leading to the $l^{\pm}\nu_{l\pm}\gamma\gamma$ final state, including initial state radiation (ISR) and final state radiation (FSR) photons. As a crosscheck, the Standard Model distributions of $p_{T_{\gamma 1}}$ and $M_{\gamma\gamma}$ according to the selection used in [33], described in the previous section, have been reproduced. These are plotted adjacent to the corresponding distributions in figures 6.2 and 6.3: good agreement is seen. For the remainder of this study, only the exclusive channel $q\overline{q} \rightarrow e^{-}\overline{\nu}_{e}\gamma\gamma$ is considered.

6.3.2 ATLFAST Reconstruction and Event Selection

The generated events have been processed by ATLFAST, the fast detector simulation software for ATLAS. The ATHENA version 6.0.3 of the software was used. ATLFAST models the basic geometry of the detector, taking into account the region of precision physics covered by the Inner Detector, the region covered by the calorimetry and the granularity of the calorimeters. Isolated photons, electrons and muons are selected, jets are reconstructed and the missing transverse energy is estimated. ATLFAST makes no allowance for detection efficiencies, so appropriate multiplicative factors have to be applied by hand. Particle mis-identification is also not modelled. The latter is an important factor governing the rate of the principal backgrounds and is the subject of section 6.4.

The W$\gamma\gamma$ events can be triggered in ATLAS through either the two photons having $p_{T_{\gamma}} > 20$ GeV or the electron from the W decay satisfying $p_{T_e} > 25$ GeV [98]. As shown in figure 6.4, the $q\overline{q} \rightarrow e^{-}\overline{\nu}_{e}\gamma\gamma$ cross-section falls sharply as the cut on the minimum photon transverse momentum, $p_{T_{\gamma}}^{\min}$, is increased. To be as inclusive as possible, therefore, the basic selection criteria employed on the quantities reconstructed by ATLFAST are as follows :

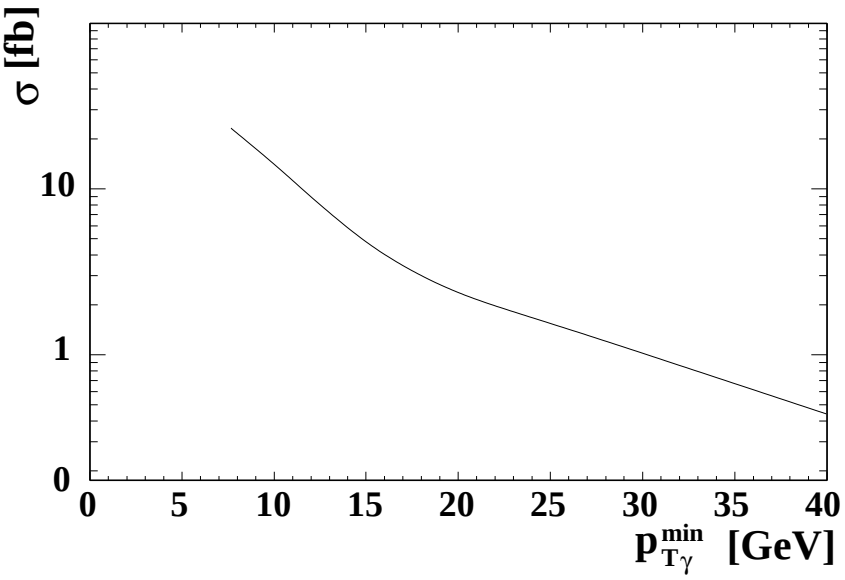

Figure 6.4: The cross-section for $q\overline{q} \to e^-\overline{\nu}_e\gamma\gamma$ as a function of the minimum photon transverse momentum, $p_{T_\gamma}^{\min}$. The other cuts listed in section 6.3.2 of the text are imposed.

- Two photons, both with $p_{T_\gamma} > 15$ GeV and $|\eta_\gamma| < 2.4$.
- One electron with $p_{T_e} > 25$ GeV and $|\eta_e| < 2.4$.
- Missing energy satisfying $p_{T_{\rm miss}} > 20$ GeV
- Separation of photons, $\Delta R_{\gamma\gamma} > 0.4$, and each photon and electron, $\Delta R_{e\gamma} > 0.8$
- Transverse mass of $e^-\nu$ system: $M_T^{(e,\nu)} > 65$ GeV

Generator level cuts were chosen sufficiently far from these cuts on the reconstructed quantities to ensure that events absent at generator level could not be smeared by ATLFAST such that they would pass the selection.

6.3.3 Simulation Chain

The simulation of the signal process proceeded as follows. Weighted events were generated by W2GRAD, which was implemented as an external process to PYTHIA [99]

within the ATHENA-ATLFAST framework. PYTHIA was used to add extra QCD showers, beam remnants and underlying events and model the subsequent fragmentation and decay of the partons. Events were then selected from all those generated using an accept/reject algorithm. This accepts an event k with probability $w_k/w_{\max}$, where w_k is the weight of the event and $w_{\max}$ is some maximum weight. The events outputted from the algorithm were therefore all of unit weight, and these were passed to the ATLFAST simulation.

It should be noted that this is a leading order study in QCD only. The higher order quark-gluon initiated processes, such as $qg \to Wq'\gamma\gamma$, are not modelled in W2GRAD.

6.4 ATLFAST Jet-γ Mis-Identification Rate

The most important backgrounds to $W\gamma\gamma$ are anticipated to be $W\gamma$ + jet and W + 2jet events [95] in which one or both jets are mis-identified as photons. The probability for a jet to be mis-identified in this way is $1/R_{\text{rej}}$, where R_{rej} is referred to as the jet-γ rejection factor. Since the cross-sections for W plus one- or two-jet events are several orders of magnitude higher than the cross-section of the signal process, a high jet rejection factor is essential to control these background contributions.

A study of photon identification using the full ATLAS simulation software found the jet-γ rejection factor to be approximately 1 300 for a photon efficiency of 80%, for jets with $p_T \approx 20$ GeV at low luminosity [100]. That is, approximately 1 in 1 300 jets were falsely identified as photons. For the majority of these, the false identification occurred because the jet contained a "real" photon, for example from the decay of a pion. It has been suggested in [101] that this jet rejection can be improved by up to 70% by employing isolation as an additional criterion for photon identification, at the cost of a small loss of efficiency.

To evaluate the expected background contributions from mis-identified jets in $W\gamma$ + jet and W + 2jet events, 1 million of each type were generated using PYTHIA

and simulated in ATLFAST. The process $q\overline{q} \to W\gamma$ with additional jets from QCD ISR, but no FSR or QED ISR, was used to produce the $W\gamma$ + jet sample. For the W + 2jet sample, the $q\overline{q} \to W$ process, again with additional QCD ISR and no FSR was used. The $q\overline{q} \to gW$ and $qg \to qW$ processes were not employed since these are only accurate for events in the high p_T tail, $p_T > M_W$ [102]. For both samples the W was allowed to decay only to an electron and its neutrino. For every jet in a $W\gamma$ + jet event which, when re-labelled as a photon, allowed that event to pass the selection, the event was accepted with weight 1/1 300. The events of the W + 2jet sample were tested against the cuts taking each jet re-labelled as a photon together with every other jet similarly re-labelled. The events that passed were accepted with weight $(1/1\,300)^2$.

As ATLFAST makes no allowance for particle mis-identification, only photons that are present in the PYTHIA event record can be reconstructed. However, as stated above, the majority of the mis-identified jets arise by virtue of some part of the QCD shower fluctuating to a real photon, and ATLFAST can therefore also reconstruct such showers as photons. Since the rejection factor evaluated in [100] includes these contributions, taking with unit weight any $W\gamma$ + jet or W + 2jet events which are accepted without any jet re-labelling would double-count the background. It was found that the rate of such events was about three times the expectation, based on a rejection factor of 1 300, though this is thought to be a problem of the current ATLFAST definition of an isolated photon [103].

6.5 Summary and Results

$W\gamma\gamma$ production proceeding to the $l^{\pm}\nu_{l^{\pm}}\gamma\gamma$ final state could be the first tri-boson signal observed at the LHC. The process is sensitive to a possible AQGC coupling of the form $WW\gamma\gamma$. The Standard Model contribution to the exclusive $e^{-}\overline{\nu}_e\gamma\gamma$ final state has been evaluated and simulated at ATLAS. Background contributions from W + jet and W + 2jet events, in which one or both jets are mis-identified as photons, have also been evaluated assuming a jet-γ rejection factor of 1 300.

Applying the selection of section 6.3.2 and assuming an ATLAS efficiency of 80% for photons and electrons, the expected accepted cross-section for $q\overline{q} \to e^{-}\overline{\nu}_{e}\gamma\gamma$ is 0.48 fb. This corresponds to 14.4 events being expected in the 30 fb^{-1} of data that will be available in the first three (low luminosity) years of LHC operation. The rates for $q\overline{q} \to l^{-}\overline{\nu}_{l}\gamma\gamma$ will be about four times greater, depending on the ATLAS acceptance and efficiency for muons. Multiplying by four gives ~ 58 signal events, which is almost a factor of two higher than that reported in [33] and consistent with the lower value of the photon transverse momentum cut used here.

The background contributions in 30 fb^{-1} from W + jet and W + 2jet events are 9.2 and 5.3 events, respectively, assuming a low luminosity rejection factor of 1 300. This gives an overall signal to background ratio of approximately 1:1. It is likely that this could be improved by making additional requirements on the photon isolation, albeit at the cost of some photon efficiency.

The expected distributions of $p_{T_{\gamma 1}}$ and $M_{\gamma\gamma}$ in the first three years of ATLAS data are shown in figure 6.5. Both the Standard Model signal and background contributions are plotted. By cutting on the photon transverse momentum, the total Standard Model contribution can be largely removed. Above $p_{T_{\gamma 1}} = 200$ GeV, for example, both the Standard Model signal and background rates are negligible. Any AQGC contribution would then be signalled by an excess of events in this high p_T region, as shown in figure 6.2. Similarly, the total Standard Model contribution to the $M_{\gamma\gamma}$ distribution is very small above $M_{\gamma\gamma} = 500$ GeV, again allowing a clear signal for the possible anomalous $WW\gamma\gamma$ coupling to be seen here. The proposals reported in [33] for constraining the possible AQGC using its effects shown in figures 6.2 and 6.3 therefore remain valid after including the further Standard Model backgrounds considered here.

The expected limits on the anomalous coupling parameters a_0^{W} and $a_{\mathrm{c}}^{\mathrm{W}}$ at ATLAS could be found given a Monte Carlo program for $q\overline{q} \to l\overline{\nu}_{l}\gamma\gamma$ in which the $WW\gamma\gamma$ AQGC vertex is implemented.

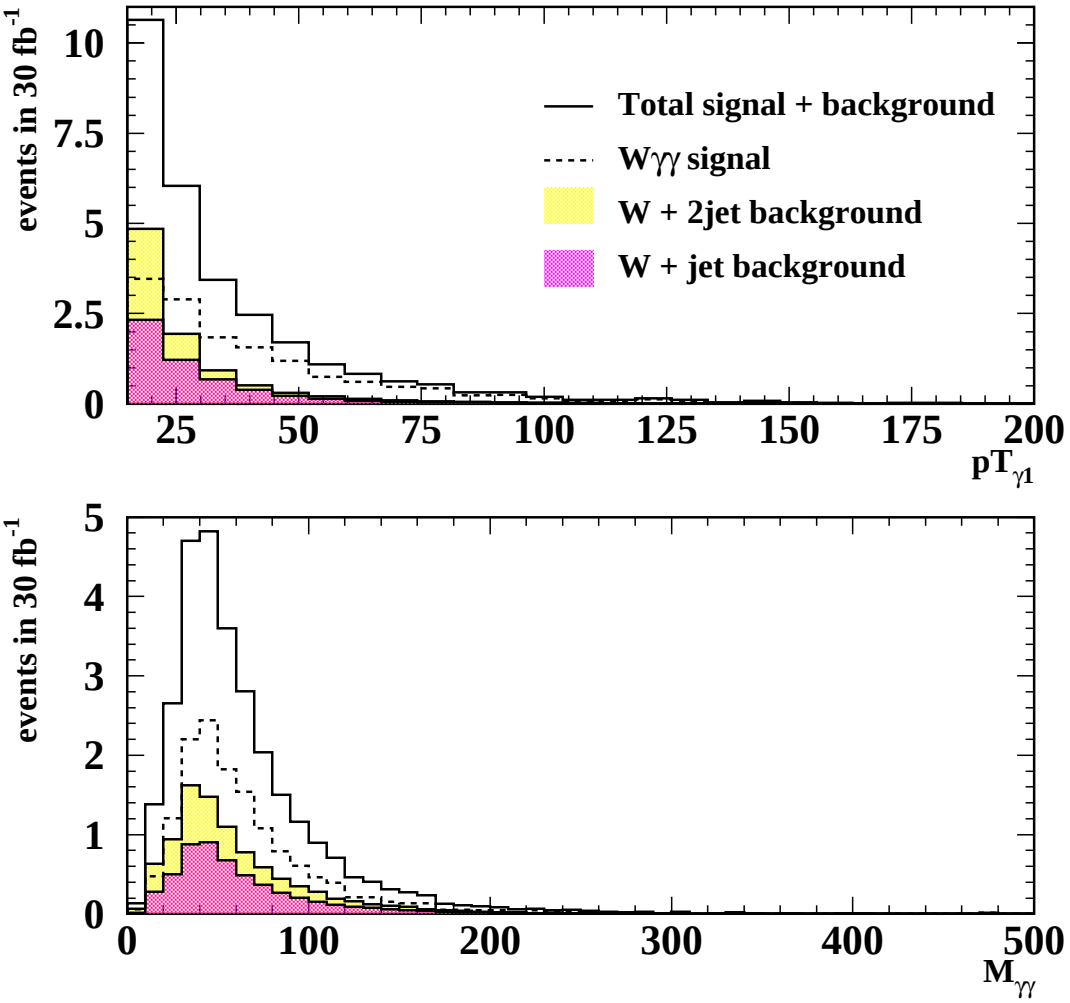

Figure 6.5: The expected distributions of $p_{T_{\gamma 1}}$ and $M_{\gamma\gamma}$ in signal and background, for the accepted $e^{-}\overline{\nu}_{e}\gamma\gamma$ events in 30 fb^{-1} of ATLAS data at low luminosity.

Bibliography

[1] G. Abbiendi *et al.* The OPAL Collaboration, OPAL Physics Note PN510, (July 2002).

[2] K. Hagiwara *et al.*, Review of Particle Physics, *Physical Review* **D66** (2002).

[3] The Super-Kamiokande Collaboration, *Phys. Rev. Lett.* **81**, 1562–1567 (1998).

[4] D. H. Perkins, *Introduction to High Energy Physics*, page 10, Addison-Wesley, 1987.

[5] H. F. Jones, *Groups, Representations and Physics*, IOP Publishing, 1990.

[6] F. Halzen and A. Martin, *Quarks and Leptons*, page 316, John Wiley and Sons, 1984.

[7] F. Halzen and A. Martin, *Quarks and Leptons*, page 149, John Wiley and Sons, 1984.

[8] G. t'Hooft, *Nucl. Phys.* **B33** (1971).

[9] E. Noether, *Nachr. Ges. Wiss. Gottingen* **171** (1918).

[10] F. Halzen and A. Martin, *Quarks and Leptons*, page 292, John Wiley and Sons, 1984.

[11] M. Kobayashi and K. Maskawa, *Prog. Ther. Phys* **49**, 652 (1973).

[12] F. Halzen and A. Martin, *Quarks and Leptons*, page 333, John Wiley and Sons, 1984.

[13] S. L. Glashow, *Nucl. Phys.* **22**, 579 (1961).

[14] P. W. Higgs, *Phys. Lett.* **12**, 132 (1964).

[15] G. Arnison *et al.*, *Phys. Lett.* **B118**, 167 (1982).

[16] M. Veltman, *Nucl. Phys.* **123**, 89 (1977).

[17] Giovanni Ridolfi, *An Introduction to the Standard Model of Electroweak Interactions*, CERN lectures.

[18] A. Salam and J. C. Ward, *Phys. Lett* **13**, 168 (1964).

[19] F. Halzen and A. Martin, *Quarks and Leptons*, page 334, John Wiley and Sons, 1984.

[20] O. Piguet, *Introduction to Supersymmetric Gauge Theories*, Lecture notes hep-th/9710095.

[21] G. Abbiendi *et al.* The OPAL Collaboration, *CERN-EP-2003-042, Submitted to Eur. Phys. J.* **C** (July 2003).

[22] G. Bélanger and F. Boudjema, *Phys. Lett* **B288**, 201 (1992).

[23] W. J. Stirling and A. Werthenbach, *Eur. Phys. J* **C14**, 103 (2000).

[24] G. Bélanger *et al.*, *Eur. Phys. J.* **C13**, 283 (2000).

[25] G. Abbiendi *et al.* The OPAL Collaboration, *Phys. Lett.* **B471**, 293 (1999).

[26] G. Abbiendi *et al.* The OPAL Collaboration, *CERN-EP-2003-043, Submitted to Phys. Lett. B.* (July 2003).

[27] G. Abbiendi *et al.* The OPAL Collaboration, OPAL Physics Note PN410, (July 1999).

[28] G. Abbiendi *et al.* The OPAL Collaboration, OPAL Physics Note PN452, (July 2000).

[29] The DELPHI Collaboration, *DELPHI 2003-059, contributed to EPS 03, Aachen* (2003), June.

[30] The L3 Collaboration, *CERN-EP/2001-080, contributed to EPS 03, Aachen* (2001), November.

[31] The L3 Collaboration, *CERN-EP/2002-034, contributed to EPS 03, Aachen* (2002), May.

[32] The ALEPH Collaboration, *ALEPH 2003-009, contributed to EPS 03, Aachen* (2003), June.

[33] O. J. P. Éboli, M. C. Gonzalez-García, and S. M. Lietti., Anomalous Quartic Gauge Boson Couplings at Hadron Colliders, *Phys. Lett.* **D63** (2001).

[34] W. J. Stirling and A. Werthenbach, *Phys. Lett.* **B466**, 369–374 (1999).

[35] S. Myers and E. Picasso, The Design, Construction and Commissioning of the CERN Large Electron Positron Collider, *Contemp. Phys.* **31**, 387 (1990).

[36] E. Picasso and G. Plass, The Machine Design, *Europhys. News* **20**, 80 (1989).

[37] K. Ahmet *et al.* The OPAL Collaboration, The OPAL Detector at LEP, *Nucl. Instrum. Meth.* **A305**, 275 (1991).

[38] D. Decamp *et al.* The ALEPH Collaboration, ALEPH: A Detector for Electron-Positron Annihilation at LEP, *Nucl. Instrum. Meth.* **A294**, 121 (1990).

[39] P. Aarnio *et al.* The DELPHI Collaboration, The DELPHI Detector at LEP, *Nucl. Instrum. Meth.* **A303**, 233 (1991).

[40] M. Acciarri *et al.* The L3 Collaboration, The Construction of the L3 Experiment, *Nucl. Instrum. Meth.* **A289**, 35 (1990).

[41] D. H. Perkins, *Introduction to High Energy Physics*, page 32, Addison-Wesley, 1987.

[42] R. J. Akers *et al.*, The OPAL Muon Barrel Detector, *Nucl. Instrum. Meth.* (1995).

[43] G. Artusi *et al.*, Limited Streamer Tubes for the OPAL Hadronic Calorimeter, *Nucl. Instrum. Meth.* (1989).

[44] S. Anderson *et al.*, The Extended OPAL Silicon Microvertex Detector, *Nucl. Instrum. Meth.* **A403**, 326 (1998).

[45] J. R. Carter *et al.*, The OPAL Vertex Drift Chamber, *Nucl. Instrum. Meth.* **A286**, 99 (1990).

[46] H. M. Fischer *et al.*, The OPAL Jet Chamber, *Nucl. Instrum. Meth.* (1989).

[47] H. Breuker *et al.*, *CERN-EP/1987-097* (1987).

[48] G. Aguillion *et al.*, Thin Scintillating Tiles with High Light Yield for the OPAL Endcaps, *Nucl. Instrum. Meth.* **A417**, 266 (1998).

[49] T. Kobayashi, Realisation of the OPAL Electromagnetic Barrel Calorimeter, in *2nd International Conference on Calorimetry in HEP*, Capri, Italy, 1991.

[50] D. H. Perkins, *Introduction to High Energy Physics*, page 57, Addison-Wesley, 1987.

[51] B. E. Anderson *et al.*, The OPAL Silicon-Tungsten Calorimeter Front End Electronics, *IEEE Trans. Nucl. Sci.* **41**, 845 (1994).

[52] M. Arignon *et al.*, The Trigger System of the OPAL Experiment at LEP, *Nucl. Instrum. Meth.* **A313**, 103 (1992).

[53] J. T. M. Baines *et al.*, The DAQ System of the OPAL Detector at LEP, *Nucl. Instrum. Meth.* **A325**, 271 (1993).

[54] D. G. Charlton, F. Meijers, T. J. Smith, and P. S. Wells, The Online Event Filter of the OPAL Experiment at LEP, *Nucl. Instrum. Meth.* **A325**, 129 (1993).

[55] C. Hawkes *et al.*, ROPE User Guide, (1996), OPAL offline note 16.

[56] CERN Application Software Group, Geant Detector Descrption and Simulation Tool, *Software Manual CERN Program Library Long Writeup W5013* (1993).

[57] J. Allison *et al.*, The Detector Simulation Program for the OPAL Experiment at LEP, *Nucl. Instrum. Meth.* **A317**, 47 (1992).

[58] G. Abbiendi *et al.* The OPAL Collaboration, *Eur. Phys. J* **C8**, 23 (1999).

[59] G. Abbiendi *et al.* The OPAL Collaboration, *Eur. Phys. J* **C18**, 253 (2000).

[60] R. Brun, O. Couet, C. Vandoni, and P. Zanarin, PAW users guide, *CERN Program Library Q121* (1991).

[61] G. Montagna, O. Nicrosini, and F. Piccinini, *Comput. Phys. Commun.* (1996).

[62] G. Montagna, M. Moretti, O. Nicrosini, M. Osmo, and F. Piccinini, *Phys. Lett.* **B515**, 197 (2001).

[63] Peter Krieger, Personal Commuication, June 2002.

[64] Peter Krieger, Personal Commuication, May 2002.

[65] S. Bain and R. Pain, Acoplanar Photons Background Generators, *DELPHI 97-89 CONF 75* (1997).

[66] P. Bevington and D. Robinson, *Data Reduction and Error Analysis for the Physical Science*, McGraw-Hill, 1992.

[67] G. Feldman and R. Cousins, Unified Approach to the Classical Statistical Analysis of Small Signals, *Phy. Rev.* **D57** (1998).

[68] F. James and M. Roos, MINUIT users guide, *CERN Program Library D506* (1981).

[69] G. Montagna, M. Moretti, O. Nicrosini, M. Osmo, and F. Piccinini, *NUCL. PHYS.* **B541**, 31 (1999).

[70] The DELPHI Collaboration, *DELPHI 98-39 PROG 231* (April 1998).

[71] F. A. Berends, P. H. Daverveldt, and R. Kleiss, *Comp. Phys. Commun.* **40**, 271 (1986).

[72] S. Jadach, B. F. L. Ward, and Z.Was, *Phys. Commun.* **130**, 260 (2000).

[73] Claudio Grandi, Luminosity Counting in ROPE with the Silicon-Tungsten Luminometer, *SW Note SW-48* (1994).

[74] M. Thomson, P. Bell, and D. Charlton, Constraints on Anomalous Quartic Gauge Boson Couplings from $\nu\overline{\nu}\gamma\gamma$ and $q\overline{q}\gamma\gamma$ Events at LEP-2, *OPAL Physics Report in editorial process* (September 2003).

[75] ATLAS Technical Proposal for a General Purpose pp Experiment at the LHC at CERN, *CERN/LHCC/94-43* (1994).

[76] The ATLAS First Level Trigger Technical Design Report, *CERN/LHCC/98-14* (1998).

[77] ATLAS Technical Design Report - Inner Detector, *CERN/LHCC/97-16, CERN/LHCC/97-17* (1997).

[78] M. Turala for the ATLAS SCT Collaboration, *Nuclear Instr. Meth.* **A466**, 243 (2001).

[79] Y. Unno for the ATLAS SCT Collaboration, *Nuclear Instr. Meth.* **A453**, 109 (2000).

[80] T. Kondo for the ATLAS SCT Collaboration, *Nuclear Instr. Meth.* **A485**, 27 (2002).

[81] Anna Peisert, Silicon Microstrip Detectors, Istituto Nazionale di Fisica Nucleare, Padova, January 1992.

[82] Review of Particle Physics, *Eur. Phys. J.* **C3**, 144 (1998).

[83] SCT Barrel Module Final Design Report - ASICs, *SCT-BM-FRD-5.4* (2001).

[84] P. Bell *et al.*, The ATLAS Semiconductor Barrel System Test, *ATLAS note in preparation* (2003).

[85] The SCT System Test web page:
http://home.cern.ch/asct186/systemtest.html.

[86] SCT barrel technical drawings:
http://dpnc.unige.ch/atlas/atlaspage/mecanact/webmec1.html.

[87] T. Weidberg, ATLAS-EDMS Technical Note, *ATL-IS-ES-0049* (2001).

[88] Documentation of the DAQ-system available at:
http://hepwww.rl.ac.uk/atlas-sct/mm/Slog/slog.pdf
http://hep.ucl.ac.uk/atlas/sct/cloac/Welcome.html
http://hepwww.rl.ac.uk/atlas sct/mm/Mustard/Mustard.ps.

[89] P. W. Phillips, Operation of Barrel Modules, *to be submitted as ATLAS-EDMS Technical Note* .

[90] System Test shielding options:
http://asct186.home.cern.ch/asct186/barrel_web/shield_options3.html.

[91] Noise occupancy studies:
http://asct186.home.cern.ch/asct186/barrel_web/es_investigation_2001−10.html.

[92] A. Chilingarov, Time Dependence of the Interstrip Capacitance, talk at the ATLAS SCT week, Valencia, June 2002.

[93] L. Feld *et al.*, *Nuclear Instr. Meth.* **A487**, 557 (2002).

[94] J. M. Butterworth, B. E. Cox, and J. R. Forshaw, WW scattering at the LHC, *Phys. Rev.* **D65** (2002).

[95] U. Baur, T. Han, N. Kauer, R. Sobey, and D. Zeppenfeld, W$\gamma\gamma$ Production at the Fermilab Tevatron Collider: Gauge Invariance and Radiation Amplitude Zero, *Phys. Rev.* **D56**, 140 (1997).

[96] E. Richter-Was, D. Froidevaux, and L. Poggioli, ATLFAST 2.0: A Fast Simulation Package for ATLAS, *ATL-PHYS-98-131* (1998).

[97] U. Baur and T. Stelzer, *Phys. Rev.* **D61** (2000).

[98] ATLAS Detector and Physics Technical Design Report, *CERN/LHCC/99-14* (1999).

[99] T. Sjöstrand, P. Edén, C. Friberg, L. Lönnblad, G. Miu, S. Mrenna, and E. Norrbin, *Computer Phys. Commun.* **135**, 238 (2001).

[100] M . Wielers, Photon Identification with the ATLAS Detector, *ATL-PHYS-99-016* (1999).

[101] M . Wielers, Isolation of Photons, *ATL-PHYS-02-004* (2002).

[102] T. Sjöstrand, L. Lönnblad, S. Mrenna, and P. Skands *Pythia 6.2: Physics and Manual*, page 178, hep-ph/0108264, 2002.

[103] Ian Hinchliffe, ATLAS Blind Tests, talk given at ATLAS overview week, Prague, September 2003.